On a Banks–Casher relation in MQCD

A. Gorsky
Institute of Theoretical and Experimental Physics, 117259 Moscow, Russia

(Submitted 16 November 1998)
Pis'ma Zh. Éksp. Teor. Fiz. **69**, No. 1, 3–7 (10 January 1999)

We discuss the meaning of a Banks–Casher relation for the Dirac operator eigenvalues in MQCD. It is argued that the eigenvalue can be identified with a coordinate involved in the string compactification manifold. © *1999 American Institute of Physics.* [S0021-3640(99)00101-2]

PACS numbers: 12.38.Lg, 11.30.Pb, 11.25.Sq

1. The brane approach to the SUSY gauge theories in different dimensions seems to be the most promising tool to capture their nonperturbative features. It is believed that all universal characteristics of the vacuum sector can be seen in terms of the brane picture. Recently a proper brane configuration was found in IIA[1] and *M* theory[2,3] for the theories with $N=1$ supersymmetry. The configuration for the pure gauge theory suggested in Ref. 1 involves NS5 and D4 branes which when lifted to *M* theory are identified with the single M5 brane wrapped around a Riemann surface embedded into the three-dimensional complex space.

It is known that a gluino condensate develops in $N=1$ SQCD, and the properties of the vacuum sector are governed by superpotentials generated in different ways depending on the relation between N_f and N_c. The gluino condensate is indicative of chiral symmetry breaking, so its derivation in the MQCD framework is very important. It was found that superpotentials can be calculated in *M* theory;[2,3,4] moreover, it turns out that the superpotential can be attributed to the 5-brane instantons.[5,6] General considerations of chirality in the brane approach indicate that at least in some situations it depends only on the local properties of the brane configuration.[7] It was also found[8] that the algebra of $N=1$ SUSY implies the existence of a domain wall between spatial regions with different phases of the gluino condensate.

In this note we consider the Banks–Casher relation[9] relating the properties of the Dirac operator eigenvalues in the instanton ensemble background with the value of the vacuum fermion condensate. This relation has been known for some time in QCD, where fermions in the fundamental representation condense in the vacuum. Generalization to the adjoint fermions relevant for the supersymmetric theory as well as additional sum rules for the spectral density of the Dirac operator have been discovered in Ref. 10. Spectral density is a universal characteristic of the low-energy sector of the theory, so one expects that it can also be treated in brane terms. Note that the universal behavior of the spectral density admits a matrix model approach for the investigation of its properties (see Ref. 11 for a review), which successfully describes key features of the spectrum. Below we

suggest an interpretation of a Banks–Casher relation in terms of M5 brane world volume and discuss the possible role of the Dirac operator eigenvalue as one of the dimensions involved in the brane picture.

2. Let us recall the main facts about the spectrum of the Dirac operator in QCD. One is concerned with eigenvalues of the operator $\hat{D}\Psi=\lambda\Psi$, and the density of the eigenvalues $\rho(\lambda)$ provides the order parameter in the low-energy sector. Namely, due to the Casher–Banks relation[9] for the fundamental fermions

$$\langle\bar{\Psi}\Psi\rangle=-\pi\rho(0)=-\int\frac{\rho(\lambda)d\lambda}{\lambda}, \tag{1}$$

the density at origin can be considered as the derivative of the partition function with respect to the mass $\pi\rho(0)=-d\ln Z/dm$ at $m=0$. More generally, there is an infinite tower of sum rules for the inverse powers of the eigenvalues,[10] for instance

$$\left\langle\sum\frac{1}{\lambda_i^2}\right\rangle_\nu=\frac{(\langle\bar{\Psi}\Psi\rangle V)^2}{4(|\nu|+N_f)}, \tag{2}$$

where the averaging with the spectral density is implied, V is the four-dimensional Euclidean volume, and ν is the topological charge of the gauge field configuration. The sum rules probe the structure of the small-λ region of the spectrum.

Another approach to the same object comes from the representation of the partition function as the path integral averaged fermion determinant

$$Z(m)=\langle\mathrm{Det}(iD-m)\rangle. \tag{3}$$

The averaging can be replaced by integration over the instanton moduli space, which due to the ADHM description, is modeled by the proper matrix model.[11] In this way of reasoning it is possible to derive the eigenvalue distribution itself. Actually the determinant can be considered as the observable in the theory dealing with the instanton moduli space. It is generally believed that the spectrum in the QCD instanton vacuum acquires a band structure due to delocalization of the zero mode on the single instanton in the instanton ensemble. It is assumed that zero eigenvalue lies in the allowed band, providing the chiral symmetry breaking.

A little bit different way to capture the fermion condensate is to consider the analytic properties of the resolvent of the Dirac operator considered on the complex mass plane

$$G(z)=\left\langle\mathrm{Tr}\frac{1}{iD-z}\right\rangle. \tag{4}$$

The Riemann surface of $G(z)$ has the cut along the imaginary axis, which is in one-to-one correspondence with the presence of the condensate.

3. Let us now proceed to the supersymmetric case. To start, note that we are now considering the condensate of gluinos–fermions in the adjoint representation. Banks–Casher relation for the adjoint fermions holds true,[10] so the issue of the derivation of the gluino condensate via the spectral density is well defined.

We would like to obtain the brane interpretation of the Banks–Casher relation as well as some features of the spectral density. The *M*-theory picture amounts to the $N=2$ SUSY gauge theory on the world volume of the *M*-theory fivebrane wrapped around the surface Σ^{12} (see also Ref. 13):

$$t^2-P_n(v)t+1=0. \tag{5}$$

In what follows we would like to present arguments that v can be identified with the eigenvalue of the four-dimensional Dirac operator. To treat the $N=1$ theory we should proceed in two steps. First, we have to shrink all monopole cycles on the surface Σ, reducing the curve to

$$y^2=\left(\frac{v^2}{4}-1\right)Q_{n-1}^2(v), \quad y=t-t^{-1}, \tag{6}$$

where Q_n are the Chebyshev polynomials. Then one performs a ''rotation'' which embeds the new curve into three-dimensional complex space. The resulting rational curve has the form

$$v=t^n, \qquad vw=\theta, \tag{7}$$

where θ can be identified with the gluino condensate in Refs. 2 and 3. We would like to consider the equation

$$\langle\xi\xi\rangle=\int w\,dv, \tag{8}$$

where ξ is the gluino field, as a Banks–Casher relation. Since in the IIA language D4 branes are located between two NS5 branes, this identification implies that the condensate develops purely due to the presence of one NS5 brane at $v=0$.

Let us comment on the interpretation of the v, w, and t variables in the field theory framework. In the theory with $N=4$ supersymmetry it is straightforward to identify six dimensions with the zero modes of three complex scalar fields. If one treats $N=2$ theories starting from softly broken $N=4$ theories, then the trace from two complex dimensions corresponding to the massive scalar fields survives due to the dimensional transmutation. We conjectured a quite different interpretation in $N=1$ theory, assuming that v is the eigenvalue of the Dirac operator. Therefore the coordinates w and t have to be considered as the eigenvalues of operators commuting with the Dirac operator and can therefore be associated with the global symmetries.

Let us compare our interpretation of $N=1$ theory with $N=2$ theory and show that there is qualitative agreement with the standard treatment of these theories. We will use arguments coming from an approach based on the relation of $N=2$ theories to the integrable systems.[14]

In the IIA picture the $N=2$ theory lives on the world volume of N_c D4 branes with finite extent in the x_6 dimension.[12] Parallel NS5 branes are located at $x_6=0$ and $x_6=l_s/g^2g_s$ where g_s and l_s are the IIA string coupling and length respectively. It was argued in Refs. 15 and 16 that integrable structure behind the solution of the theory implies that there are N_c D0 branes living on D4, one per each, whose equilibrium positions are

$$x_{6,k}=kl_s/N_cg^2. \tag{9}$$

When lifted to the M theory, the D0 branes represent the linear bundle on the spectral curve of the integrable system, which has been identified with the Riemann surface Σ which the M5 brane is wrapped around. The linear bundle yields half of the phase space of the integrable system, and the fluctuations of interacting D0 branes around these points define a Toda dynamics which linearizes on the Jacobian of the spectral curve. These branes can be treated as the point-like Abelian instantons in the four-dimensional theory, and their possible role was discussed in Refs. 16–18.

Let us now discuss fermions on the M5 world volume. Consider the zero mode of the six-dimensional Dirac operator D, which we decompose as

$$D=D^4+d^{\Sigma}, \tag{10}$$

where d^{Σ} denotes the Dirac operator on the spectral curve. We decompose the fermion wave function after IIA projection as

$$\Psi(x,x_6)=\sum_{\lambda}\ \Psi_{\lambda}(x)\Phi(n,\lambda), \tag{11}$$

where $x=(x_0,x_1,x_2,x_3)$, and n denotes the sites where the $D0$'s are localized. We conjecture that $\Phi(n,\lambda)$ is just the Baker function for the Lax equation in the Toda system if the eigenvalue of the four-dimensional Dirac operator D^4 is equal to λ. Baker fermions in the Toda system have Σ as the Fermi surface.

In IIA projection one has the fermion zero modes localized on $D0$'s so it is natural to consider the fermion wave function $\Phi(n,\lambda)$ with discrete n. Fermion zero modes on the nearest $D4$'s overlap, and the Dirac operator along x_6 acquires the discrete form

$$c_n\Phi_{n-1}+p_n\Phi_n+c_{n+1}\Phi_{n+1}=\lambda\Phi_n, \qquad c_n=\exp(x_{n+1}-x_n), \tag{12}$$

where x_i is the position of the ith $D0$ brane along the x_6 direction and coincides with the familiar expression for the Lax equation in the Toda system in the 2×2 representation.

Let us emphasize that the Hitchin-like dynamical system involving $D0$ branes cannot be seen at the classical level and has to be regarded as a quantum or quasiclassical effect. The phase space of the relevant Hitchin system is the hyper-Kähler manifold and can be interpreted as a hidden Higgs branch of the moduli space in $N=2$ theories. The very role of the integrability is to restrict N_c KK modes in the M-theory picture to the $M5$ brane world volume. Comparing expressions for the condensate in $N=1$ theory, we expect the identification

$$w(v)dv\propto\frac{\rho(\lambda)}{\lambda}d\lambda. \tag{13}$$

It is worth remarking on the corresponding deformation of the integrable system. At the first step we should fix all integrals of motion in the Toda system and then perturb it by the mass term. It is not clear at the moment if some integrable dynamics survives, but the potential degrees of freedom, namely the $D0$'s, still play an important role in the generation of the superpotential.[19] Therefore one has the proper candidates for the phase space-rational spectral curve which the $M5$ brane is wrapped around, and the linear bundle on it.

4. Some insights come from the analogy with the discrete Peierls model,[20] which is relevant for the description of one-dimensional superconductivity. The model is defined as follows: There is a periodic one-dimensional crystal with N_c sites and fermions interacting with phonon degrees of freedom. It is assumed that fermions are strongly coupled to the lattice and can jump only between nearest sites. This system is described by the periodic Toda lattice,[21] where the Toda Lax operator serves as the Hamiltonian for the fermions and the Toda degrees of freedom derive from the phonons.

The spectral curve for the Toda system coincides with the dispersion relation of the fermions, and the Lax equation coincides with the Schrödinger equation. The initial condition for the Toda evolution is chosen dynamically to minimize the total energy of fermions and phonons, and it appears that the generic curve degenerates to the ''$N=2$ curve'' with all monopole cycles vanishing. This resembles the first step towards the $N=1$ theory. Fermions develop a mass gap, and the analog of the chiral invariance known in the model is broken dynamically due to the nontrivial band around zero energy. This yields a dynamical scenario which resembles the one in the $N=1$ theory.

To conclude, we have considered the possible meaning of the Banks–Casher relation in the MQCD framework. We have obtained a qualitative picture explaining the nonvanishing spectral density of the Dirac operator at the origin and have discussed the geometrical meaning of the eigenvalues themselves. We have conjectured that six dimensions involved in the brane configuration for $N=1$ theory admit interpretation as the Dirac operator eigenvalue and eigenvalues of the two global symmetry generators. Certainly more quantitative analysis is required to confirm the picture suggested.

We would like to thank H. Leutwyler, A. Mironov, A. Morozov and A. Smilga for helpful discussions. This work was supported in part by grants CRDF-RP2-132, INTAS 96-482, and RFFR-97-02-16131.

[1] S. Elitzur, A. Giveon, D. Kutasov, and E. Rabinovichi, Nucl. Phys. B **505**, 202 (1997); http://xxx.lanl.gov/abs/hep-th/9704104.
[2] K. Hori, H. Ooguri, and Y. Oz, Adv. Theor. Math. Phys. **1**, 1 (1998); http://xxx.lanl.gov/abs/hep-th/9706082.
[3] E. Witten, Nucl. Phys. B **507**, 658 (1997); http://xxx.lanl.gov/abs/hep-th/9706109.
[4] S. Nam, K. Oh, and S. Sin, http://xxx.lanl.gov/abs/hep-th/9707247.
[5] E. Witten, Nucl. Phys. B **474**, 343 (1996); http://xxx.lanl.gov/abs/hep-th/9604030.
[6] C. Gomez, http://xxx.lanl.gov/abs/hep-th/9711074.
[7] J. Brodie and A. Hanany, Nucl. Phys. B **506**, 157 (1997); http://xxx.lanl.gov/abs/hep-th/9704043.
[8] M. Shifman and G. Dvali, Phys. Lett. B **396**, 64 (1997); http://xxx.lanl.gov/abs/hep-th/9612128; A. Kovner, M. Shifman, and A. Smilga, http://xxx.lanl.gov/abs/hep-th/9706089.
[9] T. Banks and A. Casher, Nucl. Phys. B **169**, 103 (1980).
[10] H. Leutwyler and A. Smilga, Phys. Rev. D **46**, 5607 (1992).
[11] J. Verbarschoot, http://xxx.lanl.gov/abs/hep-th/9710114.
[12] E. Witten, http://xxx.lanl.gov/abs/hep-th/9703166.
[13] A. Klemm, W. Lerche, P. Mair *et al.*, Nucl. Phys. B **477**, 746 (1996); http://xxx.lanl.gov/abs/hep-th/9604034.
[14] A. Gorsky, I. Krichever, A. Marshakov *et al.*, Phys. Lett. B **355**, 466 (1995); http://xxx.lanl.gov/abs/hep-th/9505135.
[15] A. Gorsky, Phys. Lett. B **410**, 22 (1997); http://xxx.lanl.gov/abs/hep-th/9612238.
[16] A. Gorsky, S. Gukov, and A. Mironov, Nucl. Phys. B **517**, 409 (1998); http://xxx.lanl.gov/abs/hep-th/9707120.
[17] J. Barbon and A. Pasquinucci, http://xxx.lanl.gov/abs/hep-th/9712135; hep-th/9708041.
[18] J. Brodie, http://xxx.lanl.gov/abs/hep-th/9803140.
[19] A. Karch, D. Lust, and D. Smith, http://xxx.lanl.gov/abs/hep-th/9803232.
[20] A. Gorsky, Mod. Phys. Lett. A **12**, 719 (1997).

[21] S. A. Brazovskiĭ, N. E. Dzyaloshinskiĭ, and I. M. Krichever, Zh. Éksp. Teor. Fiz. **83**, 389 (1982) [Sov. Phys. JETP **56**, 212 (1982)].

Published in English in the original Russian journal. Edited by Steve Torstveit.

Detection of the structure of the wing of the Rayleigh line in ice, water, and heavy water using four-photon polarization spectroscopy

N. P. Andreeva, A. F. Bunkin,* and A. A. Nurmatov
Institute of General Physics, Russian Academy of Sciences, 117942 Moscow, Russia

(Submitted 20 November 1998)
Pis'ma Zh. Éksp. Teor. Fiz. **69**, No. 1, 12–14 (10 January 1999)

The spectral structure of the wing of the Rayleigh line in ice, ordinary water (H_2O), and heavy water (D_2O) is recorded in the frequency range $0-50\ \mathrm{cm}^{-1}$ by means of four-photon polarization spectroscopy. It is shown that this structure can be explained by the collective rotational motion of molecules in cells determined by the structure of hexagonal ice. © *1999 American Institute of Physics.* [S0021-3640(99)00301-1]

PACS numbers: 61.25.Em, 33.20.Sn

The investigation of the spectra of low-frequency rotational motions in associated liquids, specifically, water and aqueous solutions, yields information about the structure, degree of orientational order, and lifetimes of clusters. However, in spontaneous light scattering spectroscopy one cannot observe any structure in the wing of the Rayleigh line at frequency detunings greater than $0.5\ \mathrm{cm}^{-1}$ because of the low signal/noise ratio. For this reason, we took on the task of investigating experimentally the structure of the wing of the Rayleigh line in ice, water, and heavy water over a wide spectral range by means of four-photon polarization spectroscopy.[1]

The experimental arrangement is presented in Ref. 1. The four-photon spectrum of ice in the frequency range $-20\ \mathrm{cm}^{-1}$ to $+7\ \mathrm{cm}^{-1}$ is displayed in Fig. 1. The spectrum is seen to have a complicated structure, which can be explained using a model of the formation and migration of orientational defects in ice.[2] The model is based on the assumption that the reorientation of O–H dipoles occurs as a result of proton migration along a chain of hydrogen bonds. The orientational defect is defined as a collection of O–H bonds that consists of a collective associate in which the reorientation of O–H dipoles occurs coherently.[3–6] Given the maximum moment of inertia of a water molecule ($2.94\times10^{-40}\ \mathrm{g\cdot cm}^2$) and the fact that the frequency of the rotational mode of a water molecule can be expressed as (see Refs. 7 and 8)

$$\nu_i=\frac{\hbar}{4\pi c I_i}$$

(where c is the speed of light and I_i are the principal moments of inertia of the molecule), one can calculate the minimum frequency of the rotational mode of a water molecule as $9.52\ \mathrm{cm}^{-1}$. Taking into account that a cell in hexagonal ice consists of eight molecules

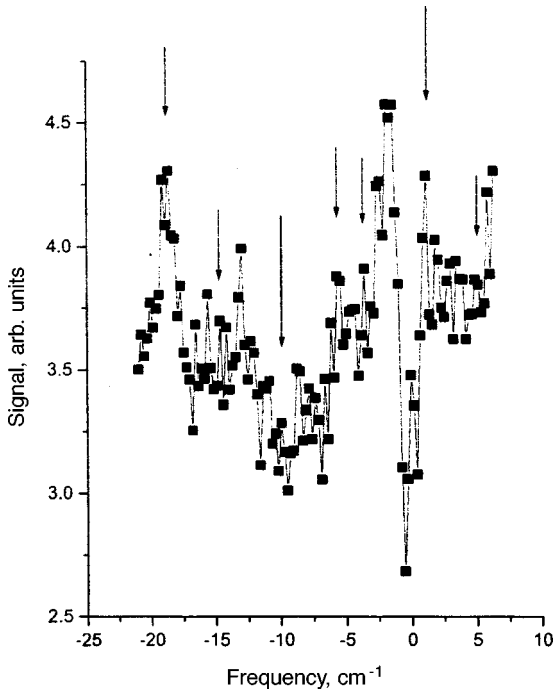

FIG. 1. Low-frequency four-photon spectrum of ice Ih. The arrows mark the principal resonance frequencies.

and using the results of Ref. 2, one can show that the minimum libration frequency in such a cell should be $\sim 1.2\ \mathrm{cm}^{-1}$ (Ref. 2). As one can see from Figs. 1 and 2, these resonances both appear in the spectra of ice and water (Fig. 2). The calculations performed using the two other principal moments of inertia ($1.92\times 10^{-40}\ \mathrm{g\cdot cm}^2$, $1.02\times 10^{-40}\ \mathrm{g\cdot cm}^2$) showed that the corresponding orientational resonances (with frequencies $14.52\ \mathrm{cm}^{-1}$ and $27.5\ \mathrm{cm}^{-1}$) are also present in the spectra of ice and water. To calculate the frequencies of other rotational modes of a free water molecule, various combinations of the three principal moments of inertia, $1/I_1+1/I_2$, $1/I_1+1/I_3$, $1/I_2+1/I_3$, and $1/I_1+1/I_2+1/I_3$, must be substituted into Eq. (1).[8] A calculation showed that the spectra of ice and ordinary water (Figs. 1 and 2) possess peaks that correspond to the librations of free molecules (9.5, 14.6, 27.4, 24.1, 37, 42.3, $51.6\ \mathrm{cm}^{-1}$) and complexes consisting of two (7.3, $8.12\ \mathrm{cm}^{-1}$), three (12.3, 14.1, $17.2\ \mathrm{cm}^{-1}$), four (6, 9.25, 10.6, $12.9\ \mathrm{cm}^{-1}$), six (1.6, 4.6, and $8.6\ \mathrm{cm}^{-1}$), and eight (1.2, 1.8, 3, $3.6\ \mathrm{cm}^{-1}$) molecules.

Using the computed frequencies we performed a model calculation of the four-photon spectrum of water. The results, together with the experimental spectrum, are displayed in the inset in Fig. 2. It is evident from Fig. 2 that the experimental and computed spectra agree quite well with one another. Therefore it can be inferred that the structure of the wing of the Rayleigh line in the experimental range of frequency detunings is due to the coherent reorientations of molecules in the cells determined by the structure of hexagonal ice.

To check these assumptions, similar experiments were performed with heavy water, whose principal molecular moments of inertia are $5.67\times 10^{-40}\ \mathrm{g\cdot cm}^2$,

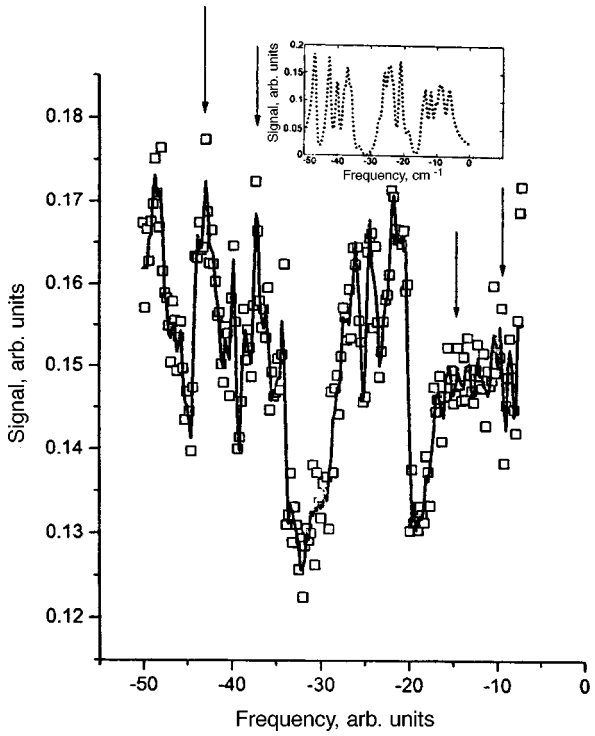

FIG. 2. Four-photon spectrum of water (H_2O). Inset: Computed spectrum.

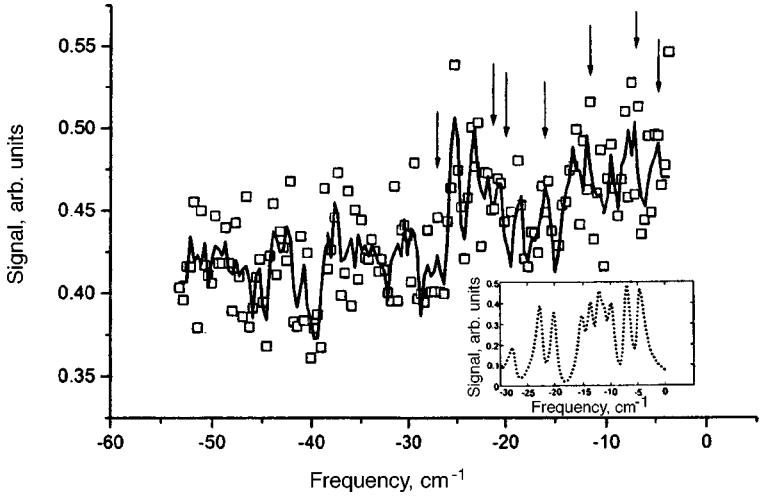

FIG. 3. Four-photon spectrum of heavy water (D_2O). Inset: Computed spectrum.

3.83×10^{-40} g·cm^2, and 1.84×10^{-40} g·cm^2 (Ref. 9). The corresponding values of the rotational frequencies of D_2O molecules (4.94, 7.3, 15.2, 12.23, 22.58, 20.14, and 27.45 cm^{-1}) can be calculated as was done for the H_2O molecule. The experimental and computed four-photon spectra of heavy water are displayed in Fig. 3. It is evident from this figure that the computed and experimental values of the resonance frequencies also agree well with one another.

In summary, we were able to observe the structure of the wing of the Rayleigh line in ice, ordinary water, and heavy water in the frequency range $0-50$ cm^{-1} by means of four-photon polarization spectroscopy. Such a structure has not been previously detected by other methods. The observed structure in the spectra of ice, H_2O, and D_2O can be explained by the collective rotational motion of water molecules in cells determined by the structure of hexagonal ice.

This work was supported by the Russian Fund for Fundamental Research (Grants Nos. 96-02-16533 and 98-02-16074) and the Russian Federal Programs ''Fundamental Spectroscopy'' and ''Fundamental Metrology.''

*e-mail: abunkin@orc.ru

[1] A. F. Bunkin, G. A. Lyakhov, A. A. Nurmatov, and N. V. Suyasov, Appl. Phys. B: Lasers Opt. **66**, 91 (1998).
[2] E. S. Kryachko, Preprint No. ITF-86-15 [in Russian], Kiev, 1986.
[3] D. Eisenberg and W. Kauzmann, *The Structure and Properties of Water*, Oxford University Press, Oxford, 1969.
[4] H. Granicher, Proc. R. Soc. London, Ser. A **247**, 453 (1958).
[5] N. D. Sokolov, Usp. Fiz. Nauk **57**, 205 (1955).
[6] A. Kahane, in *Physics of Ice*, Plenum Press, New York, 1969, p. 443.
[7] T. Del Guidice, G. Preparata, and G. Vitello, Phys. Rev. Lett. **61**, 1085 (1988).
[8] M. V. Vol'kenshteĭn, L. A. Gribov, M. A. El'yashevich, and B. I. Stepanov, *Vibrations of Molecules*, Nauka, Moscow, 1972.
[9] W. S. Benedict, E. K. Plyler, J. Res. Natl. Bur. Stand. **46**, 246 (1951).

Translated by M. E. Alferieff

High-pressure microwave discharge in an above-breakdown field. Streamer branching

P. V. Vedenin and N. E. Rozanov
Moscow Radio Engineering Institute, Russian Academy of Sciences, 113519 Moscow, Russia

(Submitted 16 November 1998)
Pis'ma Zh. Éksp. Teor. Fiz. **69**, No. 1, 15–19 (10 January 1999)

A new effect — the splitting of the tips (branching) of a microwave streamer arising from a pre-existing dense plasma cloud in an above-threshold electric field — is obtained numerically on the basis of a planar two-dimensional model. The causes of this phenomenon and the factors suppressing it are found. An expression is obtained for the value of the cloud radius above which branching occurs. © *1999 American Institute of Physics.* [S0021-3640(99)00401-6]

PACS numbers: 52.80.Tn, 51.50.+v

Theoretical investigations of microwave streamers arising near a discrete, extremely small center of ionization, for example, a single electron, in an above-breakdown field have thus far focused only on the main characteristics — the plasma density in the channel, the amplitude of the field in the channel and at the tips, the elongation and expansion rates, and the width of the ionization wave front propagating along the electric field.[1–3] As a result, a definite picture has been constructed of the streamer shape and the dynamics of these characteristics both in the presence[3] and absence[1,2] of the photoplasma produced in front of the tips; an investigation of the electrodynamic stage of the process has been initiated;[2] and, a semianalytical model describing the electrostatic stage of the evolution of a streamer has been constructed using a system of plasma chemical reactions.[4] How will this picture change if the ''seed'' employed is a dense plasma cloud produced by an external source, with a density profile differing strongly from the density profile that is formed by the time that the avalanche–streamer transition commences in the case with a discrete ionization center? In this letter we attempt to answer this question.

Formulation of the problem

Let a plasma cloud (plasmoid) be located at an antinode of a standing electromagnetic plane wave with components B_z and E_y. Let the radius of the cloud be r_0 and let the cloud be infinitely long and uniform along the z axis. The initial dimensions of the plasmoid satisfy the condition $kr_0 \ll 1$, where $k=\omega/c$ and ω is the microwave frequency. The amplitude E_V of the electric field at the antinode is greater than the breakdown value.

The numerical calculations were performed on the basis of a system of equations for the slowly time-varying ($\partial_t \ll \omega$) complex amplitudes and a model electron-balance equation:

$$\left(\partial_x \frac{1}{\epsilon}\partial_x + \partial_y \frac{1}{\epsilon}\partial_y + 1\right) B_z = 0, \quad E_x = \frac{i}{\epsilon}\partial_y B_z, \quad E_y = -\frac{i}{\epsilon}\partial_x B_z, \tag{1}$$

$$[\partial_t - |E|^\beta - D(\partial_{xx}^2 + \partial_{yy}^2)]n = 0,$$

where

$$\partial_\xi = \partial/\partial\xi;$$

$$\nu_{iV}t,\ kx,\ ky,\ B_z/E_V,\ E_{x,y}/E_V,\ n/n_{cr} \to t,\ x,\ y,\ B_z,\ E_{x,y},\ n;$$

$$\epsilon = 1 - n(1 - i\nu); \quad \nu = \nu_e/\omega \gg 1; \quad n_{cr} = m(\omega^2 + \nu_e^2)/4\pi e^2; \quad D = D_a k^2/\nu_{iV};$$

$\nu_{iV}(\propto E_V^\beta)$ is the ionization frequency in the field E_V, ν_e is the transport collision frequency of the electrons, and D_a is the ambipolar diffusion coefficient. The boundary conditions are the Sommerfeld radiation conditions. We underscore that only the terms that are primarily responsible for the branching effect are retained in the electron balance equation. The numerical algorithm used to solve Eq. (1) is described in detail in Ref. 2.

Anticipating the results, we shall say that streamer branching depends strongly on the plasma density distribution in the initial plasma cloud. For this reason, to avoid overburdening this letter, we shall present only the results obtained for the simplest case, taking as the initial profile

$$n_0(x,y) = n_{c0}\begin{cases} 1 - \left(\dfrac{r}{r_0}\right)^{2q}, & r \leqslant r_0 \\ 0, & r \geqslant r_0, \end{cases} \tag{2}$$

where $r^2 = x^2 + y^2$, $q \geqslant 1$. The index c indicates everywhere in this letter that the parameter so labeled refers to the point (0, 0). One can switch from a gently sloping density profile to the almost uniform density by increasing the parameter q.

Results of numerical simulation

For fixed values of the parameters D, n_{c0}, q, and β, the streamer can assume different forms in the course of its evolution, depending on the initial radius r_0. If $r_0 < R_{\text{tr}}(1 - \delta_-)$ ($\delta_- \ll 1$; the radius R_{tr} is discussed below), the streamer propagates along the y axis as a unit which looks like an ellipse in the xy cross section. If $r_0 > R_{\text{tr}}(1 + \delta_+)$ ($\delta_+ \ll 1$), each streamer tip (in what follows, we shall talk only about one of two tips arranged symmetrically relative to the x axis) splits into two (or more) parts arranged symmetrically relative to the y axis. This result is demonstrated in Fig. 1 (where on account of the symmetry of the problem, only half of a streamer is shown), which shows isolines of the electron density $n(x,y,t_1)/n_m =$ const ($n_m = \max n(x,y,t_1)$) at the time $t_1 = 4.9$ in the case $r_0 = 1.5 \times 10^{-2}$, $n_{c0} = 2 \times 10^{-2}$, $q = 4$, $D \cdot E_V^\beta = 2 \times 10^{-6}$, and $\beta = 5$. In the narrow transition region $\delta_- + \delta_+$, as r_0 decreases, the branches approach one another and merge at $r_0 = R_{\text{tr}}$ into a single, onion-shaped tip.

The general (for any r_0) characteristic features of the initial stage of the evolution of a streamer, during which $L = l_y/l_x \leqslant 1.5$ (l_x and l_y are the length and width, measured at the $0.1n_m$ level), are as follows. In a time t_r the electric field at the center,

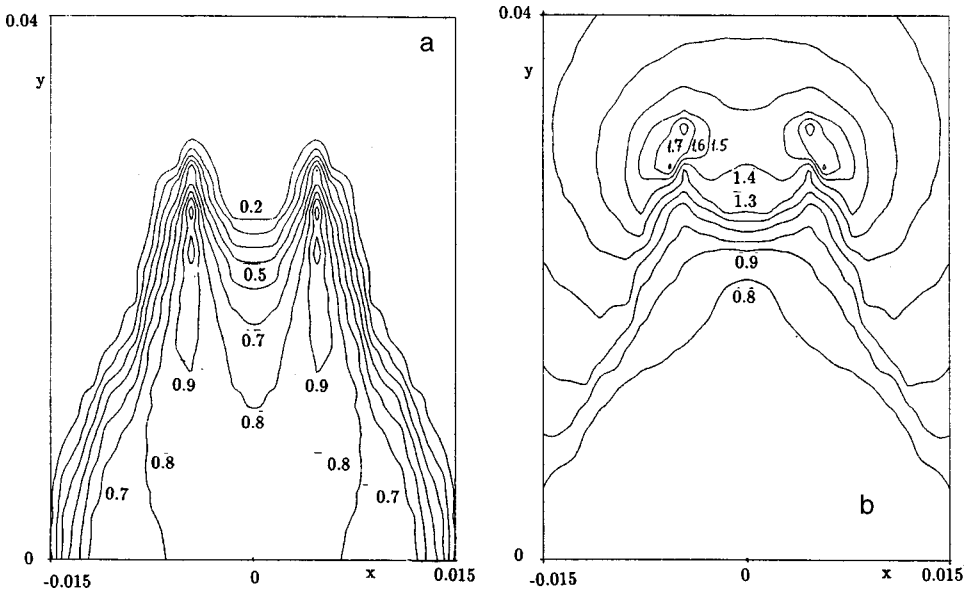

FIG. 1. Isolines of the plasma electron density normalized to the maximum value (a) and isoline of the modulus of the normalized electric field (b) for $r_0=1.5\times10^{-2}$, $n_{c0}=2\times10^{-2}$, $q=4$, $D\cdot E_V^{\beta}=2\times10^{-6}$, $\beta=5$ at time $t=4.9$.

$E_c=(1+ih)^{-1}(h=\sigma_c/(L+1), L=l_y/l_x, \sigma_c\simeq\nu n_c)$, reaches a quasistationary value, and the initial plasma density profile changes appreciably, becoming flatter or steeper depending on the value of the parameter q. This results in the formation of longitudinal and transverse fronts, whose velocities can be described by the expressions

$$u_y=2s_y\sqrt{D|E_m|^{\beta}} \quad \text{and} \quad u_x=2s_x\sqrt{D|E_c|^{\beta}}, \tag{3}$$

where $s_y=1.5$, $s_x\cong1$, and $|E_m|$ is the maximum amplitude of the field at a tip. At this stage the dynamics of the main characteristics σ_c, $|E_c|$, and $|E_m|$ and, together with them, the velocities u_y and u_x are determined mainly by the parameter h and depend only weakly on r_0.

The differences in the shapes of streamers with large and small initial radii become clear by the end of the initial stage. The density maxima move away from the point (0, 0) into the region near the tips, settling either on the y axis (in this case, the density profile $n(0,y,t)$ is dumbbell-shaped) or somewhere near the y axis ($n_m(-x,y)=n_m(x,y)$). We note that the longitudinal effect (displacement of the density maxima along the y axis) has been observed (see Refs. 1 and 2) in a numerical simulation of a microwave streamer developing from a discrete ionization center. As far as we know, the transverse splitting of a streamer tip has not been previously reported.

When transverse zones where the density is high appear, the maxima of the field amplitude move into them. This is demonstrated in Fig. 1b, where the isolines $|E(x,y)|=\text{const}$ are displayed.

Thus side branches, which overtake the central part, form at the tip of a streamer, if the front is sufficiently steep. These branch streamers propagate parallel to the external

electric field, and their length and the field amplitude at their tips gradually increase. In the present work we confined our attention only to a quite short stage in the development of the type of microwave discharge described ($l_y < 3r_0$), but this scenario apparently can also take place at later times.

Branching mechanism. Estimate of the transition radius R_{tr}.

Since the amplitude of the field inside a plasmoid with diffuse boundaries increases from the center toward the periphery and, conversely, the electron density decreases, zones of accelerated ionization of the gas will arise in an above-breakdown field right from the very beginning of the evolution of an initiated discharge. Conditions for the nucleation of local regions with elevated plasma density are produced precisely at these locations. Since these loacl regions comprise a small fraction of the total volume of the plasmoid, the amplitude of the field in them, being an integral characteristic of the charge density, is insensitive to local density variations. Therefore plasma production continues until the streamer has grown appreciably in size, $l_y(t) \cong r_0 + u_y t$, $l_x(t) \cong r_0 + u_x t$, i.e., as long as

$$r_0 \gg u_y t_{br} \quad (u_y t_{br} \cong 2 s_y t_{br} \sqrt{D|E_m|^{\beta}} \gg \sqrt{D}), \tag{4}$$

where $u_y > u_x$, $t_{br} \gg 1$ is the time of the onset of branching, plasma production continues.

A number of factors impede the formation of zones of elevated plasma density. The main ones are diffusion, which smooths density perturbations, and an increase in the velocities u_y and u_x (mainly, of course, u_y). To determine the role of diffusion in the branching mechanism, the results of calculations with and without diffusion were compared at the same small value $r_0 \ll R_{tr}$. It turned out that for $D = 0$ (in contrast to $D \neq 0$), the side density maxima arise after a short period of time.

When a local density hump $\delta n > 0$ arises on the profile $n(x,y)$ near some point, the plasma production rate at this point will change by an amount of the order of $\delta n(\psi - D/\Delta^2)$, where ψ is the response of this rate to the disturbance δn, which depends strongly on the field amplitude, and Δ is the characteristic size of the perturbation, $\Delta \ll r_0$. To obtain a rough estimate of R_{tr}, for us it is not the value of the response function that is important but rather the fact that this function, together with the field amplitude, depends mainly on the ratio of the streamer length to the streamer width and is insensitive to the variation in r_0. For this reason, the sign of the expression in parentheses is determined by the diffusion length, i.e., ultimately by the initial radius r_0. For $\psi > 0$ and $r_0 \gg \sqrt{D}$, this sign is positive, and the perturbation grows.

The final result is the following expression for the radius R_{tr} at which a transition occurs from one streamer shape to another:

$$R_{tr} = f(n_{c0}, q, \beta)\sqrt{D}, \tag{5}$$

where $f \gg 1$ is a form factor, which is established on the basis of numerical calculations.

It follows from Eq. (5) that the transition radius depends strongly on the amplitude of the external field (it is inversely proportional to $E_V^{\beta/2}$) and that it increases with the ambipolar diffusion coefficient (as $\sqrt{D_a}$). The simulation gave the following results.

1. The values $q=10$, 5, 2.5, and 1 correspond to $f(\beta=5, n_{c0}=2\times10^{-2})\cong22$, 24, 28, and 40. We underscore that the relation (5) refers only to a profile of the form (2), but even in this very simple case the dependence $f(q)$ is quite strong for $q\leqslant5$.

2. As the parameter β varies from 2 to 6, the form factor varies in the range $f(q=10,\ n_{c0}=2\times10^{-2})\cong18$–26.

3. The form factor is virtually independent of the initial density for $1<\sigma_{c0}<4(\sigma_c\cong\nu n_c)$. Outside this range the question of the relation between the transition radius and n_0 merges with the question of the influence of the shape of the initial plasma cloud on the branching.

The present work is the first attempt to understand what causes the branching of an rf streamer, and we are not yet ready to compare the results with the experimental data.[5–8] Such a comparison can probably be made in subsequent works, where we intend to: a) clarify the influence of the shape of the initial plasma cloud and, specifically, the background plasma density, b) investigate the dynamics of the branches up until the complete stopping of the streamer in the electrodynamic stage, and c) examine branching in a subthreshold field with a model initiator. Here we note only that for an initial plasma cloud of the form (2) the branching probability increases with the parameter $r_0\sqrt{\nu_{iV}/D_a}$.

[1] V. B. Gil'denburg, I. S. Gushchin, S. A. Dvinin *et al.*, Zh. Éksp. Teor. Fiz. **97**, 1151 (1990) [Sov. Phys. JETP **70**, 645 (1990)].
[2] P. V. Vedenin and N. E. Rozanov, Zh. Éksp. Teor. Fiz. **105**, 868 (1994) [JETP **78**, 465 (1994)].
[3] G. V. Naĭdis, Zh. Éksp. Teor. Fiz. **109**, 1288 (1996) [JETP **82**, 694 (1996)].
[4] P. V. Vedenin and N. A. Popov, Zh. Éksp. Teor. Fiz. **108**, 531 (1995) [JETP **81**, 286 (1995)].
[5] L. P. Grachev, I. I. Esakov, G. I. Mishin *et al.*, Zh. Tekh. Fiz. **59**, 149 (1989) [Sov. Phys. Tech. Phys. **34**, 1181 (1992)].
[6] A. L. Vikharev, A. M. Gorbachev, A. V. Kim *et al.*, Fiz. Plazmy **18**, 1064 (1992) [Sov. J. Plasma Phys. **18**, 554 (1992)].
[7] L. P. Grachev, I. I. Esakov, G. I. Mishin *et al.*, Zh. Tekh. Fiz. **64**(2), 26 (1994) [Sov. Phys. Tech. Phys. **39**, 130 (1994)].
[8] V. G. Brovkin and Yu. F. Kolesnichenko, J. Mosc. Phys. Soc. **5**, 23 (1995).

Translated by M. E. Alferieff

Cylindrical cumulation of fast ions in a ring focus of a high-power subpicosecond laser

G. S. Sarkisov

P. N. Lebedev Physics Institute, Russian Academy of Sciences, 117924 Moscow, Russia; Department of Physics, University of Nevada, Reno, NV 89557-0058, USA

V. Yu. Bychenkov and V. T. Tikhonchuk[a)]

P. N. Lebedev Physics Institute, Russian Academy of Sciences, 117924 Moscow, Russia

(Submitted 30 November 1998)
Pis'ma Zh. Éksp. Teor. Fiz. **69**, No. 1, 20–25 (10 January 1999)

A new method of cylindrical cumulation of fast ions undergoing ponderomotive acceleration at the focus of a high-power subpicosecond laser is proposed. When a laser beam is focused in a preionized gas at a ring focus, radial acceleration of ions by the ponderomotive force occurs. The ions accelerated from the inner side of the ring form a cylindrical shock wave converging toward the axis. As the shock wave cumulates, the ion density increases rapidly and the ion–ion collision probability increases along with it. A numerical simulation for a ~ 100 TW subpicosecond laser pulse predicts the generation of up to 200 keV ions and up to 100-fold volume compression of the plasma in a cylinder $\sim 1\,\mu$m in diameter. The lifetime of the dense plasma filament over the length of the laser caustic is several picoseconds. It is suggested that laser cumulation of ions be used for the production of a bright and compact subpicosecond source of fast neutrons, media for x- and γ-ray lasers, and multiply-charged ions and for the initiation of nuclear reactions.
[S0021-3640(99)00501-0]

PACS numbers: 52.50.Jm, 42.60.Jf, 42.55.Ah

The advances made in the development of the technology for generating high-power subpicosecond laser pulses opens up completely new fields of application of such pulses. Specifically, laser acceleration of particles to high energies and stimulation of nuclear reactions become possible.[1–5] In the present letter we propose a new method for producing a high-density plasma at the focus of a laser beam. The idea of the method is based on an application of ion cumulation on the axis of a cylindrical discharge[6] and a Coulomb explosion in a plasma, as predicted theoretically in Ref. 7 and recently observed experimentally in Refs. 8 and 9. A Coulomb explosion is the acceleration of ions by the electrostatic field separating the charges that arises when the ponderomotive force expells electrons from the focus of the laser radiation. In the experiments of Ref. 8, radial ejection of ions with energies up to 550 keV was obtained with a 5 TW titanium–sapphire laser with intensity $\sim 5\times 10^{18}$ W/cm^2 and duration ~ 400 fs interacting with a

helium stream. Relativistic self-focusing of the laser beam substantially increased the ponderomotive force on account of the increase an increase in the radial gradient of the intensity of the light beam inside the plasma channel. The radial acceleration of ions by the ponderomotive force at the focus of a laser beam has also been reported in Refs. 10 and 11.

In Refs. 8 and 11 the intensity of the laser beam was maximum on the axis and the ions were accelerated away from the axis of the laser beam toward the periphery. For a laser beam focused into a ring-shaped spot, some of the ions on the inner side of the ring will be accelerated in a radial direction toward the center and they will form a converging collisionless cylindrical shock wave. After a certain time has elapsed, cumulation of fast ions will occur and a high-density plasma filament will form on the axis of the laser beam. The filament can be less than one micron in diameter and $\sim 100-200\ \mu$m long, the length being determined by the length of the laser caustic. The idea of cylindrical cumulation of fast ions was formulated in Ref. 6 at the end of the 1960s for the purpose of initiating a fusion reaction, where the ions were accelerated by a cylindrical diode with a perforated cathode. The laser acceleration method has substantial advantages because there are no electrodes, the symmetry is much better, the ion energy can be conveniently controlled, and the overall power requirements are lower. The focusing of the plasma fluxes that are produced when the inner surface of a cylindrical target is irradiated with a nanosecond laser pulse has been discussed recently in Ref. 12. Neutron generation in DD reactions with laser irradiation of gas and solid targets has been reported in Refs. 13 and 14, respectively.

To accomplish efficient transfer of laser energy to the ions by means of the ponderomotive effect, it is necessary to use a uniform plasma that is transparent to laser radiation and a subpicosecond laser pulse that is powerful enough so that there will not be enough time for the ions to leave the acceleration region during the time that the pulse is applied. Otherwise, efficient acceleration of the ions will not occur. At the same time, the laser pulse should vary gradually over a distance of the order of the electronic Debye radius in order to avoid substantial energy losses due to excitation of electron plasma waves. Under these conditions the acceleration of ions with mass M and charge Z in the field of a laser beam can be described by the equation[8]

$$\frac{du_i}{dt} = -\frac{Z}{M} mc^2 \nabla_r \sqrt{1+a^2/2}, \tag{1}$$

where u_i is the ion velocity, $a = 0.85\times 10^{-9}\lambda\sqrt{I}$ is the dimensionless vector potential of the laser field, the intensity I is measured in W/cm^2, the laser wavelength λ is measured in microns, m is the electron mass, and c is the speed of light. Estimates based on Eq. (1) show that it is possible to accelerate $\sim 10^{13}$ ions to 200 keV for a caustic of length $\sim 100\ \mu$m. This requires a 100 TW neodymium laser beam with intensity 2×10^{19} W/cm^2 and duration 400 fs, and the beam must be focused to a ring 10 μm in radius and 8 μm thick (at half intensity) in deuterium gas with density $\sim 10^{20}$ cm^{-3}.

The ion energy can be controlled by varying the size of the focal ring, the intensity distribution in the focus, and the energy and duration of the laser radiation. Relativistic self-focusing of a laser beam can greatly increase the length of the caustic and, accordingly, the number of accelerated ions. Thus, in the experiments of Ref. 8 the laser channel

was ~ 1 mm long, and the results of the investigation of the ionization dynamics of the surrounding gas attested to approximately a twofold decrease in the diameter of the laser beam in the plasma as a result of self-focusing.

In the scheme proposed here, approximately half of the accelerated ions move toward the axis of the laser beam, producing a converging shock wave. The mean free path of the ions is much greater than the size of the focal ring. For this reason, as a result of cylindrical cumulation there arises on the axis a region of high density, formed by interpenetrating ion fluxes. The minimum radius is a fraction of the initial thickness of the ring of accelerated ions. On account of the sharp increase in the fast-ion density at the moment of cumulation, the yield of secondary reactions, whose rate is proportional to the product of the densities of the colliding particles, can increase sharply.

To illustrate the laser acceleration effect and the subsequent ion cumulation and to estimate the efficiency of the accompanying nuclear reactions, we performed a numerical simulation of the ion dynamics. The ions were described by the particle-in-cell method, and the electrons formed a cold neutralizing background. Initially, the stationary ions acquire an acceleration in accordance with Eq. (1), after which they coast in the radial direction. The deceleration and elastic scattering of the accelerated ions in collisions with electrons and ions were neglected, since the corresponding energy losses do not exceed 10–20% for the parameters employed in the simulation. Preionized deuterium gas with density 10^{20} cm^{-3} was chosen as the target. Laser radiation with wavelength 1.053 μm was assumed to be focused to a ring of radius $r_0 = 10\,\mu$m, and the intensity distribution in the focal spot was taken to be of the form

$$I(r,t) = I_0 (r/r_0)^4 \exp(2 - 2r^2/r_0^2 - t^2/t_0^2), \tag{2}$$

where I_0 is the maximum intensity reached at time $t = 0$, and $t_0 = 240$ fs (which corresponds to a pulse duration of 400 fs at half height[8,9]). The pulse energy was chosen as 50 J on the basis of optimization of the cross section of the reaction $D + D \rightarrow He^3 + n$.

The evolution of the radial ion density distribution is presented in Fig. 1. In the initial stage, plasma is displaced from the region of the laser beam, and two collisionless shock waves are formed. One shock wave consists of ions from the inner side of the ring and moves toward the center; the other shock wave (not shown in Fig. 1) moves toward the periphery. The high narrow peaks show the trajectories of the fast ions, which move toward the axis, collapse, and then move away from the axis. Cumulation of fast ions on the axis occurs 1.2 ps after the maximum of the laser pulse. After another 0.1–0.2 ps have elapsed, the maximum volume compression reaches a value of the order of 2000 in a small region less than 0.1 μm in diameter. It is possible that taking into account the transverse motion and collisions of fast ions with electrons and ions near the axis of the laser beam will lead to scattering of the ions and, in consequence, some decrease in the maximum compression of the plasma and increase in the diameter of the compressed region. However, this has no effect on the yield of secondary reactions and the dynamics of the compression process will remain essentially unchanged. The lifetime of the dense plasma filament is several picoseconds, which is much longer than the transit time of a fast ion across the compressed region. This is explained by the fact that the ponderomotive acceleration produces a spectrum of ions, and the slower ions reach the axis with a delay.

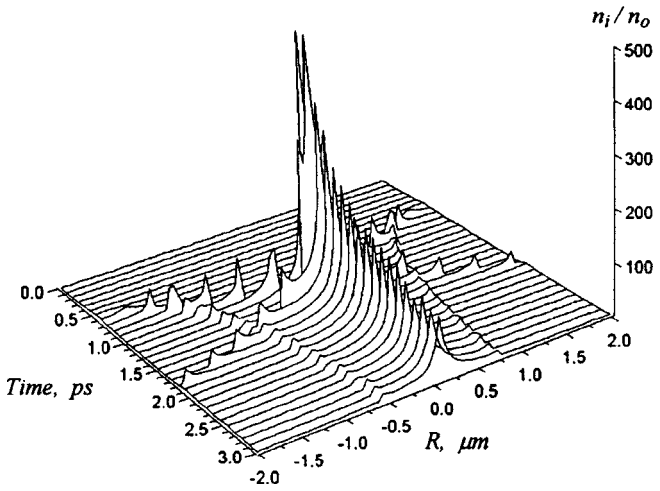

FIG. 1. Radial deuteron density distribution n_i/n_0, normalized to the initial plasma density, at different times. The energy of the laser is 50 J, the initial gas density is 10^{20} cm^{-3}, and all other parameters are given in the text. The narrow crests show the trajectory of the fastest ions forming the front of a cylindrical shock wave.

The time dependence of the average compression ratio for the plasma in a 1 μm in diameter region near the axis and the neutron yield per unit length are presented in Fig. 2a. The maximum velocity of ions moving toward the center is $\sim 4.2\times 10^8$ cm/s, which corresponds to energy $\sim$200 keV. The maximum average compression reaches 130, and the neutron yield $\sim 2.3\times 10^7$ cm^{-1}. The extremely short duration $\sim$0.1 ps of the neutron

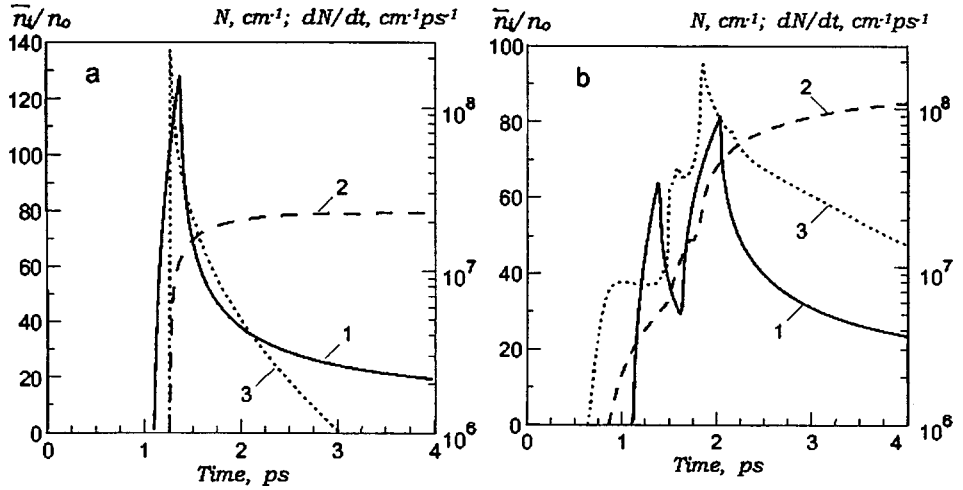

FIG. 2. Compression ratio of the plasma in a region 1 μm in diameter near the axis (*1*), the neutron yield $N(t)$ in the fusion reaction (2), and the neutron production rate dN/dt (*3*) for pure deuterium (a) and a mixture with different parts deuterium and tritium (b) as functions of time. The computational parameters are given in the caption to Fig. 1 and in the text.

pulse is interesting. It is comparable to the transit time of the fastest ions through the compressed region.

The neutron yield in such a scheme can be increased by replacing pure deuterium by a deuterium–tritium mixture, since the cross section of the DT reaction is much larger. But then ion cumulation does not increase the neutron yield as efficiently, since on account of their mass difference deuterons and tritons acquire a different velocity under the ponderomotive force and therefore reach the axis at somewhat different times. The dynamics of near-axis compression and of the neutron yield for a 1:1 DT mixture are shown in Fig. 2b. All laser beam and plasma parameters are the same as in the preceding case (Fig. 2a). The two peaks on the compression curve correspond to cumulation first of deuterium and then the tritium. On account of the kinetic separation of ions, the neutron pulse is delayed with respect to the first cumulation and has a longer duration than in the case of the DD reaction. However, on account of the large cross section of the reaction the total neutron yield is approximately 5 times higher, reaching 10^8 cm^{-1}.

The advantage of the laser ion acceleration and cylindrical ion cumulation scheme considered above lies in the fact that the neutron pulse has an extremely short duration and the transverse size of the generation region is small. Correspondingly, for a 1 mm long laser beam caustic the efficiency of the conversion of laser energy into neutrons is of the order of 10^5 neutrons/J or 2×10^{-7}, since the energy of each neutron is $\sim$14 MeV. The power of such a picosecond neutron source is very substantial, $\sim$10 MW, and the source is extremely small in size. The efficiency of such a neutron source increases appreciably with the power of the laser pulse. For a petawatt laser pulse[4] with 1 kJ energy, 1 μm wavelength, and 1 ps duration focused to a ring with radius $r_0=20\,\mu$m with the intensity distribution (2), the expected neutron yield in the DD reaction in the scheme proposed is already of the order of 4×10^8 cm^{-1} at an average compression of $\sim$2000 in a cylinder 1 μm in diameter. The maximum energy of fast ions is then greater than 600 keV.

The quite high efficiency of the conversion of laser energy into neutrons under the conditions of cylindrical cumulation of the accelerated ions advantageously distinguishes the scheme proposed here from a previously used scheme,[13] where the DD reaction was initiated by a diverging flux of fast ions, flying out of the channel produced by the laser beam and propagating in a gas plasma produced in advance. In the experiment of Ref. 13 the average neutron yield was 700 neutrons/J. This is probably due to the low efficiency of laser acceleration of ions in the channel. At the same time, the laser acceleration of ions in a rarefied plasma is probably less efficient than in a solid target, though it gives a neutron pulse of shorter duration. The results obtained in Ref. 14, where $\sim10^9$ neutrons were obtained by focusing a laser pulse with intensity $\sim10^{19}$ W/cm^2 and duration $\sim$1 ps on the surface of deuterated polystyrene (C_8D_8).

In conclusion, we note that the method, examined above, of cylindrical cumulation of ions by a subpicosecond ring-shaped laser pulse can be implemented on existing short-pulse $\sim$100 TW lasers, and it can be used to generate a neutron pulse for other applications. For example, the lifetime of the plasma produced by cumulation on the axis is quite long, of the order of 10 picoseconds. It will contain a large number of ions in excited states $\sim10^{12}-10^{13}$ cm^{-1}. For this reason, with an appropriate choice of gas and target the compressed plasma can be used as an amplifying medium for x- or γ-ray lasers and for initiation of nuclear reactions.

We thank V. N. Novikov for assisting in the development of the numerical program. This work was partially supported by the Russian Fund for Fundamental Research.

[a)]e-mail: tikhon@sci.lebedev.ru

---

[1] B. Luther-Davies, E. G. Gamaly, Y. Wang *et al.*, Laser Phys. **1**, 325 (1991).
[2] D. Umstadter, S. Y. Chen, A. Maksimchuk *et al.*, Science **273**, 472 (1996).
[3] P. L. Shkolnikov, A. E. Kaplan, A. Pukhov, and J. Meyer-ter-Vehn, Appl. Phys. Lett. **71**, 3471 (1997).
[4] G. A. Mourou, C. P. J. Barty, and M. D. Perry, Phys. Today **51**, No. 1, 22 (1998).
[5] D. A. Gryaznykh, Ya. Z. Kandiev, and V. A. Lykov, JETP Lett. **67**, 257 (1998).
[6] M. Gryzinski, J. Novikowski, M. Sadowski *et al.*, Plasma Phys. Controlled Fusion **10**, 450 (1968).
[7] N. H. Burnett and G. D. Enright, IEEE J. Quantum Electron. **QE-26**, 1797 (1990).
[8] G. S. Sarkisov, V. Yu. Bychenkov, V. T. Tikhonchuk *et al.*, JETP Lett. **66**, 828 (1997).
[9] S. Y. Chen, G. S. Sarkisov, A. Maksimchuk *et al.*, Phys. Rev. Lett. **80**, 2610 (1998).
[10] K. Krushelnick, A. Ting, C. I. Moore *et al.*, Phys. Rev. Lett. **78**, 4047 (1997).
[11] J. Fuchs, G. Malka, J. C. Adam *et al.*, Phys. Rev. Lett. **80**, 1658 (1998).
[12] G. A. Askar'yan, S. V. Bulanov, and I. V. Sokolov, ''Inverted cylindrical laser corona,'' in *Abstracts the 25th Zvenigorod Conference on Plasma Physics and Controlled Thermonuclear Fusion* [in Russian], Moscow Physical Society Press, Moscow, 1998, p. 148.
[13] G. Pretzler, A. Saemann, A. Pukhov *et al.*, Phys. Rev. E **58**, 1165 (1998).
[14] P. A. Norreys, A. P. Fews, F. N. Beg *et al.*, Plasma Phys. Controlled Fusion **40**, 175 (1998).

Translated by M. E. Alferieff

Anisotropy of the upper critical field and specific heat in V_3Si — a superconductor with cubic symmetry

M. N. Khlopkin[a)]
Kurchatov Institute Russian Science Center, 123182 Moscow, Russia

(Submitted 23 November 1998)
Pis'ma Zh. Éksp. Teor. Fiz. **69**, No. 1, 26–29 (10 January 1999)

The specific heat of a V_3Si single crystal ($T_c = 17$ K, $H_{c2} = 20$ T) in magnetic fields up to 8 T is investigated experimentally for three orientations of the field relative to the crystallographic directions — $H \| \langle 001 \rangle$, $H \| \langle 110 \rangle$, and $H \| \langle 111 \rangle$. Both the upper critical magnetic field and the specific heat of the mixed state are observed to depend on the orientation of the magnetic field relative to the crystallographic directions (anisotropy): The critical field reaches its maximum value and the specific heat its minimum value in a field along the $\langle 001 \rangle$ direction. The anisotropy scale in both phenomena increases as the magnetic field and reaches 3% in a 6 T field. The interrelationship of the upper critical field anisotropy and the specific-heat anisotropy in type-II superconductors is studied. It is shown that the anisotropy of the specific heat in the mixed state in weak fields can serve as a criterion for nontrivial pairing.
[S0021-3640(99)00601-5]

PACS numbers: 74.25.Ha, 74.25.Bt

A number of unusual phenomena observed in the last few years in high-temperature superconductors suggest the possible manifestation of unconventional mechanisms of superconductivity, including mechanisms involving unconventional pairing, for example, with *d* symmetry of the order parameter. For example, in Refs. 1–5 a nonlinear, close to square-root, magnetic-field dependence of the specific heat in the mixed state was observed, and it was interpreted in accordance with the theoretical works[6] as a manifestation of *d* pairing. However, later, a similar behavior of the specific heat was also observed[7] in a superconductor with *s* pairing — V_3Si. For this reason, control investigations of conventional superconductors where *s* pairing is known to exist are required in order to make a more accurate interpretation of such phenomena. It is desirable that their superconducting properties be as close as possible to those of high-temperature superconductors. The most suitable objects for such control measurements are compounds with the A-15 structure, which have high critical temperatures and fields and a short coherence length. Examples are V_3Si and Nb_3Sn.

In Ref. 8 a specific-heat anisotropy of the high-temperature superconductor $La_{2-x}Sr_xCuO_4$ in the mixed state with the magnetic field oriented in the a–b plane was observed, and it was interpreted to be an indication of *d* pairing.

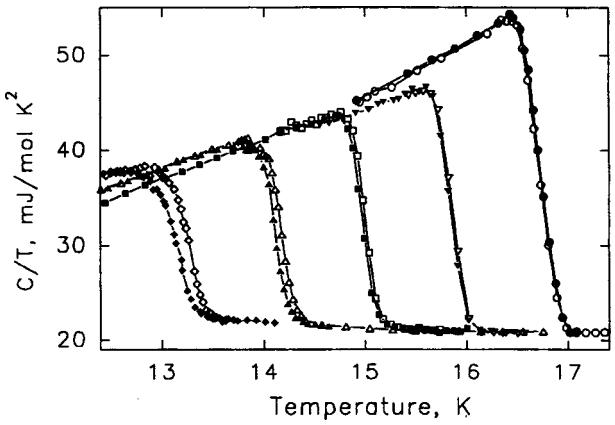

FIG. 1. Specific heat of a V_3Si single crystal in magnetic fields 0, 2, 4, 6, and 8 T for two orientations relative to the crystallographic directions: open symbols — $H\|\langle 100\rangle$, filled symbols $H\|\langle 111\rangle$; ○ — $H=0$; ∇—$H=2$ T; □ — $H=4$ T; Δ — $H=6$ T; ◇ — $H=8$ T.

In the present work the upper critical magnetic field and specific heat of a V_3Si single crystal in magnetic fields were investigated experimentally, their anisotropy was observed, and the dependence of the anisotropy on the magnitude of the magnetic field was studied in fields up to 8 T.

The V_3Si single crystal was prepared by the technology described in Ref. 9. The superconducting transition temperature, determined by the standard four-contact method, was 17.15 K, the width of the transition was of the order of 0.2 K, and the resistance ratio $\rho_{300K}/\rho_{18K}=16$. The directions of the crystallographic axes were determined according to the x-ray diffraction patterns, and the error in the orientation of the crystal mounted in a calorimeter did not exceed 5°. The specific heat of a 1.5 g sample was measured by the adiabatic method,[10] and the measurement error did not exceed 1%.

The results of the specific-heat measurements performed in the temperature interval 13–17 K are presented in Fig. 1. Sharp jumps, corresponding to a superconducting transition in a magnetic field (more accurately — a transition from a mixed state to a normal state), were observed in the temperature dependence of the specific heat. This made it possible to determine the temperature dependence of the upper critical magnetic field. One can see that the temperature of the jump in the specific heat depends not only on the magnitude but also on the orientation of the magnetic field. The orientation dependence (anisotropy) increases rapidly with the magnetic field: The critical temperature of the superconducting transition varies essentially linearly with the magnetic field, while the difference of the critical temperatures for different field orientations $\delta T_c = T_c(H\|\langle 001\rangle) - T_c(H\|\langle 111\rangle)$ increases quadratically and reaches 0.16 K in an 8 T field. Thus the scale of the relative anisotropy of the upper critical field $\delta T_c/(T_c(H=0) - T_c(H))$ increases linearly with the magnetic field. Extrapolating this dependence to H_{c2} at zero temperature gives a value of the order of 20%.

It should be noted that the anisotropy of the critical magnetic field in V_3Si was investigated previously in Refs. 11–14, but no temperature dependence of the anisotropy was noted. The anisotropy of the critical magnetic field in crystals with cubic or tetrago-

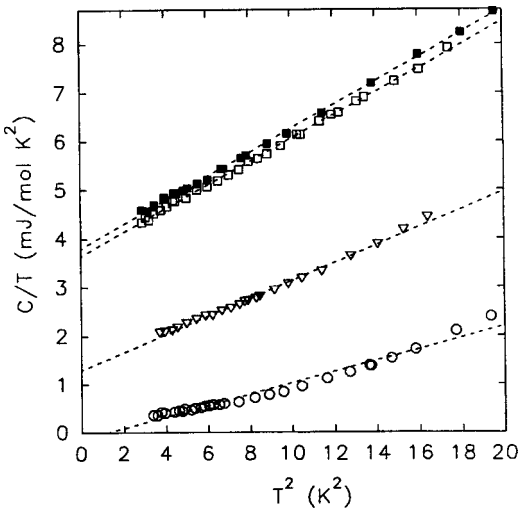

FIG. 2. Temperature dependence of the specific heat at low temperatures in magnetic fields H with different orientations: open symbols — $H\|\langle 100\rangle$, filled symbols — $H\|\langle 111\rangle$; ○ — $H=0$; ∇ — $H=2$ T; □ — $H=6$ T.

nal symmetry is a nontrivial phenomenon, since the effective mass tensor is isotropic in such symmetry. However, when second-order effects, such as Fermi velocity anisotropy and the electron–phonon interaction, are taken into account, anisotropy of the upper critical magnetic field is obtained in models with s pairing,[15] and its magnitude is found to depend on the temperature and vanishes at $T=T_c$, which corresponds to that observed in V_3Si in the present work. The criterion of nontrivial pairing, however, is the presence of H_{c2} anisotropy at temperatures close to T_c (Ref. 16), i.e., in weak fields.

It is interesting to note that in one of the models investigated in Ref. 15, anisotropy also leads to an anomalous temperature dependence, with positive curvature, of the upper critical field. The physical meaning of this mechanism is that the magnetic field partially isotropizes the order parameter, which decreases the effective critical parameters. Therefore a stronger field dependence of the critical temperature $T_c(H)$, a larger value of the derivative dT_c/dH, and therefore a lower value of its reciprocal — the temperature derivative of the upper critical field dH_{c2}/dT — should be observed in the region of isotropization of the order parameter, and this process is more intense in weak fields.

The temperature dependence of the specific heat C in the mixed state is shown in Fig. 2 in the coordinates C/T versus T^2 for different values and orientations of the magnetic field. A magnetic field increases the specific heat of the mixed state, and a dependence on the magnetic field orientation (anisotropy) is also observed: The specific heat of the mixed state is minimum for an orientation in the $\langle 001\rangle$ direction and maximum for $\langle 111\rangle$. For a field oriented in the $\langle 110\rangle$ direction, the experimental data on both the specific heat and critical magnetic field fall between the data for the orientations $\langle 001\rangle$ and $\langle 111\rangle$.

The scale of the relative specific-heat anisotropy increases with the magnetic field: It equals 3% in a 6 T field and decreases to zero as the field approaches zero.

In the standard theory of superconductivity,[17–19] the magnetic-field dependence of

the specific heat of the mixed state at low temperatures is nearly linear $(C(H)-C(H=0))/T=\gamma H/H_{c2}$, where γ is the Sommerfeld coefficient, characterizing the specific heat of the electronic system in the normal (nonsuperconducting) state. On the basis of this relation one would expect that the scale of the specific heat anisotropy at low temperatures will not depend on the applied field and will correspond to the scale of the anisotropy of H_{c2} at zero temperature, i.e., it will be of the order of 20%.

Comparing our experimental data on the specific heat and critical field shows that the scale of the specific-heat anisotropy and the character of its dependence on the magnitude of the magnetic field are very close to those for the critical magnetic field taken at the same values of the external magnetic field but at very different temperatures. Hence it can be concluded that the anisotropy of the specific heat of the mixed state is determined not by the temperature but by the applied magnetic field.

In Ref. 5 the thermodynamics of the mixed state of a superconductor is analyzed on the basis of quite general model-free assumptions and it is shown that the magnetic-field dependence of the specific heat $C(H)$ of the mixed state is more complicated and is related with the temperature dependence of the critical magnetic field $H_{c2}(T)$ by the condition of entropy balance, which leads to the relation (see Ref. 5)

$$(d\gamma^*/dH)\cdot(dH_{c2}/dT)=-p\Delta C(H)/T_c^2(H). \tag{1}$$

Here $\gamma^*=C/T$ as $T\to 0$, p is a factor of the order of 1, and $\Delta C(H)$ and $T_c(H)$ are, respectively, the magnitude of the jump in the specific heat at the transition from the mixed to the normal state in the magnetic field H and the temperature of this transition.

The application of this relation to a superconducting transition in low fields, where in the presence of s pairing dH_{c2}/dT, $\Delta C(H)$, and $T_c(H)$ are almost isotropic, leads immediately to the conclusion that $d\gamma^*/dH$, which describes the specific heat of the mixed state, must also be almost isotropic in weak fields, as is in fact observed in the present experiment in V_3Si. In strong fields and at low temperatures the specific-heat anisotropy can also be observed in the presence of s pairing, as happens in V_3Si.

In summary, the specific-heat anisotropy in weak fields but not that in strong fields can serve as a criterion of nontrivial pairing.

I thank V. A. Marchenko for providing the sample.

This work is supported by the Scientific Council on the Problem of High-Temperature Superconductivity, and it was performed as part of Project 96039 of the State Scientific and Technical Program ''Topical Problems of Condensed-Matter Physics'' category ''Superconductivity.''

[a)]e-mail: khlopkin@ismain.isssph.kiae.ru

[1]K. A. Moler, D. J. Baar, J. S. Urbach *et al.*, Phys. Rev. Lett. **73**, 2744 (1994).
[2]K. A. Moler, D. J. Baar, Ruixing Liang *et al.*, J. Supercond. **8**, 571 (1995).
[3]R. A. Fisher, D. A. Wright, J. P. Emerson *et al.*, Physica C **252**, 237 (1995).
[4]B. Revaz, A. Junod, A. Mirmelstein *et al.*, Czech. J. Phys. **46**, Suppl S3, 1205 (1996).
[5]M. N. Khlopkin, G. Kh. Panova, N. A. Chernoplekov *et al.*, Zh. Éksp. Teor. Fiz. **112,** 1386 (1997) [JETP **85**, 775 (1997)].
[6]G. E. Volovik, JETP Lett. **58**, 469 (1993).
[7]A. P. Ramirez, Phys. Lett. A **211**, 59 (1996).

[8] M. N. Khlopkin, G. Kh. Panova, N. A. Chernoplekov, and A. A. Shikov, JETP Lett. **66**, 715 (1997).
[9] B. N. Tret'yakov, V. A. Marchenko, V. B. Kuritsyn, and B. N. Kodess, Zh. Éksp. Teor. Fiz. **65,** 1551 (1973) [Sov. Phys. JETP **38**, 772 (1974)].
[10] M. N. Khlopkin, N. A. Chernoplekov, and P. A. Cheremnykh, Preprint IAÉ-3549/10 [in Russian], Moscow (1982).
[11] M. Pulver, Z. Phys. **257**, 22 (1972).
[12] E. J. Kramer and G. S. Knapp, J. Appl. Phys. **46**, 4595 (1975).
[13] S. Foner and E. J. McNiff, Appl. Phys. Lett. **32**(2), 122 (1978).
[14] M. N. Khlopkin and V. A. Marchenko, Fiz. Tverd. Tela (Leningrad) **25,** 3691 (1983) [Sov. Phys. Solid State **25**, 2125 (1983)].
[15] W. Pitscheneder and E. Schachinger, Phys. Rev. B **47**, 3300 (1993).
[16] L. P. Gor'kov, JETP Lett. **40**, 1155 (1984).
[17] C. J. Gorter, H. Van Beelen, and R. De Bruyn Outboter, Phys. Lett. **8**, 13 (1964).
[18] K. Maki, Phys. Rev. A **139**, 702 (1965).
[19] A. A. Abrikosov, *Fundamentals of the Theory of Metals*, North-Holland, Amsterdam, 1988; Nauka, Moscow, 1987.

Translated by M. E. Alferieff

Optical detection of the absorption of acoustical phonons by a two-dimensional electron gas in a magnetic field

V. E. Zhitomirskiĭ,[a)] O. V. Volkov, and I. V. Kukushkin
Institute of Solid-State Physics, Russian Academy of Sciences, 142432 Chernogolovka, Russia

S. Rozhko
Max-Planck-Institut für Festkörperforschung, 70569 Stuttgart, Germany

W. Dietsche
School of Physics and Astronomy, University of Nottingham, Nottingham NG7 2Rd, United Kingdom

(Submitted 27 November 1998)
Pis'ma Zh. Éksp. Teor. Fiz. **69**, No. 1, 30–35 (10 January 1999)

The effect of absorption of nonequilibrium acoustical phonons on the intensity of recombination of a two-dimensional electron gas in a magnetic field is investigated. The nonequilibrium acoustical phonons are emitted in the relaxation of electrons in a tunnel junction deposited on the back side of a sample with a two-dimensional electronic channel. It is demonstrated that the optical signal showing the intensity of the recombination of nonequilibrium electrons from a photoexcited size-quantization subband can serve as a sensitive detector of acoustical phonons. Because the general heating of two-dimensional carriers and the intersubband transitions stimulated by the absorption of nonequilibrium acoustical phonons lead to effects of different sign, the useful signal can be discriminated unambiguously. © *1999 American Institute of Physics.* [S0021-3640(99)00701-X]

PACS numbers: 73.20.Mf, 73.20.Dx, 85.30.Mn

1. The investigation of the spectrum of the collective excitations of a two-dimensional (2D) electron gas in the ultraquantum limit is one of the most pressing and interesting problems in the physics of low-dimensional systems. The energy of acoustical phonons in GaAs with wavelength of the order of the magnetic length (100 Å) is 15 K, which makes the phonon method unique for investigating features in the dispersion of collective excitations suc as, for example, the magnetoroton in the fractional quantum Hall effect regime.

The main problem in using the phonon method for measurements on 2D electronic channels is the high sensitivity of the measured quantities to changes in temperature. The electrical power released in the sample for generating high-energy phonons also leads to an undesirable general increase of the lattice temperature. From this standpoint, a tunnel

junction[1] has an advantageous over a thermal source in terms of the efficiency of conversion of electrical power into a flux of high-energy phonons. The spectrum of acoustical phonons emitted as a result of energy relaxation of tunneling carriers is determined by the voltage V applied to the junction. On the high-energy side the spectrum of emitted phonons has a cutoff near $\hbar\omega_{\rm ph}=$ eV. The thermal power released in this method (with a fixed spectrum of nonequilibrium phonons) can be varied over wide limits by varying the tunneling resistance.

In the present work we investigated the effect of acoustical phonons, generated by a tunnel junction, on the intensity of the recombination radiation line of the nonequilibrium electrons of a photoexcited subband in an isolated GaAs/AlGaAs heterojunction. For sufficiently high electron densities in the ground-state subband (about 4.8×10^{11} cm^{-2}) the Fermi level of the system of 2D carriers lies directly adjacent to the bottom of the next size-quantization subband. Photoexcited electrons arrive in the 2D channel from the bulk of the GaAs, replacing the 2D carriers lost as a result of recombination. Localization of the photoexcited carriers in the z direction occurs in the course of relaxation between the size-quantization subbands. The relaxation between the first excited and zeroth subbands is accompanied by the emission of acoustical phonons with characteristic quasimomenta of the order of the Fermi momentum k_f. When the energy gap between the bottom of the first size-quantized subband and the Fermi level of a 2D electronic system is less than the energy of the acoustical phonons $E_{\rm ph}=\hbar sk_f\simeq0.4$ meV, a bottleneck forms for intersubband relaxation processes. The main channel for loss of photoexcited carriers becomes their recombination with photoexcited holes.[2] The absorption of acoustical phonons is an alternative channel for relaxational loss (see inset in Fig. 2) and decreases the intensity of recombination of nonequilibrium electrons in a photoexcited subband.

2. In the present work we investigate a sample with a 2D electronic channel in an isolated GaAs/AlGaAs heterojunction with a monolayer of acceptors laid down during growth of the structure at a distance of 300 Å from the heterointerface, was investigated.[3] Since the overlap of the wave functions of the 2D electrons in the main subband and a hole on a distant neutral acceptor is small, the lifetimes of the photoexcited holes is long (hundreds of nanoseconds). The extent of the wave function of the 2D electrons of a photoexcited subband is much greater than that of the wave function of the zeroth subband. This gives a much better overlap of the electrons with a hole localized on a distant acceptor, and for this reason their radiative recombination lifetime is of the order of 30 ns.[2] In the spectra of the recombination radiation the linehat corresponding to the photoexcited size-quantization subband can therefore have a much higher intensity than that for electrons in the ground-state subband, even though the density of nonequilibrium carriers in the photoexcited subband is several orders of magnitude lower than the density of equilibrium 2D electrons.

Optical excitation of the experimental sample was accomplished with a tunable Ti:Sp laser, and the radiative recombination was detected with a CCD camera. A spectral resolution of 0.03 meV was achieved with a Ramanor U-1000 spectrometer.

An Al–Al_2O_3–Al (1 mm^2, 0.6 Ω) tunnel junction was deposited on the back side of an experimental sample 0.5 mm thick in a 10^{-6} mbar vacuum, and the oxidation of the Al was carried out in a plasma discharge in an oxygen atmosphere at 3×10^{-3} mbar pressure. The Al films were 50 nm thick, which corresponded to an Ohmic resistance of

0.5 Ω per square. To generate nonequilibrium acoustical phonons, we passed a 30 mA current through the tunnel junction. The applied electrical power of 1 mW was comparable to an optical pump power of 2 mW and did not produce appreciable heating of the sample at temperature 1.4 K. Phonon absorption was detected according to the change in the intensity of the luminescence of the 2D electrons.

3. Figure 1 shows the magnetooscillations, measured at 1.4 K, of the intensity of the recombination of electrons in the photoexcited subband. The density of the 2D electrons in the ground-state subband was 4.8×10^{11} cm^{-2}. A diagram of the magnetic-field dependence of the energy of optical transitions which was obtained for the experimental sample is presented at the bottom of Fig. 1b. It consists of a set of spectra measured with a small magnetic-field step. An example of such spectra is presented in Fig. 1c for several values of the magnetic field. The contrast of the diagram reflects the intensity of recombination, so that a high intensity corresponds to a light color. Black corresponds to a weak signal. In Ref. 2, it was demonstrated that there is a single-valued relation between the magnetooscillations shown in Fig. 1a and the oscillations of the relaxation time of photoexcited carriers as the zeroth Landau level 0_e^1 of the first subband crosses empty Landau levels N_e^0 of the ground-state subband (see Fig. 1b). The relaxation time of nonequilibrium electrons from the excited subband into the ground-state subband increases as the splitting between the subband and the closest Landau level decreases, just as in the case of zero magnetic field. The magnetooscillations of the relaxation time give rsie to sharp maxima of the recombination intensity, with a period (in terms of the reciprocal of the magnetic field) equal to the ratio of the intersubband splitting (E_{10}) to the electron cyclotron energy ($\hbar\omega_c^e$).

Figure 2b shows the magnetic field diagram of the effect of phonons on the intensity of the 2D-carrier recombination radiation. It was obtained as the difference of the intensities in the recombination luminescence spectra with and without excitation of acoustical phonons in the experimental sample. An example of such difference spectra is presented in Fig. 2c for several characteristic values of the magnetic field. The phonon signal did not exceed 1% of the optical signal in the entire range of magnetic fields. It should be noted that the detected signal at the spectral positions corresponding to Landau levels of the ground-state subband, is due exclusively to the change in the shape of the well as a result of repopulation of the photoexcited subband. For proof, we performed similar measurements on the same sample with a substantially lower 2D-electron density. The channel was emptied by illuminating the sample with 4880 Å laser light, which is absorbed in the AlGaAs layer.[3] At lower densities the distance between the bottom of the subband and the Fermi level of the system becomes greater than 5 meV, and intersubband relaxation is rapid, so that the intensity of the recombination line of the electrons of the photoexcited subband becomes negligibly small.

The intensity change at the spectral position of the photoexcited size-quantization subband as a result of phonon illumination and as a result of a change in the temperature of the sample by 0.5 K is shown in Fig. 2a. Comparing the two curves in Fig. 2a, shows that the effects due to thermal heating and absorption of high-energy phonons are of different sign. This situation has no analogs in the literature and is an essential feature of the experimental object. The temperature dependence of the intensity of recombination of the electrons of the photoexcited subband is determined by two basic mechanisms. The first one is an increase in the population of the photoexcited subband as a result of the

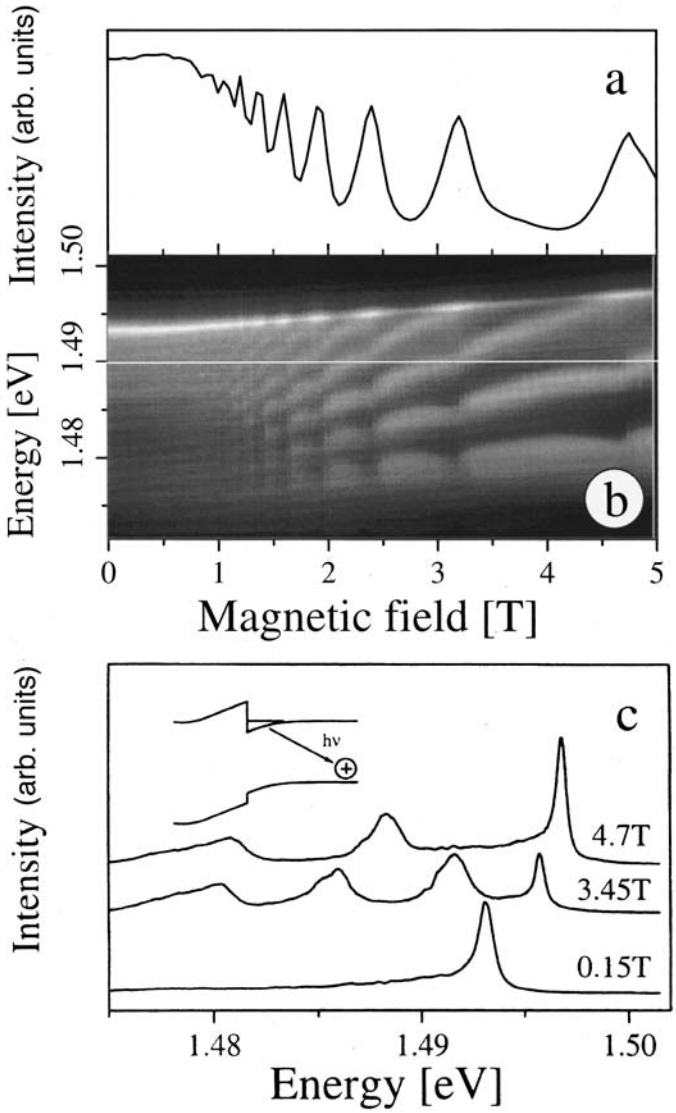

FIG. 1. Magnetooscillations of the intensity of recombination of the electrons of a photoexcited subband measured at 1.4 K (a). The 2D electron density of the ground-state subband is 4.8×10^{11} cm^{-2}. Diagram of the magnetic-field dependence of the energy of optical transitions measured for the experimental sample (b). The diagram is a set of spectra measured with a small magnetic-field step. An example of such spectra is presented for several values of the magnetic field (c). The contrast of the diagram reflects the intensity of recombination, so that high intensity corresponds to a light color. Black corresponds to a weak signal. Inset: Diagram of optical transitions in an isolated heterojunction with a delta-layer of acceptors.

broadening of the Fermi distribution function of the 2D electrons in the ground-state subband with increasing electron temperature. The second one is a decrease in the density of nonequilibrium carriers due to the acceleration of the intersubband relaxation as a result of the absorption of high-energy phonons. In doped systems, the first mechanism

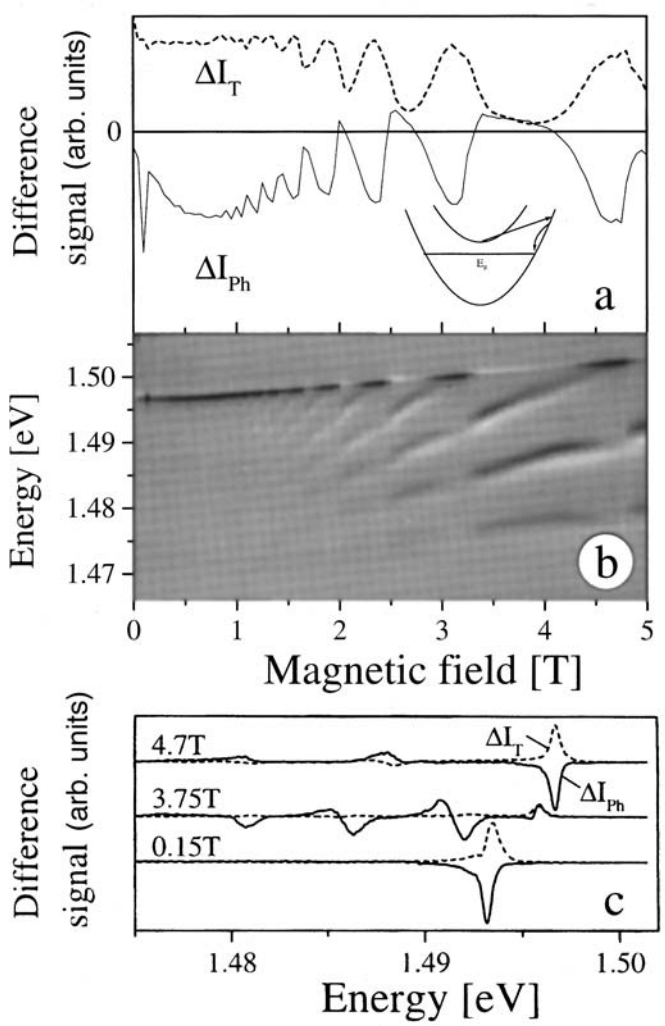

FIG. 2. Variation of the intensity at the spectral position of the photoexcited size-quantization subband as a result of both phonon illumination and a change in the temperature of the sample by 0.5 K (a). The magnetic-field diagram of the effect of phonons on the intensity of the recombination radiation of two-dimensional carriers (b). The diagram was obtained as the difference of the intensities in the recombination luminescence spectra with and without excitation of acoustical phonons in the experimental sample. An example of such difference spectra is presented for several characteristic values of the magnetic field (c). Inset: Diagram of intersubband transitions of photoexcited carriers with absorption of nonequilibrium acoustical phonons in weak magnetic fields.

— a change in the 2D-electron statistics — is much stronger than the second one, and only the phonon method permits distinguishing the second mechanism in a pure form. The use of a tunnel junction as a phonon generator is decisive for preventing lattice heating, since the undesirable lattice heating can completely mask phonon absorption effects, as happens in investigations of the temperature dependence. We performed test measurements in which the same electrical power was released by passing a current

either through the tunnel junction or through the bottom resistive film of the tunnel junction. In the latter case the signal due to heating of the sample was measured. In this way one can discriminate the useful signal, but for our object the heating signal was at least an order of magnitude weaker in all fields than the phonon signal, so that the experimental results presented above need no correction.

4. Two features in weak fields can be seen clearly near 0.15 and 0.55 T in the magnetic-field dependence of the phonon-induced signal (Fig. 2a). They are observed despite the fact that in the experiment acoustical phonons with all possible energies and propagation directions are excited. This situation arises because of the selectivity of the intersubband transitions with respect to the quasimomentum of the absorbed acoustical phonons. Since the Fermi velocity v_f of the 2D electrons in the ground-state subband is two orders of magnitude higher than the velocity of sound in GaAs, intersubband transitions are possible only with absorption of acoustical phonons with in-plane quasimomenta of the order of the Fermi momentum k_f. The position 0.15 T of the first resonance with respect to the magnetic field approximately corresponds to the intersubband cyclotron resonance, where the frequency of the absorbed phonon is equal to the cyclotron frequency of electrons in the photoexcited subband and the electrons are in temporal resonance with the acoustic wave. The frequency of the phonons whose absorption gives rise to intersubband relaxation is $\omega_{\rm ph}=sk_f\simeq 600$ GHz for the given 2D electron density in the ground-state subband. Equality of the cyclotron frequency $\omega_c=eB/m$ and $\omega_{\rm ph}$ occurs in the magnetic field $B=0.2$ T, which agrees well with the experiment. Therefore we infer that the first minimum is associated with the resonance amplification of phonon-induced intersubband transitions from an excited into the ground-state subband via a virtual cyclotron transition in the excited subband.

In somewhat higher magnetic fields it is possible to satisfy another resonance condition, where the magnetic length becomes of the order of the wavelength of the characteristic phonons — $2\pi/k_f$. Such an estimate gives for the magnetic field a value 0.51 T, which corresponds to the second feature in weak magnetic fields in Fig. 2a. We infer that phonon absorption is intensified on account of such geometric resonance, and hence the phonon-induced intersubband transitions of photoexcited carriers are accelerated. The classical analog of a resonance of this type is the well-known geometric resonance, where the electron cyclotron diameter equals the phonon wavelength. In this case, the electrons always remain in a region of constant phase and efficiently extract energy from the ultrasonic wave.

5. In summary, in the present work the existence of cyclotron and geometric resonances for absorption of nonequilibrium acoustical phonons was demonstrated for phonon-induced intersubband transitions. In high magnetic fields, the intersubband transitions between Landau energy levels with the same energy values but from different subbands (Fig. 2a) are caused by absorption of phonons with $1/k_{\rm ph}\simeq l_H\cdot(N/2)^{1/2}$, where N is the number of the Landau level in the ground-state subband. The detection of the absorption of such phonons by 2D carriers in our experiments demonstrates the exceptional possibilities of our phonon method for investigating features in the spectra of the collective excitations of a system of 2D electrons in the fractional quantum Hall effect regime with $k\cdot l_H=1$.

We thank K. Ploog for providing the samples of an isolated heterojunction. This work was supported by Deutsche Forschungsgemeinschaft (DFG), a Russian Fund for

Fundamental Research Grant No. 98-02-04079, and a grant from the Government Program (GNTP FTNS) ''Nanostructures.''

[a)]e-mail: zhitomir@issp.ac.ru

---

[1] S. Roshko, V. Zhitomirsky, J. Cooper *et al.*, Physica B **219**, 16 (1996).
[2] A. F. Dite, I. V. Kukushkin, V. B. Timofeev *et al.*, JETP Lett. **54**, 642 (1991).
[3] I. V. Kukushkin, K. von Klitzing, K. Ploog, and V. B. Timofeev, Phys. Rev. B **40**, 7788 (1989).

Translated by M. E. Alferieff

Equation of state and elastic properties of lithium: Isotope effects

E. L. Gromnitskaya, O. V. Stal'gorova, and S. M. Stishov
Institute of High-Pressure Physics, Russian Academy of Sciences, 142092 Troitsk, Moscow Region, Russia

(Submitted 30 November 1998)
Pis'ma Zh. Éksp. Teor. Fiz. **69**, No. 1, 36–40 (10 January 1999)

The equations of state and elastic properties of the lithium isotopes Li^6 and Li^7 at high pressures are investigated at a temperature of 76 K by a pulsed ultrasonic method. Proofs of the existence of appreciable quantum contributions to the pressure and elastic moduli of lithium are given. © *1999 American Institute of Physics.*
[S0021-3640(99)00801-4]

PACS numbers: 64.30+t, 62.20.Dc

The effect of the isotopic composition on the properties of matter is a manifestation of the quantum laws of nature. Indeed, according to Heisenberg's uncertainty principle, a particle confined in a bounded region of space possesses kinetic energy inversely proportional to its mass. This leads to the existence of the so-called zero-point energy E_z and the appearance of isotope effects in bound, including condensed, systems. To observe quantum effects of this kind experimentally, certain conditions must be satisfied. For example, it is obvious that the temperature T of the system under study should not be high compared to the Debye temperature Θ_D, i.e., $T/\Theta_D \leqslant 1$. At the same time, the zero-point energy E_z of the system should be appreciable compared to the total energy or the cohesive energy E of the system:

$$E_z/|E| \cong \Theta_D/|E| > \delta, \tag{1}$$

where δ is a small quantity whose numerical value is determined by the specific experimental conditions. The present letter is devoted to an experimental investigation of the equation of state of lithium, which, on account of its low atomic mass, is a natural (and nearly the only) candidate for studying quantum effects, including isotope effects, in metals. The numerical calculations in Ref. 1 show that the kinetic energy of lithium is still higher than the classical value $\frac{3}{2}T$ even at 520 K. However, since the cohesive energy E_c is substantial, the ratio (1) in the case of lithium is ~ 0.02, signifying that the quantum effects are generally small. In this connection, it is worthwhile to estimate the expected quantum contributions to the pressure P and the bulk modulus K for lithium isotopes. We write the quantum contribution to the pressure at $T=0$ in the quasiharmonic approximation as

$$P_z = \gamma \frac{E_z}{V}, \tag{2}$$

where γ is the Grüneisen constant, E_z is the zero-point energy, and V is the atomic volume. Taking $\gamma=1$ and $E_z=\frac{9}{8}\Theta_D$, we rewrite Eq. (2) as

$$P_z \cong \Theta_D/V. \tag{3}$$

Taking account of the fact that natural lithium consists primarily of the isotope Li^7, and taking $\Theta_D^{Li^7}=344$ K,[2] we have $\Theta_D^{Li^6}\cong 372$ K. For $V=12.7$ cm^3/g·atom we obtain, using relation (3),

$$\Delta P_z = P_z^{Li^6} - P_z^{Li^7} \cong 0.02 \text{ GPa}. \tag{4}$$

Next, from Eq. (3), neglecting the volume dependence of the Grüneisen constant, we have for the quantum contribution to the bulk modulus $K_z=-V(dP_z/dV)$

$$K_z = \gamma(1+\gamma)\frac{\Theta_D}{V}. \tag{5}$$

Substituting into Eq. (5) the numerical values of Θ_D (Ref. 2) and V (Ref. 2), we obtain $\Delta K_z = 0.04$ GPa. These estimates are, of course, order-of-magnitude estimates and pertain to absolute zero.

We shall also estimate the isotopic volume effect, especially since in this case it is possible to make a direct comparison with experimental data.[3] We write the relative volume difference of the corresponding lithium isotopes as

$$\frac{\Delta V}{V} \approx \frac{V^{Li^6}-V^{Li^7}}{V_0} = \frac{\Delta P_z}{K}, \tag{6}$$

where V_0 is the ''classical'' volume of lithium. Taking ΔP_z from Eq. (4) and $K=12$ GPa,[2] we obtain $\Delta V/V = 1.5\times 10^{-3}$. Curiously, the much more complicated calculations performed in Ref. 4, which are based on a calculation of the phonon spectrum of Li, give $\Delta V/V = 1.8\times 10^{-3}$. The corresponding experimental value is $\approx 1.2\times 10^{-3}$ at room temperature.[3]

The estimates presented above show that the problem of determining the isotope effects in the equation of state of lithium is by no means hopeless. As shown in the present letter, the contributions of quantum effects to the equation of state and elastic properties of lithium isotopes are quite distinguishable.

EXPERIMENTAL PART

The equation of state and the elastic properties of polycrystalline lithium were investigated using the ultrasonic piezometer described in Ref. 5. This method was used in previous work to investigate natural lithium up to 1.6 GPa and temperature 77 K.[6] In the present experiment, just as in Ref. 6, the high-pressure unit of the piezometer was immersed in a liquid-nitrogen bath. The temperature of the unit was measured with copper-constantan thermocouples and was 77.4 ± 0.2 K. In the course of the experiment the times Δt and range Δl of ultrasonic pulses were measured as functions of the load F. The measurement errors in these quantities were ~ 0.01 mm and $\sim 0.01\mu$s, respectively. The pressure was calculated from the obvious relation $P=F/S$, where S is the piston area of the piezometer, with corrections for friction and deformation. The accuracy of the pres-

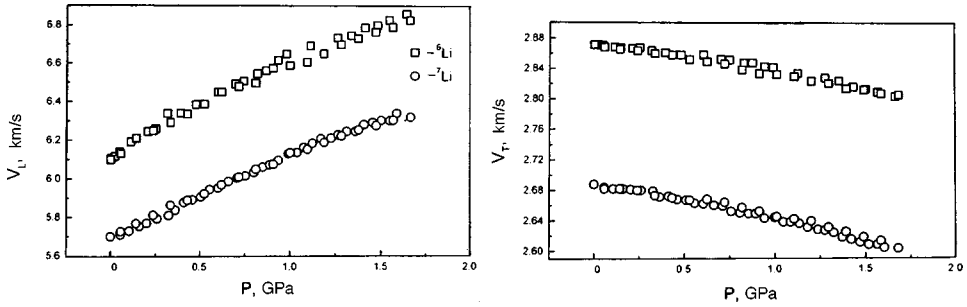

FIG. 1. Longitudinal (V_L) and transverse (V_T) velocities of ultrasonic waves versus pressure P in lithium isotopes at $T=77.4$ K.

sure measurements was better than 0.02 GPa. The velocities of longitudinal (V_l) and transverse (V_t) waves were calculated as functions of the pressure from the $\Delta t(P)$ and $\Delta l(P)$ data obtained (see Refs. 7 and 8 for details).

The investigations were performed on samples of isotopically enriched lithium-6 (Li^6) and samples of lithium with the natural isotopic composition, referred to below as lithium-7 (Li^7). The Li^6 samples contained 99.9% lithium with the isotopic composition 95.83% Li^6 and 4.17% Li^7 together with the impurities Na, Mg, Al, and other elements. The isotopic composition of the 99.87% pure natural lithium (Li^7) was 96.16% Li^7 and 3.84% Li^6; the impurity composition was the same as in the case of the Li^6 samples.

The preparation of samples with adequate isotropy which are suitable for the measurements presented a certain problem because of the high elastic anisotropy of lithium. The best results were obtained by hot deformation followed by rapid quenching of the initial material. As is well known, when metallic lithium, which possesses a body-centered structure under normal conditions, is cooled to liquid-nitrogen temperature, it partially transforms into a rhombohedral 9R phase (structural type Sm).[9–11] It has also been asserted that the low-temperature phase of lithium is most likely a mixture of various polytypes, which are based on close-packed planes of lithium.[12] In any case, when pressure is applied to this structurally nonuniform system, irreversible changes occur, leading ultimately to stabilization of the elastic properties of the system.[6] It is believed that pressure treatment eliminates the residual bcc phase of lithium. It should be noted that the accuracy of the measurements of the velocities of elastic waves in experiments of this type depends strongly on the correctness of the procedures for introducing corrections for friction when calculating the pressure, acoustic anisotropy of the samples, and a number of other factors which are difficult to control. In this situation, the only way to obtain reliable data is to perform repeated independent measurements. At the same time, the variance of the results obtained in independent measurements makes it possible to assess their reliability. In this connection, several series of independent experiments were performed on each of the isotopically enriched samples.

The main experimental result obtained in this work is presented in Fig. 1, which demonstrates the pressure dependence of the longitudinal (V_l) and transverse (V_t) velocities of elastic waves for Li^6 and Li^7. The errors in the measured values of the velocity are of the order of 0.5% for longitudinal and 0.3% for transverse waves. The present data

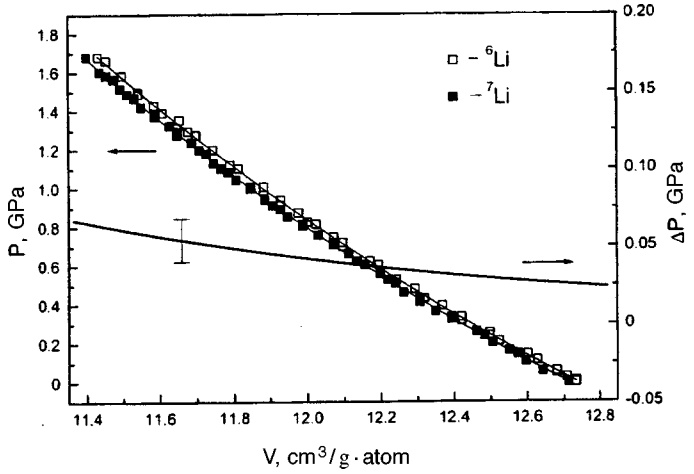

FIG. 2. Pressure P versus volume V in lithium isotopes at $T=77.4$ K. The solid line corresponds to $\Delta P(V)$, where $\Delta P = P^{\mathrm{Li}^6}(V) - P^{\mathrm{Li}^7}(V)$. The vertical bar shows the error in the values of ΔP.

for lithium with the natural isotopic composition (Li^7) agree well with the results of Ref. 6. It is not difficult to calculate from the data obtained the values of the density of Li^6 and Li^7 at high pressures, if the initial values are known.[7,8] The densities at $T=77$ K and atmospheric pressure were taken as $\rho_{\mathrm{Li}^6}=0.474$ g/cm^3 and $\rho_{\mathrm{Li}^7}=0.547$ g/cm^3, respectively. These values were obtained by extrapolating the results of Ref. 3 to low temperatures using the data of Refs. 13 and 14.

Figure 2 shows the pressure versus the atomic volume V for Li^6 and Li^7. The numerical values of V were obtained from the density data with the real isotopic composition taken into account. The function $\Delta P(V) = P^{\mathrm{Li}^6}(V) - P^{\mathrm{Li}^7}(V)$ is also constructed here. The adiabatic and isothermal bulk moduli K_s and K_T and the shear modulus G can be calculated by an elementary method from the data obtained in Refs. 7 and 8. The corresponding results are presented in Figs. 3 and 4. The errors in K_T and G are of the order of 1% and 0.5%, respectively.

DISCUSSION

The anomalous behavior of the transverse sound velocity V_T, which decreases with increasing pressure in both isotopes (Fig. 1), is interesting. In the present case this means that the shear modulus G increases more slowly than the density with increasing pressure ($V_T^2 = G/\rho$) (Fig. 4). This behavior could indicate an approaching instability of the low-temperature phase of Li. The flattening of the curves $G(V)$ at small volumes is an additional argument in favor of this supposition.

Turning to Fig. 2, we note that for low pressures P the pressure difference $\Delta P \simeq 0.025$ GPa, which agrees very well with the estimate made at the beginning of this letter ($\Delta P = 0.02$ GPa). Nonetheless, we recall that the amplitudes of the values of ΔP depend strongly on the initial values used for the density ρ. However, as the calculations show, the character of the behavior of ΔP under compression remains unchanged even if $\Delta\rho$ is chosen from the condition $V_m^{\mathrm{Li}^6} - V_m^{\mathrm{Li}^7} = 0$ at $T=77$ K and atmospheric pressure.

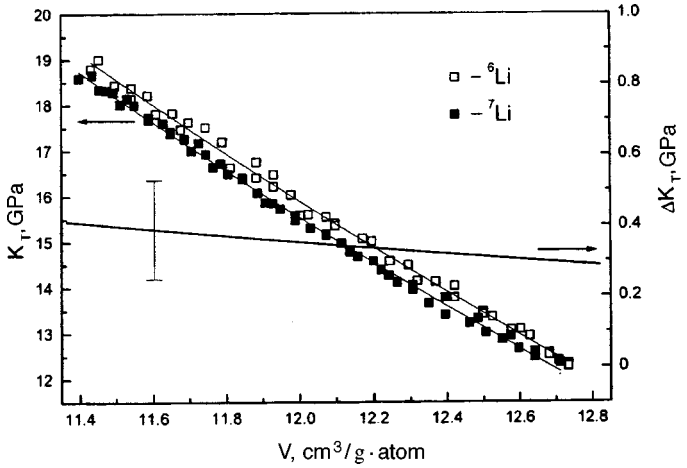

FIG. 3. Bulk modulus K_T versus volume V for lithium isotopes at $T=77.4$ K. Solid line — $\Delta K_T = K_T^{\mathrm{Li}^6}(V) - K_T^{\mathrm{Li}^7}(V)$. The vertical bar shows the error in the values of $\Delta K_T(V)$.

Figure 2 shows clearly that ΔP increases as volume decreases, though it should be remembered that the error in the computed values of ΔP is very substantial.

Figure 3, which shows the volume dependence of the bulk modulus K_T, indicates the reason why ΔP increases under compression. The bulk modulus of the light isotope is everywhere greater than the corresponding modulus of the heavy isotope $K_T^{\mathrm{Li}^6} > K_T^{\mathrm{Li}^7}$. The behavior of $\Delta K_T(V)$ under compression is not entirely clear because of the large error in the computed values of ΔK_T. The experimental values of ΔK_T are several times greater than the estimate made above, though the sign of the estimate is correct. But, in

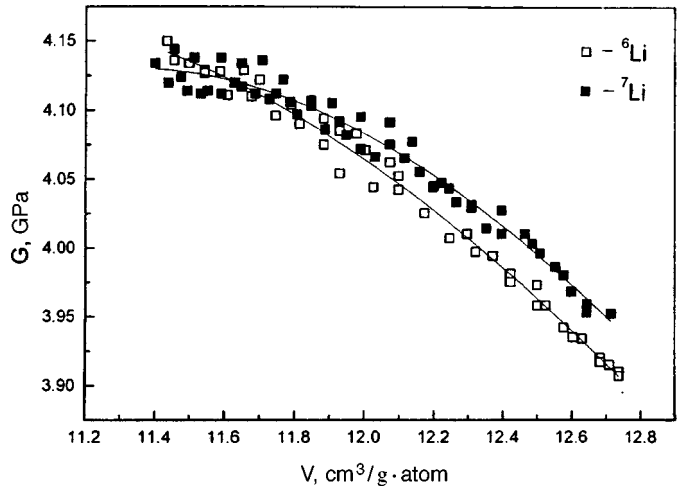

FIG. 4. Shear modulus G versus volume V for lithium isotopes at $T=77.4$ K.

view of the simplifications made, this estimate probably should be regarded as a lower limit.

Finally, we turn once again to Fig. 4. Without discussing, for the time being, the region where the curves $G(V)$ strongly flatten, we call attention to the fact that for large volumes $G^{\mathrm{Li}^7} > G^{\mathrm{Li}^6}$. This result could attest to a large anharmonic contribution to the shear moduli as a result of zero point vibrations, which, generally speaking, is expected. In this case, the actual equality of the shear moduli at small volumes (see Fig. 4) could possibly indicate a decrease in anharmonic effects under compression. However, the data from Ref. 14, where any quantum contribution to the elastic constants of lithium is rejected, are at variance with this supposition. We could explain this assertion with respect to the bulk modulus K_T. The difference between the corresponding values for Li^6 and Li^7 becomes unnoticeable in the coordinates $K_T - P$. However, this explanation does not work for the shear moduli. Thus this question requires further investigation.

In closing, it should be stated that the present experimental data apparently can serve as proof of the existence of quite measurable quantum contributions to the equation of state and elastic properties of lithium at $T = 77$ K. These contributions, at least, do not decrease with pressure, which, strictly, can be expected of a system in which the Coulomb interaction predominates.[15]

[1] C. Filippi and D. M. Ceperley, Phys. Rev. B **57**, 252 (1998).
[2] C. Kittel, *Introduction to Solid State Physics*, 4th ed., Wiley, New York, 1971.
[3] E. J. Covington and D. J. Montgomery, J. Chem. Phys. **27**, 1030, (1957).
[4] B. Johansson and A. Rosengren, J. Phys. **5**, L15 (1975).
[5] O. V. Stal'gorova, E. L. Gromnitskaya, D. R. Dmitriev, and F. F. Voronov, Prib. Tekh. Éksp., No. 6, 115 (1996).
[6] E. L. Gromnitskaya and O. V. Stal'gorova, Zh. Éksp. Teor. Fiz. **106**, 1453 (1994) [JETP **79**, 7785 (1994)].
[7] F. F. Voronov, Fiz. Met. Metalloved. **11**, 620 (1961).
[8] F. F. Voronov and O. V. Stal'gorova, Fiz. Met. Metalloved. **34**, 496 (1972).
[9] C. M. McCarthy, C. W. Tompson, and S. A. Werner, Phys. Rev. B **22**, 574 (1980).
[10] H. G. Smith, Phys. Rev. Lett. **58**, 1228 (1987).
[11] W. Schwarz and O. Blaschko, Phys. Rev. Lett. **65**, 3144 (1990).
[12] W. Schwarz, O. Blaschko, and I. Gorgas, Phys. Rev. B **44**, 6785 (1991).
[13] W. B. Pearson, Can. J. Phys. **32**, 708 (1954).
[14] R. A. Felice, J. Trivisonno, and D. E. Schuele, Phys. Rev. B **16**, 5173 (1977).
[15] I. Pomeranchuk, Zh. Éksp. Teor. Fiz. **20**, 919 (1950).

Translated by M. E. Alferieff

On the NMR spectrum in antiferromagnetic $CsMnI_3$

V. I. Marchenko and A. M. Tikhonov
P. L. Kapitsa Institute of Physics Problems, Russian Academy of Sciences, 117334 Moscow, Russia

(Submitted 1 December 1998)
Pis'ma Zh. Éksp. Teor. Fiz. **69**, No. 1, 41–45 (10 January 1999)

An explanation is proposed for the spin-reduction anisotropy observed in an investigation of NMR in the noncollinear six-sublattice antiferromagnet $CsMnI_3$. © *1999 American Institute of Physics.* [S0021-3640(99)00901-9]

PACS numbers: 75.50.Ee, 33.25.+k

In exchange-interaction magnets, relativistic effects lead to a definite orientation of the spin structure with respect to the crystal axes and to weak distortions of the relative orientation of the sublattices — weak ferromagnetism[1–3] or weak (additional) antiferromagnetism[2] (see the case of Cr_2O_3). In Ref. 4 relativistic distortions of a new type, which the authors termed spin-reduction anisotropy, were found in the noncollinear antiferromagnet $CsMnI_3$. In the present letter, a description of this phenomenon is given on the basis of the theory of exchange symmetry.[5]

The relative orientation of the sublattices in $CsMnI_3$ is shown in Fig. 1. Following Dzyaloshinskiĭ,[2] we introduce instead of the six sublattices their linear combinations

$$\begin{aligned}
&\mathbf{M}=\mathbf{M}_1+\mathbf{M}_2+\mathbf{M}_3+\mathbf{M}_4+\mathbf{M}_5+\mathbf{M}_6,\\
&\mathbf{L}=\mathbf{M}_1+\mathbf{M}_2+\mathbf{M}_3-\mathbf{M}_4-\mathbf{M}_5-\mathbf{M}_6,\\
&\mathbf{L}_1=\mathbf{M}_1-\frac{1}{2}(\mathbf{M}_2+\mathbf{M}_3)-\mathbf{M}_4+\frac{1}{2}(\mathbf{M}_5+\mathbf{M}_6),\\
&\mathbf{L}_2=\frac{\sqrt{3}}{2}(\mathbf{M}_2-\mathbf{M}_3)-\frac{\sqrt{3}}{2}(\mathbf{M}_5-\mathbf{M}_6),\\
&\mathbf{L}_3=\mathbf{M}_1-\frac{1}{2}(\mathbf{M}_2+\mathbf{M}_3)+\mathbf{M}_4-\frac{1}{2}(\mathbf{M}_5+\mathbf{M}_6),\\
&\mathbf{L}_4=\frac{\sqrt{3}}{2}(\mathbf{M}_2-\mathbf{M}_3)+\frac{\sqrt{3}}{2}(\mathbf{M}_5-\mathbf{M}_6),
\end{aligned} \tag{1}$$

which transform according to one-dimensional $\mathbf{M}, \mathbf{L}$ and two-dimensional $(\mathbf{L}_1,\mathbf{L}_2),(\mathbf{L}_3,\mathbf{L}_4)$ representations of the group of permutations of the sublattices realized by the crystal transformations of the symmetry group D_{6h}^4 of the crystal. In the exchange approximation, in $CsMnI_3$ the antiferromagnetism vectors $(\mathbf{L}_1,\mathbf{L}_2)$ are nonzero; in addition, they are equal in modulus and perpendicular to each other, in agreement with the

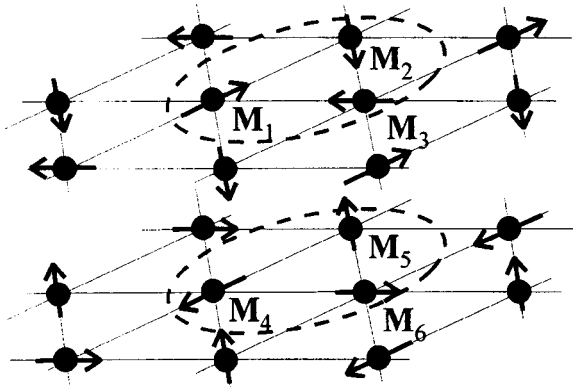

FIG. 1.

general requirements of exchange symmetry.[5] Analysis of the quadratic relativistic invariants shows that the remaining spin vectors do not arise in the structure as an effect due to weak ferromagnetism **M** or weak antiferromagnetism **L**, $(\mathbf{L}_3,\mathbf{L}_4)$. It is found that the distortions of the spin structure that were found in Ref. 4 reduce to breakdown of the exchange condition — the equality of the moduli of the vectors $(\mathbf{L}_1,\mathbf{L}_2)$. This effect arises for the following reasons.

The exchange energy of a structure with arbitrary magnitudes and relative orientation of the spin vectors $\mathbf{L}_1,\mathbf{L}_2$ is a function of the form

$$E\{\mathbf{L}_1^2+\mathbf{L}_2^2,\quad 4(\mathbf{L}_1\cdot\mathbf{L}_2)^2+(\mathbf{L}_1^2-\mathbf{L}_2^2)^2\}. \tag{2}$$

We introduce as the variables characterizing the magnitudes and relative orientation of the vectors $\mathbf{L}_1,\mathbf{L}_2$ the parameters ξ, ζ, and ϕ, defined as

$$L_1=\xi\cos\zeta,\quad L_2=\xi\sin\zeta,\quad \mathbf{L}_1\cdot\mathbf{L}_2=L_1L_2\cos\phi. \tag{3}$$

The minimum of the exchange energy in $CsMnI_3$ corresponds to the value $\xi=\xi_0$ and

$$\zeta=\pi/4,\quad \phi=\pi/2. \tag{4}$$

Near this minimum the exchange energy is a positive-definite quadratic form with respect to small deviations:

$$\text{const}+C_1[4(\delta\zeta)^2+(\delta\phi)^2]+C_2(\delta\xi)^2. \tag{5}$$

The anisotropy energy of first-order in $(v/c)^2$ reduces to the invariant

$$-B(L_{1z}^2+L_{2z}^2)/2. \tag{6}$$

As a result of this term, the vectors $\mathbf{L}_1,\mathbf{L}_2$ will differ from the values $\mathbf{L}_1^0,\mathbf{L}_2^0$ of the exchange approximation (3) and (4) by some amount $\delta\mathbf{L}_1,\delta\mathbf{L}_2$. The term in the anisotropy energy (6) that is linear in these deviations has the form

$$-B(L_{1z}^0\delta L_{1z}+L_{2z}^0\delta L_{2z}). \tag{7}$$

In $CsMnI_3$ in the ground state the spin plane is perpendicular to the basal plane of the crystal (the anisotropy constant B is positive). The orientation of the sublattices in the

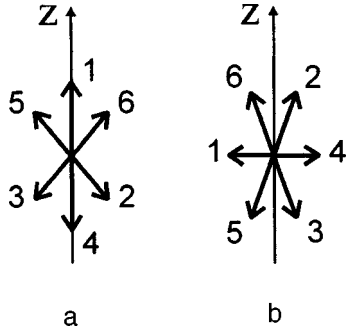

FIG. 2. Distortions of the exchange structure by anisotropy in $CsMnI_3$.

spin plane and the azimuthal orientation of the spin plane itself are fixed by the sixth-order anisotropy energy.[6] In the presence of a magnetic field directed along a symmetry axis of the crystal, the following three orientational states are observed:[7,8] In fields below $H_{c1}=39$ kOe — the phase I ($L_{1z}^0=L_1^0, L_{2z}^0=0$, Fig. 2a); in the interval $H_{c1}<H<H_c=52.5$ kOe — the phase II ($L_{1z}^0=0, L_{2z}^0=L_2^0$, Fig, 2b); and, for $H>H_c$ — the phase III ($L_{1z}^0=L_{2z}^0=0$, Fig. 1).

Minimizing the sum of expressions (5) and (7), we find that in each phase the vectors $(\mathbf{L}_1,\mathbf{L}_2)$ remain orthogonal ($\delta\phi=0$) and that

$$\begin{aligned}
&\text{phase I:} \quad \delta\zeta=-A_1, \quad \delta\xi=A_2\xi_0,\\
&\text{phase II:} \quad \delta\zeta=A_1, \quad \delta\xi=A_2\xi_0,\\
&\text{phase III:} \quad \delta\zeta=0, \quad \delta\xi=0,
\end{aligned} \tag{8}$$

where the constants $A_1=B\xi_0^2/16C_1$ and $A_1=B/4C_2$ are positive.

Therefore the easy-axis anisotropy can lead to $L_1^2\neq L_2^2$ and to an increase in the squared order parameter $L_1^2+L_2^2$. In the general case, evidently, relativistic effects can also destroy the orthogonality of the antiferromagnetism vectors. In $CsMnI_3$ the exchange interaction between the nearest neighbors along the z axis is much greater than exchange in the basal plane.[9] It is easy to show that this leads to $C_2\gg C_1/\xi_0^2$, so that when comparing with experiment we neglect the contribution of A_2.

Inverting the system (1) with respect to the magnetizations of the sublattices with allowance for the uniform magnetization in the external magnetic field, we obtain

$$\mathbf{M}_j=\frac{1}{6}\mathbf{M}+\frac{1}{3}\{\mathbf{L}_1\cos(\mathbf{Q}\cdot\mathbf{r}_j)+\mathbf{L}_2\sin(\mathbf{Q}\cdot\mathbf{r}_j)\}, \quad \mathbf{Q}=\left(\frac{4\pi}{3a},0,\frac{\pi}{c}\right), \tag{9}$$

where a and c are the periods of the crystal lattice. Up to terms linear in the magnetic field, we obtain in the phase I

$$M_1=M_0\left(1+A_1+\frac{H}{H_E'}\right), \quad \cos\alpha_1=1,$$

$$M_{2,3}=M_0\left(1-\frac{1}{2}A_1-\frac{1}{2}\frac{H}{H'_E}\right),\quad \cos\alpha_{2,3}=-\frac{1}{2}-\frac{3}{4}A_1+\frac{3}{4}\frac{H}{H'_E},$$
$$M_4=M_0\left(1+A_1-\frac{H}{H'_E}\right),\quad \cos\alpha_4=-1, \tag{10}$$
$$M_{5,6}=M_0\left(1-\frac{1}{2}A_1+\frac{1}{2}\frac{H}{H'_E}\right),\quad \alpha_{5,6}=\frac{1}{2}+\frac{3}{4}A_1+\frac{3}{4}\frac{H}{H'_E},$$

where $H'_E=M_0(N_A/\chi_\perp)\approx 4\times 10^3$ kOe, N_A is Avogadro's number, $\chi_\perp$ is the magnetic susceptibility in the spin plane; we used the value $\chi_\perp=0.75\times 10^{-2}$ cgs units/mole from Ref. 9; α_j is the angle between the magnetization of the jth sublattice and the z axis. In the phase II

$$M_{1,4}=M_0(1-A_1),\qquad \cos\alpha_{1,4}=\frac{H}{H'_E}$$
$$M_{2,6}=M_0\left(1+\frac{1}{2}A_1+\frac{\sqrt{3}}{2}\frac{H}{H'_E}\right),\quad \cos\alpha_{2,6}=\frac{\sqrt{3}}{2}+\frac{\sqrt{3}}{4}A_1+\frac{1}{4}\frac{H}{H'_E},$$
$$M_{3,5}=M_0\left(1+\frac{1}{2}A_1-\frac{\sqrt{3}}{2}\frac{H}{H'_E}\right),\quad \cos\alpha_{3,5}=-\frac{\sqrt{3}}{2}-\frac{\sqrt{3}}{4}A_1+\frac{1}{4}\frac{H}{H'_E}. \tag{11}$$

The structural distortions under discussion are shown schematically in Fig. 2. In phase III the magnetizations of all sublattices are M_0, and $\cos\alpha_j=H/H_E$, where $H_E=M_0(N_A/\chi_\parallel)^2\approx 2\times 10^3$ kOe and $\chi_\parallel$ is the electronic magnetic susceptibility along the normal **n** to the spin plane.

Neglecting relaxation, the dynamics of the nuclear sublattice reduces[10,11] to the dynamics of a ferromagnet in an effective field. Therefore the Lagrangian of the low-frequency spin dynamics of the antiferromagnet $CsMnI_3$ will be the sum of the Lagrangian of a noncollinear antiferromagnet[5] and six Lagrangians of the nuclear sublattices coupled by the hyperfine interaction:

$$\frac{\chi_\perp}{2\gamma^2}(\mathbf{\Omega}+\gamma\mathbf{H})^2+\frac{\chi_\parallel-\chi_\perp}{2\gamma^2}(\mathbf{n}\cdot(\mathbf{\Omega}+\gamma\mathbf{H}))^2-\mathcal{U}_a+\frac{1}{6}\sum_{j=1}^{6}\mathbf{m}_j\cdot\left(\frac{\mathbf{\Omega}_{nj}}{\gamma_n}-A\mathbf{M}_j+\mathbf{H}\right), \tag{12}$$

where $\mathbf{\Omega}$ is the angular velocity of the electronic spin rotations; $\mathbf{\Omega}_{nj}$ is the angular velocity of the spin rotations of the nuclei in the jth sublattice; χ_n is the susceptibility of the nuclei; γ and γ_n are the electronic and nuclear gyromagnetic ratios; A is the hyperfine interaction constant; $\mathbf{m}_j$ is the magnetization of the jth nuclear sublattice, and its equilibrium value is $\chi_n(-A\mathbf{M}_j+\mathbf{H})$.

When the spin plane is normal to the basal plane of the crystal, the energy $\mathcal{U}_a$ reduces to the expression $f(H)\cos 6\varphi$, $f(H)=b_1+b_3H^2+b_4H^4+b_5H^6$, where φ is the angle between the vector $\mathbf{L}_1$ and the z axis. Since the function $f(H)$ changes sign in the field H_{c1},[8] it is convenient to introduce a different representation

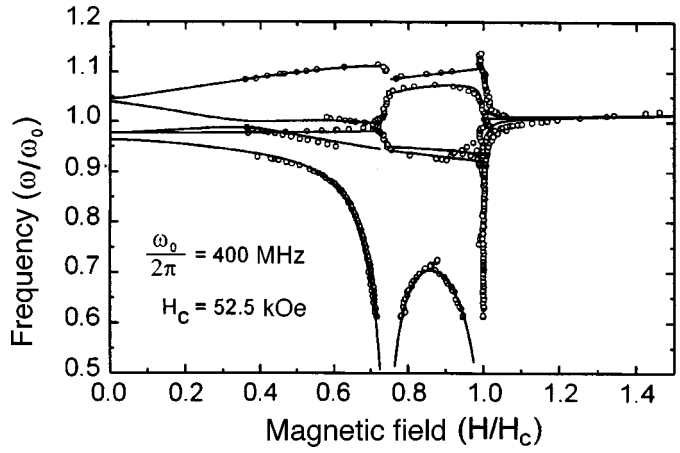

FIG. 3. NMR spectrum in $CsMnI_3$. The experimental data are taken from Ref. 7 at temperature 1.3 K.

$$f(H)=b_1\left[1-\left(\frac{H}{H_{c1}}\right)^2\right]\left[1+k_1\left(\frac{H}{H_c}\right)^2+k_2\left(\frac{H}{H_c}\right)^4\right]. \tag{13}$$

This function determines the field dependence of the AFMR frequency associated with oscillations of the angle φ. The constants b_1 (associated with the zero-field frequency) and $k_1=-1.7$ can be determined from the experimental data of Ref. 6; the contribution of the term $\propto k_2$ is small in the frequency range investigated in Ref. 6. The constant A_1 determines the zero-field splitting of the NMR frequencies:

$$\frac{\omega_1-\omega_2}{\omega_1}=\frac{M_1-M_2}{M_1}\approx\frac{3}{2}A_1. \tag{14}$$

According to the experimental data of Ref. 4, $\omega_1/2\pi=417$ MHz and $\omega_2/2\pi=390$ MHz, whence $A_1=0.045$.

The magnetic resonance spectrum described by the Lagrangian (12) consists of three AFMR branches (see Refs. 6 and 10) and six NMR branches. Five NMR branches for the values taken above for the parameters of the theory and for the two remaining adjustable parameters $\gamma_n AM_0/2\pi=\omega_0/2\pi=400$ MHz and $k_2=0.71$ are presented in Fig. 3. The frequency of the sixth branch neglecting in-plane anisotropy is zero.

We note that the function $f(H)$ for the indicated values of the parameters k_1 and k_2 vanishes in a field slightly above H_c, i.e., the system is accidentally close to a spin-flop transition from the phase II to the phase I as H_c is approached.

This work was partially supported by Grant No. 98-02-16572 from the Russian Fund for Fundamental Research.

[1] A. S. Borovik-Romanov and M. P. Orlova, Zh. Éksp. Teor. Fiz. **31**, 579 (1956) [Sov. Phys. JETP **4**, 531 (1957)].
[2] I. E. Dzyaloshinksiĭ, Zh. Éksp. Teor. Fiz. **32**, 1547 (1957) [Sov. Phys. JETP **5**, 1259 (1957)].
[3] A. S. Borovik-Romanov, Zh. Éksp. Teor. Fiz. **36**, 766 (1959) [Sov. Phys. JETP **9**, 539 (1959)].
[4] B. S. Dumesh, S. V. Petrov, and A. M. Tikhonov, JETP Lett. **67**, 692 (1998).
[5] A. F. Andreev and V. I. Marchenko, Usp. Fiz. Nauk **130**, 39 (1980) [Sov. Phys. Usp. **23**, 21 (1980)].

[6] S. I. Abarzhi, M. E. Zhitomirskiĭ, O. A. Petrenko *et al.*, Zh. Éksp. Teor. Fiz. **104**, 3232 (1993) [JETP **77**, 521 (1993)].
[7] B. S. Dumesh, S. V. Petrov, and A. M. Tikhonov, JETP Lett. **67**, 1046 (1998).
[8] V. I. Marchenko and A. M. Tikhonov, Pis'ma Zh. Éksp. Teor. Fiz. **68**, 844 (1998) [JETP Lett. **68**, 887 (1998)].
[9] H. W. Zandbergen, J. Solid State Chem. **35**, 367 (1980).
[10] L. A. Prozorova, S. S. Sosin, D. V. Efremov, and S. V. Petrov, Zh. Éksp. Teor. Fiz. **112**, 1893 (1997) [JETP **85**, 1035 (1997)].
[11] A. S. Borovik-Romanov, B. S. Dumesh, S. V. Petrov, and A. M. Tikhonov, Zh. Éksp. Teor. Fiz. **113**, 352 (1998) [JETP **86**, 197 (1998)].

Translated by M. E. Alferieff

Changes in the magnetic structure of $(La_{0.25}Pr_{0.75})_{0.7}Ca_{0.3}MnO_3$ upon the isotopic substitution of ^{18}O for ^{16}O

A. M. Balagurov, V. Yu. Pomyakushin, D. V. Sheptyakov, and V. L. Aksenov
Neutron Physics Laboratory, Joint Institute of Nuclear Research, 141980 Dubna, Russia

N. A. Babushkina, A. M. Belova, A. N. Taldenkov, and A. V. Inyushkin
Kurchatov Institute Russian Science Center, 123182 Moscow, Russia

P. Fischer, M. Gutmann, and L. Keller
Paul Scherrer Institute, CH-5232 Villigen, Switzerland

O. Yu. Gorbenko, V. A. Amelichev, and A. R. Kaul'
Moscow State University, 119899 Moscow, Russia

(Submitted 2 December 1998)
Pis'ma Zh. Éksp. Teor. Fiz. **69**, No. 1, 46–51 (10 January 1999)

A giant isotope effect, wherein the low-temperature metallic state is replaced by an insulator state, was recently observed when ^{18}O was substituted for ^{16}O in $(La_{0.25}Pr_{0.75})_{0.7}Ca_{0.3}MnO_3$ [N. A. Babushkina, L. M. Belova, O. Yu. Gorbenko *et al.*, Nature (London) **391**, 159 (1998)]. In the present work, the temperature evolution of the magnetic structure of two samples of this compound is studied by neutron diffraction. One sample contained a natural mixture of oxygen isotopes, 99.7% ^{16}O, while the other was enriched to 75% with the isotope ^{18}O. It is established that the samples are crystallographically identical at room temperature. As the temperature decreases, the sample with ^{16}O undergoes successive antiferromagnetic ($T_{AFM}=150$ K) and ferromagnetic ($T_{FM}=110$ K) transitions, which lead to the establishment of a noncollinear ferromagnetic structure, while a purely antiferromagnetic ($T_{AFM}=150$ K) order arises in the sample with ^{18}O. The temperature dependences of the intensities of the diffraction peaks associated with the charge ordering differ substantially in samples with ^{16}O and ^{18}O, and they correlate with the behavior of their electric resistance and magnetic structure.
[S0021-3640(99)01001-4]

PACS numbers: 75.30.Kz, 75.50.−y, 71.30.+h

Investigations performed in the last few years have shown that the low-temperature state of manganites with the perovskite structure $A_{1-x}A'_xMn^{3+}_{1-x}Mn^{4+}_xO_3$, where A is La or a rare-earth ion and A′ is an alkaline-earth divalent cation — Ca, Sr, etc., is determined by the balance of several types of interactions and can be easily modified by

changing the composition or by an external perturbation (see, for example, the review articles of Refs. 1 and 2 and also Ref. 3). The phase transition from the paramagnetic insulator into the ferromagnetic metallic state (insulator–metal transition) is ordinarily described in the the ''double exchange'' model,[4] on the basis of which the possible magnetic configurations have been predicted and the correlation between the magnetic and transport properties has been interpreted.[5,6]

The observed features of phase transitions in perovskite manganites (now widely known as CMR compounds on account of the ''colossal'' magnetoresistance effect observed in them[7]) cannot be explained solely on the basis of the double-exchange model and they make it necessary to take account of additional effects (the dynamic and static Jahn–Teller effects, ordering of the charges Mn^{3+} and Mn^{4+} in the structure, and others), and special experiments are must be performed in order to clarify the role of these effects.

The investigation of the coupling of the electronic and phonon subsystems in manganites merits special attention. A great deal of evidence showing the importance of this interaction is presented in a recent review.[8] Isotopic substitution is a direct experimental method for studying the effect of the dynamics of atomic vibrations on physical properties.[9–11] For example, in the first work on this subject[9] it was found for the compound $La_{0.8}Ca_{0.2}MnO_3$ that the Curie temperature decreases by 21 K upon 95% substitution of ^{18}O for ^{16}O. This is much greater than the shift of the temperature of magnetic or electronic phase transitions in other previously investigated oxides, e.g., high-temperature superconductors. In Ref. 11 the effect of isotopic substitution was investigated for the compound $(La_{1-y}Pr_y)_{0.7}Ca_{0.3}MnO_3$ with $y=0.75$; this choice is based on the critical value of the tolerance factor of the perovskite structure for this composition (~ 0.91), at which the structure becomes especially sensitive to various physical perturbations. In Ref. 11 it was observed that this composition with the natural isotopic oxygen content (99.7% ^{16}O, referred to in the text below as O-16) becomes a metal at $T \approx 100$ K, while for the composition 85% enriched in the isotope ^{18}O (referred to below as O–18) the effect is not simply a decrease of the temperature of the transition to the metallic state but rather the circumstance that the compound remains an insulator right down to 4 K (Fig. 1). A similar effect has also been observed[12] in the compound $(La_{0.5}Nd_{0.5})_{0.67}Ca_{0.33}MnO_3$.

In the present work we investigared how the magnetic structure is affected by the isotopic substitution of ^{18}O for ^{16}O in $(La_{1-y}Pr_y)_{0.7}Ca_{0.3}MnO_3$ with $y=0.75$. Just as in a previous work[13] for the composition with $y=0.5$, we employed neutron diffraction to identify the magnetic structure and to determine the changes occurring in the atomic structure together with the colossal isotope effect.

The samples were prepared in the powder form by means of the so-called ''paper synthesis.'' For this, a water solution of a mixture of nitrates of La, Pr, Ca, and Mn, taken in the required ratios, was deposited on ash-free paper filters, which after drying (120 °C) were burned. The oxide product obtained in the process was roasted at 700 °C in air for 2 h. The final heat treatment was performed by annealing compressed tablets at 1200 °C in air for 12 h.

The process of enriching the composition $(La_{0.25}Pr_{0.75})_{0.7}Ca_{0.3}MnO_3$ with oxygen isotopes was conducted at $T=950$ °C and $p=1$ atm. Two samples, each of mass 5 g,

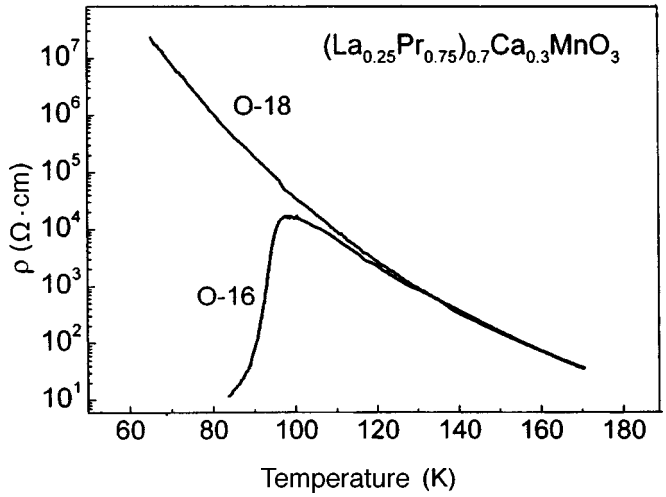

FIG. 1. Temperature dependence of the resistance of the compound $(La_{0.25}Pr_{0.75})_{0.7}Ca_{0.3}MnO_3$ for the samples O-16 and O-18 near the phase transition of the sample O-16 to the metallic state ($T_{IM} \approx 100$ K). The resistance of the sample O-18 has a semiconductor dependence right down to liquid-helium temperature.

were annealed simultaneously: one sample in an ^{16}O atmosphere (99.7% enrichment) and the other in an ^{18}O atmosphere (85% enrichment). Platinum crucibles holding the powders were placed inside two quartz tubes arranged parallel in a furnace. Each tube was a part of a closed loop. ^{16}O oxygen circulated in one loop, and ^{18}O oxygen circulated in the other. Eleven successive changes of the oxygen atmosphere were made in the loop. The oxygen gas depleted as a result of exchange was removed from the loop and the loop was filled with ''fresh'' ^{18}O oxygen with 85% isotopic enrichment. The total annealing time at 950 °C was 100 h. The ^{18}O content in the sample obtained was 75%, as followed from the change in weight of the sample and the results of mass-spectrometric analysis of the oxygen atmosphere in the loop.

Neutron-diffraction experiments were performed on a DMC diffractometer at the Paul Scherrer Institute using the SINQ source. The diffraction spectra were measured in a regime with the sample heated from 12 to 293 K. The samples were packed in a hermetically sealed vanadium container (8 mm in diameter and 40 mm high) filled with helium. The magnetic structure was analyzed according to the diffraction spectra measured at wavelength $\lambda = 2.5616$ Å . Rietveld refinement (FULLPROF program, space group *Pnma*) was performed in the range of scattering angles $2\theta = 10–90°$, corresponding to d_{hkl} from 1.8 to 14.7 Å .

It is obvious that a necessary condition for making a correct comparison of the results obtained for isotopically-substituted samples is that the samples must be crystallographically identical. Analysis of the room-temperature diffraction spectra showed that the O-16 and O-18 samples are indeed identical; specifically, their oxygen contents were identical to within ± 0.03. A comparison of the unit cell parameters of the two samples gives better accuracy. Their measurement, performed at room temperature in the FDVR high-resolution neutron diffractometer in Dubna, gave the following results:

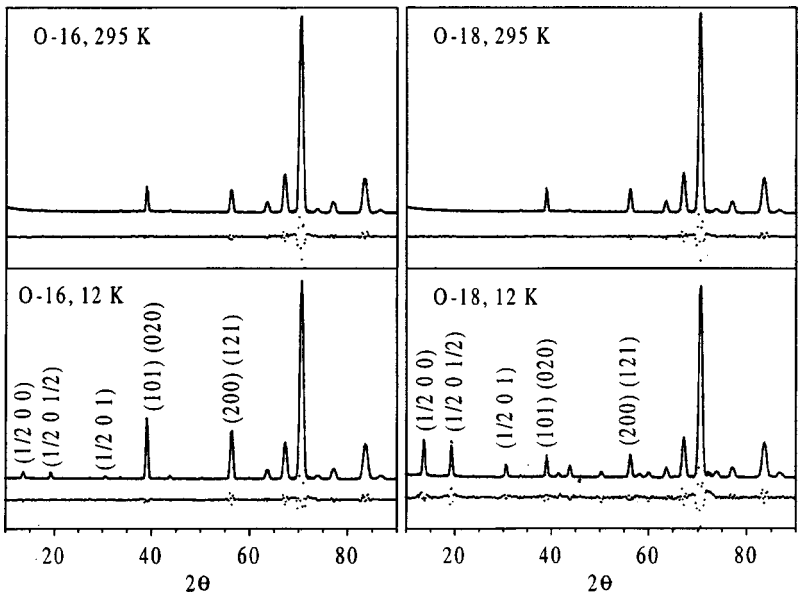

FIG. 2. Diffraction spectra of the O-16 and O-18 samples measured at room temperature (top figures) and at $T=12$ K (bottom figures). The spectra are identical at room temperature. At low temperature the intensity of the AFM peaks (1/2 0 0) and (1/2 0 1/2) for sample O-18 is much higher, while in the spectrum of the O-16 sample the intensity of the FM peaks (101)/(020) and (200)/(121) is higher. The bottom curves in the figures show the difference of the measured and computed (by the Rietveld method) intensities and demonstrate the good agreement.

$a=5.45657(7)$ Å, $b=7.69294(9)$ Å, $c=5.44788(8)$ Å for O-16 and $a=5.45673(6)$ Å, $b=7.69315(8)$ Å, $c=5.44786(7)$ Å for O-18, i.e., the unit cell parameters are identical to within 0.002–0.004%. A comparison with existing dependences of the cell parameters of manganites on the amount of oxygen (see, for example, Ref. 14) gives in this case an upper limit ± 0.002 for the difference in the oxygen content between the O-16 and O-18 samples. The data from chemical analysis of the samples O-16 and O-18 by the iodometry method, described in Ref. 15, agree with this estimate: The oxygen content in the general formula $(La_{0.25}Pr_{0.75})_{0.7}Ca_{0.3}MnO_x$ corresponds to $x=2.995\pm 0.008$ in O-16 and to $x=2.996\pm 0.005$ in O-18.

Figure 2 shows the characteristic neutron diffraction patterns measured for the O-16 and O-18 samples at room temperature and $T=12$ K. One can see that superstructural reflections of the type (1/2 0 0) and (1/2 0 1/2) at $2\theta=13.6°$ and 19.2°, associated with the establishment of antiferromagnetic (AFM) order, appear in the neutron diffraction patterns of both samples as temperature decreases. The intensity of these peaks is much higher for the sample O-18. An enhanced contribution to the nuclear Bragg peaks of the type (101)/(020) and (200)/(121) at $2\theta=39°$ and 56° is clearly noticeable in the neutron diffraction pattern from O-16 at $T=12$ K; this contribution arises with the establishment of ferromagnetic (FM) order. The temperature-dependences of the intensities of the AFM and FM peaks in both samples are shown in Fig. 3. For O-18 the intensity of the AFM peaks grows monotonically with decreasing temperature, and for O-16 the dependence is nonmonotonic and has a maximum at $T\approx 110$ K, which correlates with the appearance of

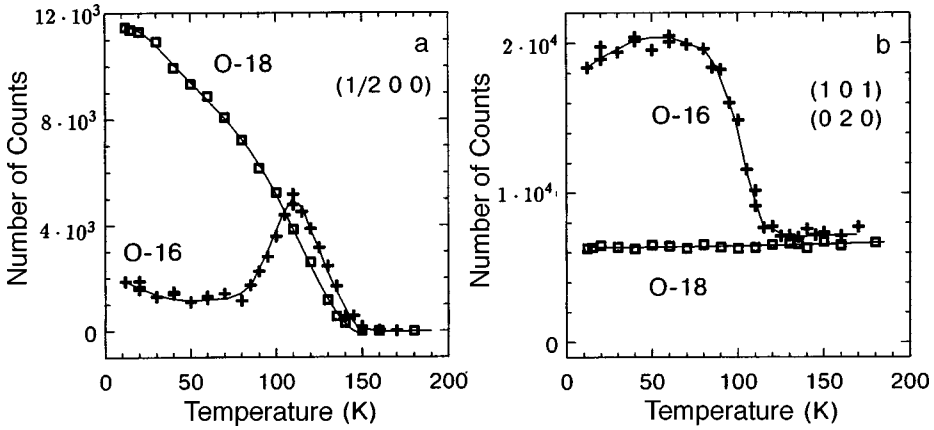

FIG. 3. Temperature dependences of the intensities of the characteristic diffraction peaks of samples O-16 and O-18: (a) AFM peak (1/2 0 0), (b) FM peaks (101)/(020). The decrease at $T<50$ K of the intensity of the (101)/(020) peaks of sample O-16 is due to ordering of the magnetic moments of Pr. The lines are drawn for clarity.

the FM component in the corresponding Bragg peaks. The intensity of the (101)/(020) peaks for the sample O-16 (Fig. 3b) below 50 K decreases somewhat. This can be interpreted by analogy with Ref. 16 as being due to ordering of the magnetic moments of the Pr atoms. For the O-18 sample, to within the statistical accuracy achieved ($\sim$1.3%), there was no FM contribution to the diffraction peaks.

The magnetic structure of the sample O-16 was refined in a model consisting of two antiferromagnetic phases AFM1 and AFM2 and a ferromagnetic phase FM1 with magnetic moments on the Mn atoms. The AFM1 phase was described in a crystal cell with a doubled parameter a and propagation vector $\mathbf{k}_1=(1/2\,0\,0)$; the phase AFM2 was described in a cell with doubled parameters a and c and propagation vector $\mathbf{k}_2=(1/2\,0\,1/2)$. For the sample O-18, the magnetic structure was refined in a similar manner but with no FM component. The values of the magnetic moments of Mn are essentially independent of their orientation. A search through the variants with different directions of the moments along the basal directions yielded the best agreement between the measured and computed intensities with the Mn moments oriented along the b axis in the AFM phases and along the c axis in the FM phase. Figure 4 shows the temperature dependences of the refined magnetic moments μ_{AFM1}, μ_{AFM2}, and μ_{FM}. The magnetic structure formed in the O-16 sample can be represented as noncollinear (canted) ferromagnetic, similar to the structure observed for the compositions $Pr_{0.7}Ca_{0.3}MnO_3$ (Ref. 3) and $Pr_{0.65}(Ca_{0.7}Sr_{0.3})_{0.35}MnO_3$ (Ref. 17). In the sample O-18, not only was the electric conductivity suppressed, but the ferromagnetic component was also completely suppressed, which has not been observed thus far in compositions with Pr with the natural content of oxygen isotopes. Therefore isotopic substitution did not reduce to a simple shift of $T_c(\langle r_{\mathrm{A}}\rangle)$ in the magnetic phase diagram, but rather it led to a fundamentally new magnetic state.

In both samples AFM ordering ($T_{\mathrm{AFM}}\approx 150$ K) is preceded by the appearance of weak superstructural reflections of the type (3/2 0 2) at $T_{\mathrm{CO}}\approx 180$ K (Fig. 5). The ap-

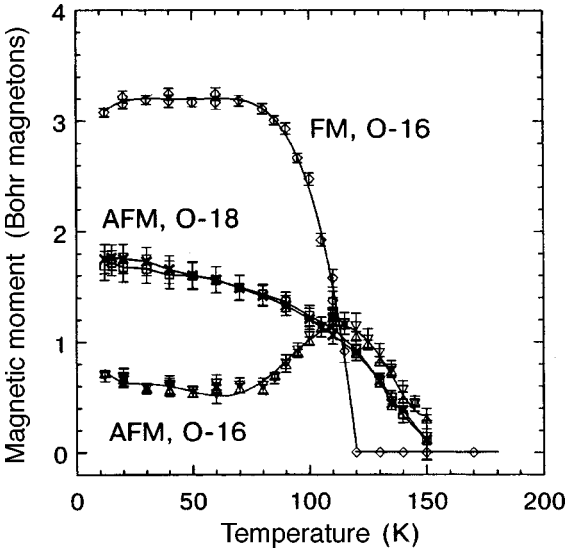

FIG. 4. Temperature dependences of the magnetic moments of Mn (in Bohr magnetons) for the FM and AFM components of the sample O-16 and the AFM components of the sample O-18. For sample O-16 the points at some temperatures were measured twice. In both samples the AFM moments for sublattices with different propagation vectors are virtually identical. The lines are drawn for clarity.

pearance of such reflections is attributed to charge ordering (CO ordering) of the cations Mn^{3+}/Mn^{4+}, which results in doubling of the lattice period along *a* and lowering of the spatial symmetry to the monoclinic $P2_1/m$ structure,[18] which has been well studied[3,19] for the composition $Pr_{0.7}Ca_{0.3}MnO_3$.

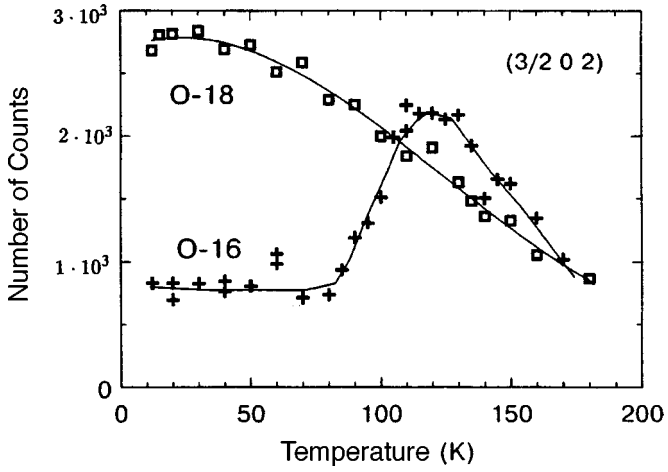

FIG. 5. Temperature dependences of the intensity of the CO peak (3/2 0 2) of samples O-16 and O-18. This peak does not occur at room temperature. For the O-16 sample the points at some temperatures were measured twice. The lines are drawn for clarity.

The experimental results presented show that for $T > T_{CO}$ the O-16 and O-18 samples are crystallographically identical and similar to other CMR compounds with the same ratio of the cations Mn^{3+} and Mn^{4+}. Below $T = T_{CO} \approx 180$ K a charge ordering process commences in both samples. At $T = T_{AFM} \approx 150$ K antiferromagnetic ordering of the magnetic moments of manganese commences, forming a structure with two propagation vectors $\mathbf{k}_1 = (1/2\ 0\ 0)$ and $\mathbf{k}_2 = (1/2\ 0\ 1/2)$ (pseudo-CE-structure[3]). Thus, down to 110 K the CO and AFM ordering processes develop identically in both samples. Below $T = T_{FM} \approx 110$ K a ferromagnetic ordering of manganese moments appears in the O-16 sample. It should be noted especially that the isotopic substitution of oxygen did not change T_{CO} and T_{AFM}.

In Ref. 20 it is shown that the composition $(La_{1-y}Pr_y)_{0.7}Ca_{0.3}MnO_3$ with $y = 0.75$ lies near the boundary between the metallic and insulator states, and even a relatively weak perturbation, including isotopic substitution of oxygen,[11] can transform one state into another. A possible microscopic model of such a transition, in which the electron hopping integral between the states of neighboring ions is related with the reduced mass of the ions, is presented in Ref. 20. In the present work, the magnetic structure of the compound $(La_{0.25}Pr_{0.75})_{0.7}Ca_{0.3}MnO_3$ was determined and it was shown that under isotopic substitution of ^{18}O for ^{16}O the change in the electronic state (metal–insulator) correlates completely with the changes in the magnetic structure (noncollinear ferromagnet – pure antiferromagnet) and with the process of charge ordering of the cations Mn^{3+} and Mn^{4+}.

This work was supported by grants from the Russian Fund for Fundamental Research (Projects 96-02-17823, 97-02-16665, 96-15-96738, and 97-03-32979) and INTAS-RFBR (Projects I-96-0639 and IR-97-1954).

[1] C. N. R. Rao, A. K. Cheetham, and R. Mahesh, Chem. Mater. **8**, 2421 (1996).
[2] A. P. Ramirez, J. Phys.: Condens. Matter **9**, 8171 (1997).
[3] D. Cox, P. G. Radaeli, M. Marezio, and S.-W. Cheong, Phys. Rev. B **57**, 3305 (1998).
[4] C. Zener, Phys. Rev. **82**, 403 (1951).
[5] J. B. Goodenough, Phys. Rev. **100**, 564 (1955).
[6] Z. Jirak, S. Krupicka, Z. Simsa *et al.*, J. Magn. Magn. Mater. **53**, 153 (1985).
[7] S. Jin, M. McCormac, T. H. Tiefel *et al.*, J. Appl. Phys. **76**, 6929 (1994).
[8] A. J. Millis, Nature (London) **392**, 147 (1998).
[9] G. M. Zhao, K. Conder, H. Keller, and K. A. Muller, Nature (London) **381**, 676 (1996).
[10] J. P. Frank, I. Isaac, W. Chen *et al.*, Phys. Rev. B **58**, 5189 (1998).
[11] N. A. Babushkina, L. M. Belova, O. Yu. Gorbenko *et al.*, Nature (London) **391**, 159 (1998).
[12] G. M. Zhao, H. Keller, J. Hofer *et al.*, Solid State Commun. **104**, 57 (1997).
[13] A. M. Balagurov, V. Yu. Pomyakushin, V. L. Aksenov *et al.*, JETP Lett. **67**, 705 (1998).
[14] C. Ritter, M. R. Ibarra, J. M. De Teresa *et al.*, Phys. Rev. B **56**, 8902 (1997).
[15] I. G. Krogh Andersen, E. Krogh Andersen *et al.*, J. Solid State Chem. **113**, 320 (1994).
[16] Z. Jirak, S. Vratislav, and J. Zajicek, Phys. Solid State **52**, K39 (1979).
[17] H. Yoshizawa, R. Kajimoto, H. Kawano *et al.*, Phys. Rev. B **55**, 2729 (1997).
[18] P. G. Radaelli, D. E. Cox, M. Marezio, and S.-W. Cheong, Phys. Rev. B **55**, 3015 (1997).
[19] H. Yoshizawa, H. Kawano, Y. Tomioka, and Y. Tokura, Phys. Rev. B **52**, R13145 (1995).
[20] N. A. Babushkina, L. M. Belova, V. I. Ozhogin *et al.*, J. Appl. Phys. **83**, 7369 (1998).

Translated by M. E. Alferieff

Magnetic states of the surface and bulk of ferrites near a phase transition at the Curie temperature

A. S. Kamzin* and V. L. Rozenbaum
A. F. Ioffe Physicotechnical Institute, Russian Academy of Sciences, 194021 St. Petersburg, Russia

(Submitted 16 October 1998; resubmitted 2 December 1998)
Pis'ma Zh. Éksp. Teor. Fiz. **69**, No. 1, 52–57 (10 January 1999)

Investigations of the magnetic state of a surface layer ~200 nm thick and of the bulk in macroscopic ferrite crystals of the type Ba–M ($BaFe_{12}O_{19}$) are performed in the phase transition region around the Curie temperature (T_c). The method of simultaneous gamma, x-ray, and electron Mössbauer spectroscopy, which made it possible to compare directly the phase states of the surface and bulk of the sample, is used for the measurements. It is observed experimentally that in $BaFe_{12}O_{19}$ the transition of a surface layer ~200 nm thick to the paramagnetic state occurs at temperatures below T_c. It is established that the transition temperature $T_c(L)$ of a thin layer localized at depth L from the surface of the crystal increases with distance from the surface and reaches the value T_c at the lower boundary of the ''critical'' surface layer. Therefore, near T_c a nonuniform state in which the crystal is magnetically ordered in the bulk but disordered at the surface is observed. A phase diagram of the states of the surface and of the bulk of macroscopic magnets near the Curie (or Néel) point is proposed on the basis of all the experimental results obtained in the present work as well as previously published results. © *1999 American Institute of Physics.* [S0021-3640(99)01101-9]

PACS numbers: 75.50.Bb, 75.30.Kz, 75.40.−s

The study of the influence of a ''defect'' such as a surface on the magnetic properties of surface and subsurface layers of a crystal has been increasingly attracting investigators since the 1970s. From the applied standpoint the problem of a surface is of interest because a surface strongly influences the formation of the properties of nanosize powders and films, and an understanding of the nature of the formation of the properties of such materials will make it possible, for example, to determine ways to produce such materials with the required properties.

Surface processes which accompany fundamental phenomena such as phase transitions in the bulk of a crystal are of special interest. The concept of the surface magnetic energy was introduced in the first theoretical descriptions of the surface properties of crystals,[1] and it was shown that for negative values of this energy the surface of a crystal can possess magnetization at temperatures above the Curie point for the bulk of the

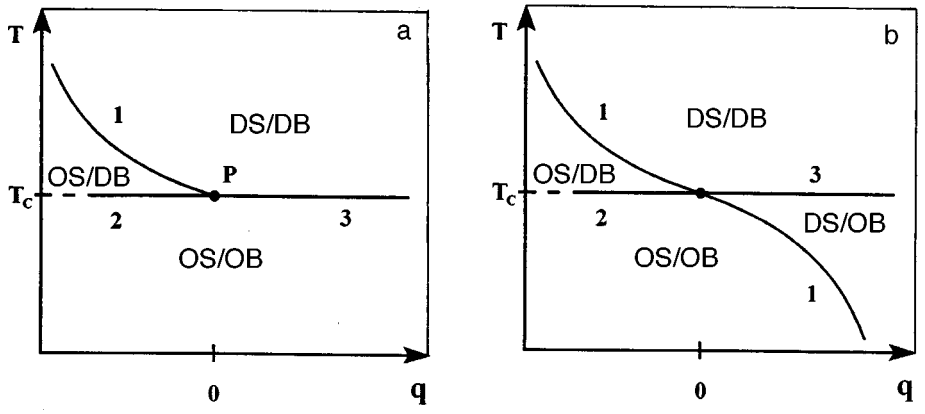

FIG. 1. Phase diagram of states of the surface and bulk of a semi-infinite ferromagnet near the Curie temperature: a — obtained theoretically,[5] b — proposed by the authors on the basis of all experimental data. *1* — Line of surface phase transitions, *2* — ordinary transition, *3* — extraordinary transition. *OB* region — magnetically ordered bulk of the crystal, *OS* — magnetically ordered surface of the crystal, *DB* — magnetically disordered bulk, *DS* — magnetically disordered surface.

sample. The surface magnetization decreases exponentially in a direction into the bulk of the sample. Theoretical investigations of the surface of antiferromagnetic crystals[2] predicted the possibility of the existence of surface magnetization at temperatures above the Néel point. Later, the surface properties were described using virtually all of the methods developed for studying the properties of bulk crystals (see, for example, the reviews Refs. 3–5 and the references cited therein). As a result, a theoretical phase diagram of the states of a surface and of the bulk of a semibounded magnet near the Curie point was obtained. This diagram, taken from Ref. 5, is presented in Fig. 1a, where q is a phenomenological order parameter which was introduced in Ref. 1 and determines the surface energy. The designations of the phase transition lines are as follows:[6] *1* — surface, *2* — ordinary, and *3* — extraordinary. For a negative value of q (see Fig. 1) magnetic ordering arises on the crystal surface up to the appearance of magnetization in the bulk, i.e., at temperatures above the Curie (or Néel) point. For positive q, as follows from theoretical descriptions and the phase diagram (Fig. 1a), the surface just as the bulk of the crystal transform into the paramagnetic state at the Curie (or Néel) temperature.

Results confirming the existence of magnetization on Cr, Co, Ni, Tb, and Gd surfaces at temperatures above the magnetic ordering point in the bulk of these substances have now been obtained experimentally (see Refs. 3–5 and 7 and the references cited therein). Thus, these experimental data agree with the region of the theoretical phase diagram that corresponds to negative values of the parameter q.

Comparatively recently, it was established experimentally that in antiferromagnets with a weak ferromagnetic moment[8,9] as well as in hexagonal ferrites[10] a transition of the surface to the paramagnetic state occurs at temperatures below the Néel (Curie) point for the bulk of the crystals. It has also been shown[8–10] that the temperature of the order–disorder transition decreases continuously within a surface layer of ''critical'' thickness. These experimental data do not agree with the theoretical descriptions of surface magnetism[1–5] and the theoretical phase diagram (Fig. 1a), whence it follows that the

surface of a magnet at temperatures below the Curie point can be only in an ordered state.

In the present letter we present experimental data obtained near a phase transition at the Curie point of the magnetic state of a surface and the bulk of macroscopic crystals with an uncompensated magnetic moment. Ferrite single crystals of the type Ba-M (chemical formula $BaFe_{12}O_{19}$) were chosen for the investigations. Ferrites of the type Ba-M possess the hexagonal crystal structure of magnetoplumbite. At temperatures below the Curie point the magnetic structure of Ba-M crystals is a collinear ferrimagnet with a high anisotropy field and easy-magnetization axis along the crystallographic *c* axis (see, for example, Ref. 11 and the references cited therein).

The SGXEMS method, proposed in Ref. 12, was used for the investigations. This method is based on the simultaneous detection of Mössbauer spectra in radiations with different mean free paths in the material, specifically, gamma rays, characteristic x rays, and conversion and Auger electrons, which carry information about the properties of the bulk and surface layers of a bulk crystal with a thickness of several μm and 300 nm, respectively. To study the properties of surface layers less than 300 nm thick in the SGXEMS method, secondary-electron selection by energy is performed,[13] since the energy of an electron which has left the sample is progressively lower the greater the depth of the atom whence this electron originated. The SGXEMS method was implemented in the form of the automated system described in Ref. 14.

For the Mössbauer measurements, slabs ~ 100 μm thick were cut from Ba-M single crystals synthesized from a fluxed melt. The crystallographic *c* axis was directed perpendicular to the plane of the slabs. The crystal surfaces were polished chemically (in orthophosphoric acid at temperature $+90\,^{\circ}$C for 1 min). Such treatment of the samples, as was shown in Refs. 15 and 16, gives high-quality preparation of a surface. The SGXEMS method was used to obtain experimental spectra at temperatures from 300 to 750 K. The temperature was maintained constant to within $\pm 0.1\,^{\circ}$C.

The iron ions in Ba-M type ferrites occupy five nonequivalent positions. For this reason, the Mössbauer spectra of these compounds in the temperature range of magnetic ordering consist of five Zeeman sextuplets. The following circumstances make it necessary to increase the accuracy of the mathematical analysis of the experimental spectra. Since the number of magnetic bonds of iron ions occupying nonequivalent positions is different, the effective magnetic fields at the iron nuclei in each sublattice are different, and because the quadrupole splittings are different, the lines in the sextuplets are strongly shifted from one another. In the slabs prepared for the experiments, the crystallographic *c* axis, along which the magnetic moments in the crystal were directed, was oriented perpendicular to the plane of the surface. If a gamma-ray beam is directed parallel to the *c* axis, then on account of the longitudinal Zeeman effect the second and fifth lines of the Zeeman sextuplets will be absent in the Mössbauer spectrum.

The effective magnetic fields, which are presented as a function of temperature in Fig. 2 for iron ions occupying the 12κ and $4f_2$ positions in $BaFe_{12}O_{19}$, were calculated from the experimental spectra. To facilitate interpretation of Fig. 2, the fields at the iron ions in the $4f_1$,$2a$, and $2b$ sublattices are not shown. It should be noted that the parameters of the hyperfine interactions calculated from the experimental Mössbauer spectra of $BaFe_{12}O_{19}$, i.e., for the bulk of the sample, agree well with the published data (see, for example, Refs. 17–19 and the references cited therein).

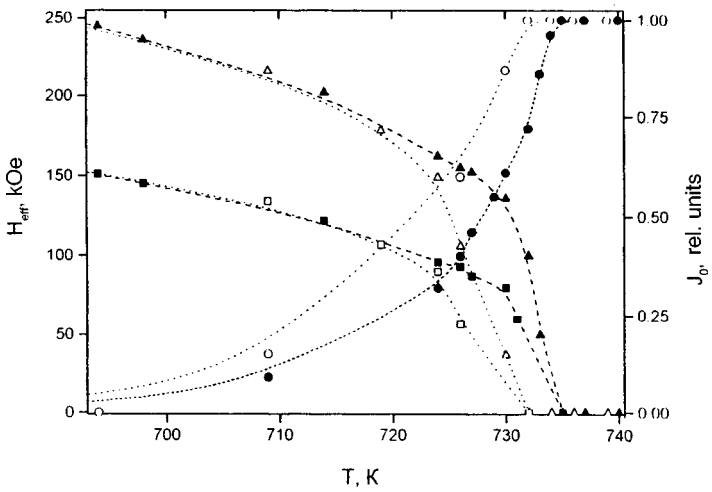

FIG. 2. Temperature dependences of the effective magnetic fields in $BaFe_{12}O_{19}$ at the iron nuclei occupying nonequivalent 12κ and $4f_2$ positions in the bulk of the crystal (■,▲) and in a 200 nm thick surface layer (□,△), as well as the intensity of the paramagnetic line of iron ions located in the bulk (●) and in a surface layer (○).

The temperature of the transition to the paramagnetic state was determined by all the methods employed in Mössbauer spectroscopy: 1) the temperature at which the Zeeman lines vanished in the spectrum and only lines of the paramagnetic phase were observed was determined from the experimental spectra obtained near a phase transition. The temperature at which the total width of the lines in the spectrum equals the width of the lines in the spectrum of the paramagnetic phase was taken as the Curie point. 2) The temperature was determined by the method of temperature scanning, in which the transition point is determined from the temperature dependence of the number of photons detected as the gamma-ray source moves with constant velocity (or with a stationary source). In this case, as one can see from Fig. 2, the number of detected quanta increases as the transition point is approached from the low-temperature side, and then at the transition point the curve saturates, and as the temperature increases further, the number of detected photons remains unchanged. The results obtained by these methods agreed with each other.

As one can see from Fig. 2, the effective magnetic fields obtained from the gamma-ray absorption spectra, i.e., the fields at the iron nuclei located in the bulk of the crystal, vanish at a Curie temperature of 735 K. We note that the temperature dependences of the fields obtained from Mössbauer spectra agree with the data presented by other authors (see, for example, Ref. 20). It follows from Fig. 2 that the effective fields at the iron nuclei located in a $\sim$200 nm thick surface layer of the experimental crystals decrease with increasing temperature more rapidly than the fields on the iron nuclei located in the bulk of this crystal. The magnitudes of the effective magnetic fields determined from the conversion and Auger electron spectra, i.e., the fields at the iron nuclei located in a $\sim$200 nm thick surface layer, vanish at 732 K, which is three degrees lower than the Curie temperature.

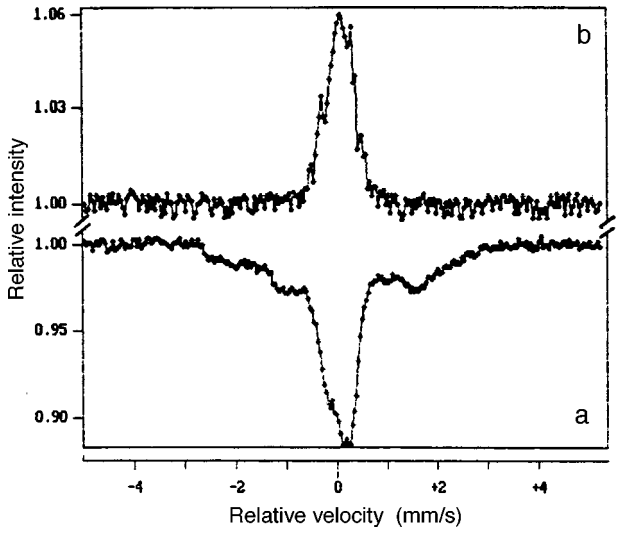

FIG. 3. Mössbauer spectra of $BaFe_{12}O_{19}$, obtained at 732 K by detecting gamma rays (a), i.e., from the bulk of the crystal, and by detecting conversion and Auger electrons (b) from a $\sim$200 nm thick surface layer.

The experimental Mössbauer spectra obtained near the ''order–disorder'' phase transition provide direct confirmation of the result that the surface layer of $BaFe_{12}O_{19}$ crystals transform into the paramagnetic state at a temperature below the Curie point for the bulk of the sample. Examples of such spectra, recorded at $T=732$ K, are presented in Fig. 3. Comparing the spectral data obtained at temperatures somewhat below the Curie point (Fig. 3) shows that Zeeman splitting of the lines, indicating the existence of magnetic ordering in the bulk of the sample, is observed in the Mössbauer spectrum (Fig. 3a), while there are no Zeeman lines in the spectrum obtained by detecting conversion and Auger electrons (Fig. 3b), but rather only the lines corresponding to the paramagnetic state of the sample are observed. It should be noted that our Mössbauer spectra are similar to the spectra obtained by other authors near the Curie point by detecting gamma rays (see Ref. 14 and the references cited therein).

Analysis of the experimental spectra showed that the transition of a bulk ferromagnetic sample to the paramagnetic state occurs as follows. When the crystal is heated, the paramagnetic phase forms on the surface of the crystal, and it arises at temperatures below the Curie point. As temperature increases further, the entire surface of the crystal transforms into the paramagnetic phase, and then the paramagnetic phase propagates into deeper and deeper layers. At the Curie point the thermal energy destroys the magnetic ordering in the entire remaining volume of the crystal. The transition temperature $T_c(L)$ of a thin layer located at a depth L from the surface increases continuously with distance from the surface of the sample, reaching the value T_c for the bulk of the crystal.

As noted above, experimental data indicating that magnetization can exist on the surface of a crystal in the absence of magnetic ordering in the bulk of the crystal have been presented in a number of works (see Refs. 3–5 and 7 and the references cited therein). These results correspond to negative values of the phenomenological order parameter q in the diagram (Fig. 1a) obtained from theoretical investigations.

The experimental results presented in Refs. 8–10 as well as the experimental data described in the present letter show that the transition of the surface of magnets to the paramagnetic state can also occur at temperatures below the Néel (or Curie) point. This conclusion fits in with the theoretical phase diagram (Fig. 1a). On the basis of all experimental results taken together we propose a more accurate phase diagram (Fig. 1b) of the states of the surface and bulk of a crystal near the Curie (Néel) point. As one can see from Fig. 1b, the part of the theoretical phase diagram (Fig. 1a) that corresponds to $q > 0$ is altered. In this case, as the temperature increases, the paramagnetic phase arises first at the surface of the crystal, and this happens at temperatures below the Curie point (see Fig. 1b), when the bulk of the sample is still magnetically ordered. In this temperature range the crystal is in a nonuniform state, specifically, a magnetically disordered surface with a magnetically ordered bulk (the region *DS/OB* in Fig. 1b). However, it cannot be asserted on the basis of the experimental data obtained in the present work that the order parameter is zero in the region of the disordered states. As the temperature increases further, a transition to the paramagnetic phase occurs in increasingly deeper surface layers, and the thermal energy at the Curie point destroys the magnetic ordering in the bulk of the sample, and the entire crystal becomes paramagnetic.

All of the existing experimental data obtained in investigations of the magnetic states of the surface and bulk of macroscopic magnets near the Curie (Néel) fit in the proposed phase diagram presented in Fig. 1b.

In summary, in the present letter direct experimental data indicating that a thin surface layer of macroscopic ferrimagnetic crystals transforms into the paramagnetic state at a temperature below the Curie point for the bulk of the crystal were presented. A phase diagram describing the state of the surface and bulk of a crystal near the Curie (or Néel) temperature was proposed on the basis of all the experimental data.

This work was supported by the Russian Fund for Fundamental Research under Grant No. 98-02-18279.

*e-mail: kamzin@kas.ioffe.rssi.ru

[1] M. I. Kaganov and A. M. Omel'yanchuk, Zh. Éksp. Teor. Fiz. **61,** 1679 (1971) [Sov. Phys. JETP **34**, 895 (1972)].
[2] D. L. Mills, Phys. Rev. **3**, 3887 (1971).
[3] K. Binder, *Magnetic Surface Phenomena, Phase Transitions and Critical Phenomena,* Academic Press, New York, **3,** 325 (1983).
[4] M. P. Kaganov and A. V. Chubukov, in *The Magnetic Properties of Crystalline and Amorphous Media*, Nauka, Novosibirsk, 1989, p. 148.
[5] H. W. Diehl, J. Mod. Phys. B **11,** 3503 (1997).
[6] T. C. Lubensky, H. Rubin Morton, Phys. Rev. B **12**, 3885 (1975).
[7] T. Kaneyoshi, J. Phys.: Condens. Matter **3**, 4497 (1991).
[8] A. S. Kamzin and L. A. Grigor'ev, JETP Lett. **57**, 552 (1993); Zh. Éksp. Teor. Fiz. **105,** 377 (1994) [JETP **78**, 200 (1994)]; Fiz. Tverd. Tela (St. Petersburg) **36,** 1371 (1994) [Phys. Solid State **36**, 765 (1994)]; Fiz. Tverd. Tela (St. Petersburg) **37,** 67 (1995) [Phys. Solid State **37**, 33 (1995)].
[9] A. S. Kamzin, L. A. Grigor'ev, and S. A. Kamzin, Fiz. Tverd. Tela (St. Petersburg) **37,** 67 (1995) [Phys. Solid State **37**, 33 (1995)].
[10] A. S. Kamzin and V. L. Rozenbaum, JETP Lett. **67**, 991 (1995); Fiz. Tverd. Tela (St. Petersburg) **41,** No. 3 (1999), at press [Phys. Solid State].
[11] Sh. Sh. Bashkirov, A. B. Liberman, and V. I. Sinyavskiĭ, *The Magnetic Microstructure of Ferrites*, Kazan State University Press, 1978.

[12] A. S. Kamzin, V. P. Rusakov, and L. A. Grigor'ev, *Proceedings of International Conference on the Physics of Transition Metals*, USSR, Kiev, 1998, Pt. 2, p. 271; Pis'ma Zh. Tekh. Fiz. **16,** 38 (1990) [Sov. Tech. Phys. Lett. **16**, 616 (1990)].
[13] A. S. Kamzin and L. A. Grigor'ev, Pis'ma Zh. Tekh. Fiz. **19**(8), 50 (1993) [Sov. Tech. Phys. Lett. **19**(4), 245 (1993)]; Pis'ma Zh. Tekh. Fiz. **19**(21), 32 (1993) [Sov. Tech. Phys. Lett. **19**(11), 680 (1993)].
[14] A. S. Kamzin, S. M. Irkaev, Yu. N. Mal'tsev, and L. A. Grigor'ev, Prib. Tekh. Éksp., No. 1, 80 (1993).
[15] A. S. Kamzin, L. P. Ol'khovik, and V. L. Rozenbaum, JETP Lett. **61**, 936 (1995); J. Magn. Magn. Mater. **161**, 139 (1996); Zh. Éksp. Teor. Fiz. **111**, 1426 (1997) [JETP **84**, 788 (1997)].; JETP Lett. **67**, 843 (1998); JETP Lett. **67**, 991 (1998).
[16] B. Stahl, R. Gellert, A. S. Kamzin *et al.*, J. Phys. IV France, 7, Coll C1, Suppl. III, C1-219 (1997).
[17] R. H. Fogel and B. J. Evans, J. Appl. Phys. **49**, 1570 (1978).
[18] B. J. Evans, F. Granjean, A. P. Lilot *et al.*, JMMM **67,** 123 (1987).
[19] G. Albanese, M. Garbuciccio, and A. Deriu, Phys. Status Solidi A **23**, 351 (1974).
[20] D. R. Taft, J. Appl. Phys. **35**, 776 (1964).

Translated by M. E. Alferieff

Effect of the nuclear hyperfine field on the 2D electron conductivity in the quantum Hall regime

S. A. Vitkalov
Chemistry Department and National High Magnetic Field Laboratory, University of Florida, Gainesville, Florida 32611-7200 USA;
P. N. Lebedev Physical Institute, Russian Academy of Sciences, 117924 Moscow, Russia

C. R. Bowers
Chemistry Department and National High Magnetic Field Laboratory, University of Florida, Gainesville, Florida 32611-7200 USA

J. A. Simmons and J. L. Reno
Sandia National Laboratories, Albuquerque, NM 87185-1415

(Submitted 19 November 1998; resubmitted 2 December 1998)
Pis'ma Zh. Éksp. Teor. Fiz. **69**, No. 1, 58–63 (10 January 1999)

The effect of the nuclear hyperfine interaction on the dc conductivity of 2D electrons under quantum Hall effect conditions at filling factor $\nu=1$ is observed for the first time. The local hyperfine field enhanced by dynamic nuclear polarization is monitored via the Overhauser shift of the 2D conduction electron spin resonance in AlGaAs/GaAs multiquantum-well samples. The experimentally observed change in the dc conductivity resulting from dynamic nuclear polarization is in agreement with a thermal activation model incorporating the Zeeman energy change due to the hyperfine interaction. The relaxation decay time of the dc conductivity is, within experimental error, the same as the relaxation time of the nuclear spin polarization determined from the Overhauser shift. These findings unequivocally establish the nuclear spin origins of the observed conductivity change. © *1999 American Institute of Physics.* [S0021-3640(99)01201-3]

PACS numbers: 73.40.Hm, 72.15.−v, 73.20.Dx

In conductors and superconductors, fluctuations of the hyperfine contact interaction usually provide the dominant mechanism for nuclear spin relaxation at low temperatures.[1,2] These relaxation times are closely related to the electronic structure and dynamics in these materials. In recent years it has been recognized that the hyperfine interaction can serve as a powerful tool in studies of 2D conducting electron systems. Several notable applications include the quantum Hall effect (QHE)[3] and quantum computation.[4] However, studies of the effect of electron–nuclear spin interactions on the electronic transport are very rare. In nonmagnetic metals the spin–spin interaction between electrons and nuclei is theoretically predicted to produce a strongly magnetic-field and temperature dependent contribution to the resistivity.[5] The contribution of the hyperfine interaction to magnetotransport quantum oscillations of the resistivity has been ob-

served in bulk InSb.[6,7] In a 2D electron system the effect of hyperfine interaction on electron spin resonance (Overhauser effect) has been observed in AlGaAs/GaAs.[8,9] In the present study we demonstrate experimentally that the hyperfine interaction can produce an observable change of the dc conductivity of a 2D electron system under quantum Hall conditions.

To predict the effect of the hyperfine field on the 2D conductivity we use the conventional assumption that the energy of the excitations of the ground state in the QHE near filling factor $\nu=1$ can be expressed as a sum of two terms:[10,11]

$$\Delta=\Delta_0+|g|\mu_B(B_0+B_n), \tag{1}$$

where Δ_0 is the exchange energy due to e–e interaction and $|g|\mu_B B_0$ is the Zeeman term due to the externally applied field B_0. Through the hyperfine field the nuclei provide an additional contribution $|g|\mu_B B_n$ to the 2D ground state excitation energy. Here g is the Landé g factor of the excitations and μ_B is the electron Bohr magneton. The local hyperfine field B_n is proportional to the nuclear spin polarization, $B_n=a\langle I_z\rangle$,[12,13] where a is the contact hyperfine coupling constant. At temperatures much greater than a few mK, the thermal equilibrium hyperfine field $B_n^{\rm eq}$ can ordinarily be neglected. In the context of electron spin resonance (ESR), B_n is known as the Overhauser shift.[8,13,14] In the absence of spin–orbit interaction, as in the conduction band of GaAs,[11,15] neither the cyclotron energy nor the electron–electron Coulomb interactions are affected by B_n, regardless of its magnitude or sign, because the origin of B_n is the spin–spin coupling between the electron and nucleus.

Under our experimental conditions, where $T\approx 2.5$ K and $B_0=5.35$ T, the longitudinal conductivity at $\nu=1$ obeys an Arrhenius law:

$$\sigma_{xx}=\sigma_0\exp(-\Delta/2kT), \tag{2}$$

where σ_0 is a constant. In the thermally activated regime the energy gap Δ can be determined from the temperature dependence of σ_{xx}. Consider the conductivity change that would result from a change in the nuclear polarization: through the collective hyperfine interaction of the 2D electrons with the nuclei in the vicinity of the 2D electrons, the local nuclear hyperfine field B_n will be enhanced. For a small change in the hyperfine field, $\delta B_n \ll B_0$, we will have from (1) and (2):

$$\delta\sigma_{xx}/\sigma_{xx}=-|g|\mu_B\delta B_n/2kT=\alpha\delta B_n/B_0, \tag{3}$$

where $\alpha=-|g|\mu_B B_0/2kT$ is a constant. Experimentally we measured the dc conductivity of the AlGaAs/GaAs multiquantum well samples by the standard four probe method in magnetic fields up to $B_0=6$ T and temperatures $T=1.7$–4.2 K. To obtain the 2D longitudinal conductivity σ_{xx} we measured the longitudinal resistivity $\rho_{xx}=\beta U_{xx}/I$ and the Hall resistivity $\rho_{xy}=U_{xy}/I$, where β is a geometric factor, I is the current through the sample, and U_{xx} and U_{xy} are the longitudinal and Hall voltages. To calculate the 2D conductivity we used the standard formula $\sigma_{xx}=\rho_{xx}/(\rho_{xx}^2+\rho_{xy}^2)$.

According to (3) the relative dc conductivity change is proportional to the change in the nuclear hyperfine field B_n. To observe this dependence experimentally, we have employed the method of dynamic nuclear polarization (DNP) by down-field swept ESR to enhance the magnitude of $\langle I_z\rangle$.[8,9] The corresponding DNP-enhanced hyperfine field is $B_n^{\rm DNP}$. The change in the Overhauser shift of the ESR line is given by $\delta B_n=B_n^{\rm DNP}$

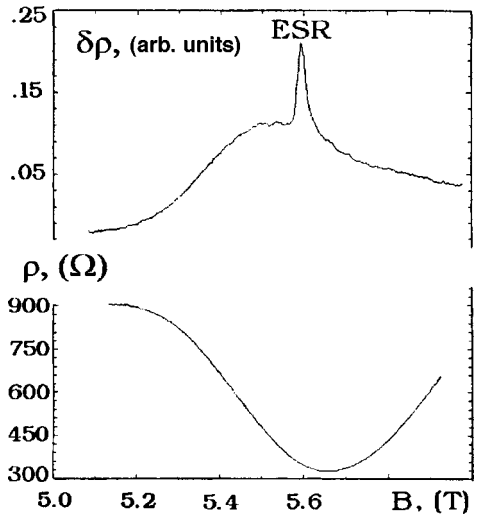

FIG. 1. Magnetic field dependence of the longitudinal resistivity per layer (lower curve) and variation of the resistivity induced by microwave excitation near filling factor $\nu=1$ in sample EA124. The ESR line position corresponds to $g=-0.415$. The spectrum was recorded at a microwave frequency of 32.48 GHz and at $T=1.7$ K. The angle between B_0 and the normal to the sample is 60°.

$-B_n^{\mathrm{eq}}$ (Refs. 8, 13, and 14). The 2D electron spin resonance signal is detected electrically as described in a previous paper[16] on single AlGaAs/GaAs heterojunctions. The mechanism for this phenomenon is not yet fully understood, but it nevertheless provides a working method to detect and control the Zeeman energy term.[8,9]

We have studied two different GaAs/AlGaAs multiquantum well samples. The samples were grown by molecular beam epitaxy and have the following properties at $T=4.2$ K: sample EA124 (21 GaAs wells) has a 2D electron density per layer of $6.9\times10^{10}\,\mathrm{cm}^{-2}$ and mobility $\mu=440\,000$ V/cm^{2}s; sample EA216 (40 GaAs wells) has a 2D density of $1.2\times10^{11}\,\mathrm{cm}^{-2}$ and mobility $\mu=650\,000$ V/cm^{2}s. The samples were mounted on a rotation stage to allow $\nu=1$ to be obtained over a range of magnetic fields. We measured ρ_{xx} at a frequency of 524 Hz using a lock-in amplifier. Application of the microwave power to the sample induced a change in ρ_{xx} which is detected on the output signal of the amplifier. To increase the sensitivity for ESR detection, the microwave power was modulated at a frequency of 7 Hz. The output of this amplifier was connected to the input of a second lock-in amplifier which detected $\Delta\rho_{xx}$ induced by the microwave excitation at 7 Hz. This method helps to avoid the rectification signal at 7 Hz which is induced by the microwave electromagnetic field. In Fig. 1 we present an example of the electrically detected 2D electron spin resonance at filling factor $\nu=1$, recorded using a microwave frequency of 32.48 GHz. Also shown is the longitudinal magnetoresistance at $T=1.7$ K for sample EA124.

To polarize the nuclei the microwave generator was switched to continuous mode with no modulation.[16] The magnetic field was first set to a value slightly higher than the ESR condition, and the field was then swept down. The resonant microwaves begin to polarize the nuclei through saturation of ESR transitions.[8,13,14] As the nuclear polarization

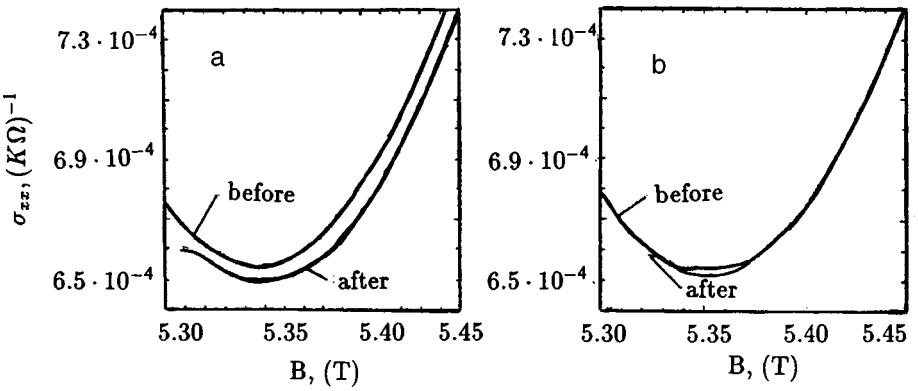

FIG. 2. Magnetic field dependences of the 2D longitudinal conductivity per layer before and after microwave irradiation of the sample, obtained at $T=2.5$ K in sample EA124. In experiment (a) the nuclei were dynamically polarized by resonant saturation of the electron spin transition. A microwave frequency of 32GHz was employed, corresponding to ESR at 5.5 T with the nuclei at thermal equilibrium. In experiment (b), the conductivity was recorded before and after off-resonant microwave excitation of the sample. The same microwave power was applied as in part (a), but the microwave frequency of 20.8 GHz (corresponding to an ESR field of 3.58 T) was far from the ESR condition, resulting in no dynamic nuclear polarization enhancement.

increases, the hyperfine field B_n due to the nuclei acting on the electrons also increases, resulting in the Overhauser shift of the ESR line. In GaAs this shift is to lower magnetic field,[8,17] because B_n is positive and adds constructively to B_0 due to the negative sign of the g factor. By choosing an appropriate down-sweep rate, it is possible to shift the ESR line considerably.[8] The maximum ESR shift that we obtained by microwave DNP was $B_n=0.2$ T at $B_0=5.5$ T.

In accordance with (3) the enhancement of the nuclear hyperfine field B_n should change the longitudinal dc conductivity σ_{xx} of the 2D electrons under QHE conditions. In Fig. 2 we present the magnetic field dependences of σ_{xx} for EA124 at $T=2.5$ K. To observe the change $\delta\sigma_{xx}$ due to δB_n, we first measured $\sigma_{xx}^{\mathrm{eq}}(B_0)$ with a magnetic field up-sweep without microwave excitation, with the nuclei in thermal equilibrium with the lattice. This conductivity trace is labeled *before* in Fig. 2a. To ensure that the nuclear spin system was initially at thermal equilibrium with the lattice, the 2D electron system was taken just outside of the $\nu=1$ magnetoresistance minimum for 300–600 s before the first sweep. The relaxation of the Overhauser shift of the ESR indicates that the nuclear spin relaxation time T_{1n} is about 60–120 s under these conditions, in reasonable agreement with previous reports.[9] After $\sigma_{xx}^{\mathrm{eq}}(B_0)$ was recorded in the first sweep, the nuclei were dynamically polarized by the down-swept DNP procedure[8] at a sweep rate $dB/dt=0.5$ mT/s near $\nu=1$. The microwave power was then switched off, and $\sigma_{xx}^{\mathrm{DNP}}(B_0)$ was recorded during a second magnetic field up-sweep, this time with the nuclear spin system highly polarized (Fig. 2a). This is the trace labeled *after* in Fig. 2a.

Using electrically detected ESR we also measured the Overhauser shift of the ESR line as a function of time using multiple detection up-sweeps. The relaxation time of the Overhauser shift at $\nu=1$ and $T=2.7$ K was observed to be 240–300 s. Since this is much longer than the time scale of the ESR detection up-sweep (about 30 s), the amount of

nuclear spin relaxation which occurs during the up-sweep is small and can be neglected for the purposes of this paper.

To eliminate the possibility that the observed time evolution of the conductivity is due to some sort of persistent microwave photoconductivity effect, the dc conductivity was measured using exactly the same procedure as in the resonant DNP experiment but with *nonresonant* microwave excitation of the sample at frequencies far from the ESR condition. The result is that nonresonant microwave excitation changes neither position of the ESR line nor the dc conductivity of sample EA124. The conductivity traces obtained before and after nonresonant excitation are therefore overlapping, as is evident from Fig. 2b.

We now estimate the value of the relative dc conductivity change due to the change δB_n induced by DNP according to (3) and compare this with the data represented in Fig. 2a. Let B_0^s be the magnetic field satisfying the ESR condition in the absence of the hyperfine field (e.g., nuclei unpolarized). The difference between the ESR fields before (at thermal equilibrium) and immediately after enhancement of the nuclear polarization is given by $\delta B_n=(B_0^s-B_n^{\rm eq})-(B_0^s-B_n^{\rm DNP})=B_n^{\rm DNP}-B_n^{\rm eq}$. The observed time dependence of the Overhauser shift demonstrates that the position of the ESR line immediately after switching off the microwaves at the end of the DNP down-sweep coincides well with $B_0^s-B_n^{\rm DNP}$. In the experiment corresponding to Fig. 2a, the ESR was shifted from its equilibrium position $B_0^s-B_n^{\rm eq}=5.503$ T to $B_0^s-B_n^{\rm DNP}=5.304$ T, and therefore $\delta B_n=199$ mT. In accordance with relation (3) the dc conductivity variation due to $B_n^{\rm DNP}$ should be $\delta\sigma_{xx}^{\rm theor}=7.3\times10^{-6}\,{\rm k}\Omega^{-1}$. The g factor $g=-0.415$ used to calculate $\delta\sigma_{xx}^{\rm theor}$ was determined from ESR (see Fig. 1). Using the experimental data from Fig. 2a, the dc conductivity change due to δB_n was found to be $\delta\sigma_{xx}^{\rm exp}=8\times10^{-6}\,{\rm k}\Omega^{-1}$. This value corresponds to the difference between the minima of the $\sigma_{xx}(B_0)$ curves before and after enhancement of the nuclear spin polarization. Hence, there is reasonable agreement between the experiment and the simple theoretical estimate of the conductivity change due to DNP enhancement of the nuclear polarization.

Figure 3a presents the relaxation decay of the change in the ESR position $\delta B_n(t)/B_0^s$ for sample EA216, obtained from ESR by multiple magnetic field up-sweeps during a period of 800 s immediately following the initial DNP down-sweep. The time dependence was fit to an exponential decay function: $\delta B_n(t)\propto\exp(-t/T_{1n})$, yielding $T_{1n}=217\,{\rm s}$ at $\nu=1$ and $T=2.5\,{\rm K}$. The time T_{1n} is comparable with the relaxation times obtained in Ref. 9.

The relaxation decay of the dc conductivity change of EA216 immediately following the DNP down-sweep is presented in Fig. 3b. The relative variation of the conductivity $\delta\sigma_{xx}/\sigma_{xx}=(\sigma_{xx}(t)-\sigma_{xx}^{\rm eq})/\sigma_{xx}^{\rm eq}$ was obtained by subtracting σ_{xx}^{eq} at the conductivity minimum before DNP from the dc magnetoconductivity minima which were measured during the relaxation decay period immediately following DNP. In this procedure the $\sigma_{xx}(B_0)$ traces were recorded over a small region around $\nu=1$ using multiple up and down field sweeps during a period of about 800 s. The Overhauser shift obtained at the termination of the DNP down-sweep was $\delta B_n(t=0)/B=0.021$. This value and $T_{1n}=217$ s were used to plot the expression $\delta\sigma_{xx}(t)/\sigma_{xx}^{\rm eq}=\alpha(\delta B_n/B)\exp(-t/T_{1n})$ in Fig. 3b. The value of α is based on the g factor measured by ESR. Quantitative agreement between this model and the experimental data is obtained with no adjustable parameters.

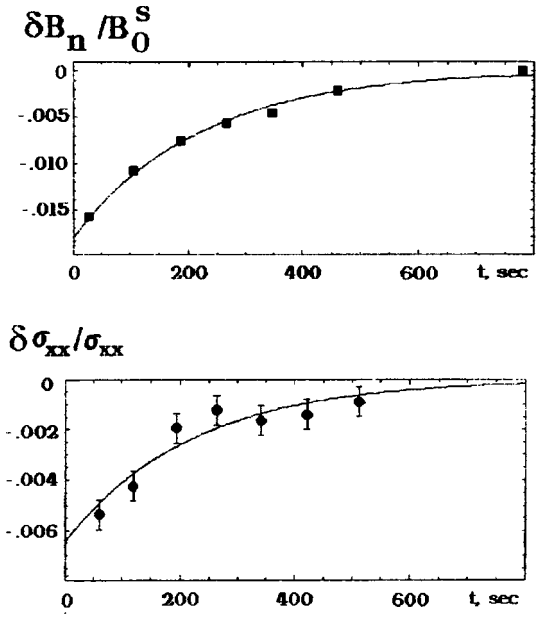

FIG. 3. Time dependence of the relative Overhauser shift $\delta B_n/B_0^s$ of the 2D electron spin resonance following DNP at $T=2.5$ K in sample EA216. The solid line represents an exponential fit to the data. The relaxation time obtained from the fitting is $T_{1n}=217$ s. Part (b) shows the time dependence of the relative variation of the longitudinal conductivity, $\delta\sigma_{xx}/\sigma_{xx}$, obtained by a sequence of magnetic field up-sweeps following an initial DNP down-sweep. The solid line represents a theoretical calculation of the effect using (4) with no adjustable parameters.

In conclusion, we have observed the effect of the nuclear hyperfine field on the dc conductivity of 2D electrons under quantum Hall effect conditions in AlGaAs/GaAs multiquantum wells at filling factor $\nu=1$. The nuclear spin polarization was enhanced using dynamic nuclear polarization, whereby the nuclei become polarized due to cross relaxation with electrons being driven by ESR transitions into a nonequilibrium polarization state. The hyperpolarized nuclei produce a local hyperfine field which is experienced by the electron spins. The resulting Overhauser shift of the ESR transition was measured using electrically detected ESR. The value of the dc conductivity change due to the nuclear spin polarization corresponds quantitatively to the thermal activation model incorporating the nuclear hyperfine field into the Zeeman energy of the charged ground-state excitations. The dc conductivity decay time measured experimentally is, within experimental error, the same as the nuclear spin–lattice relaxation time observed via Overhauser shift measurements near filling factor $\nu=1$. These findings unequivocally establish the nuclear-spin origins of the observed conductivity changes.

We thank N. Bonesteel, L. Engel, J. Graybeal, I. Kukushkin, N. Sibeldin, D. Thouless, and I. D. Vagner for helpful discussions. We also express our appreciation to Mark Whitton and Bobby Joe Pullum for experimental help, and to Bruce Brandt for superb management of the NHMFL facilities. This work was supported by NSF Grant CHE-9624243 and Project 97-1040, Physics of Solid State Nanostructures, Russia. The work at Sandia was supported by the U. S. Department of Energy under Contract DE-

AC04-94AL85000. A portion of this work was performed at the NHMFL, which is supported by NSF Cooperative Agreement DMR-9527035 and by the State of Florida.

[1] C. P. Slichter, *Principles of Magnetic Resonance*, Springer, Berlin, 1991.
[2] J. Winter, *Magnetic Resonance in Metals*, Clarendon Press, Oxford, 1971.
[3] I. D. Vagner and T. Maniv, Physica B **204**, 141 (1995).
[4] V. Privman, I. D. Vagner, and G. Kventsel, Phys. Lett. A **239**, 141 (1998).
[5] A. M. Dugaev, I. D. Vagner, and P. Wyder, JETP Lett. **64**, 211 (1996).
[6] B. Sapoval, D. Kaplan, and G. Lampel, Solid State Commun. **9**, 1591 (1971).
[7] N. Gauss and A. G. M. Jansen, Czech. J. Phys. **46**, S4, 2037 (1996).
[8] M. Dobers, K. von Klitzing, J. Schneider, G. Weinmann, and K. PLoog, Phys. Rev. Lett. **72**, 1650 (1988).
[9] A. Berg, M. Dober, R. R. Gerhardts, and K. von Klitzing, Phys. Rev. Lett. **64**, 2563 (1990).
[10] A. Schmeller, J. P. Eisenstein, L. N. Pfeiffer, and K. W. West, Phys. Rev. Lett. **75**, 4290 (1995).
[11] F. F. Fang and P. J. Stiles, Phys. Rev. **174**, 823 (1968).
[12] D. Paget, G. Lampel, B. Sapoval, and V. I. Safarov, Phys. Rev. B **15**, 5780 (1977).
[13] A. Abragam, *The Principles of Nuclear Magnetism*, Clarendon Press, Oxford, 1961, p. 191.
[14] A. W. Overhauser, Phys. Rev. **92**, 411 (1953).
[15] S. A. Vitkalov, JETP **82**, 994 (1996).
[16] D. Stein, K. von Klitzing, and G. Weimann, Phys. Rev. Lett. **51**, 130 (1983).
[17] C. R. Bowers, Solid State Nucl. Magn. Reson. **11**, 11 (1998), and references therein.

Published in English in the original Russian journal. Edited by Steve Torstveit.

The $\rho^{\pm}-\rho^{0}$ mass splitting problem

M. N. Achasov*
G. I. Budker Institute of Nuclear Physics, 630090 Novosibirsk 90, Russia

N. N. Achasov†
S. L. Sobolev Institute of Mathematics, 630090 Novosibirsk 90, Russia

(Submitted 30 November 1998)
Pis'ma Zh. Éksp. Teor. Fiz. **69**, No. 1, 8–11 (10 January 1999)

The problem of the $\rho^{\pm}-\rho^{0}$ mass splitting is discussed. It is suggested to use the $\phi\to\rho\pi\to 3\pi$ decay to measure the $\rho^{\pm}-\rho^{0}$ mass splitting.
 [S0021-3640(99)00201-7]

PACS numbers: 13.25.Jx, 13.40.Dk

In the framework of the $SU(3)$ theory with U-spin invariance of electromagnetic interactions, with the ideal $\omega-\phi$ mixing taken into account and with the $\rho^{0}-\phi$ mixing ignored for reasons of the Okubo–Zweig–Iizuki rule, it has been found[1] for the $\rho^{0}-\omega$ mixing that

$$-\mathrm{Re}(\Pi_{\rho^0\omega})=(m^2_{K^{*\pm}}-m^2_{K^{*0}})-(m^2_{\rho^{*\pm}}-m^2_{\rho^{*0}}). \tag{1}$$

The advent of quantum chromodynamics did not affect Eq. (1), since the U-spin invariance of isospin symmetry breaking interactions was not affected. Now, however, the importance of the $u-d$ quark mass splitting in the isospin symmetry breaking is perceived (see, for example, the review[2]). Equation (1) is correct to terms caused by both isospin symmetry breaking interactions and $SU(3)$ symmetry breaking interactions (''semi-strong interactions''). It means that corrections to Eq. (1) of up to 25% are possible.

The Particle Data Group[3] gives for the $K^{*\pm}-K^{*0}$ mass splitting

$$m_{K^{*0}}-m_{K^{*\pm}}=6.7\pm 1.2\ \text{MeV}, \tag{2}$$

and for the $\rho^{\pm}-\rho^{0}$ mass splitting

$$m_{\rho^0}-m_{\rho^{\pm}}=0.1\pm 0.9\ \text{MeV}. \tag{3}$$

But the $\rho^{\pm}-\rho^{0}$ mass splitting can be calculated with Eq. (1), taking into account the well-specified $\omega\to\pi^{+}\pi^{-}$ decay.[3]

Acually, as was first pointed by Glashow,[4] the ω meson decays into $\pi^{+}\pi^{-}$ via the $\rho^{0}-\omega$ mixing (see also, for example, Refs. 5–9),

$$B(\omega\to\pi^{+}\pi^{-})=\frac{\Gamma(\rho^{0}\to\pi^{+}\pi^{-};\ m_{\omega})}{\Gamma_{\omega}}\left|\frac{\Pi_{\rho^0\omega}}{m^2_{\omega}-m^2_{\rho^0}-i\cdot m_{\omega}(\Gamma_{\omega}(m_{\omega})-\Gamma^{0}_{\rho}(m_{\omega}))}\right|^2. \tag{4}$$

It is known[5–9] that $\mathrm{Im}(\Pi_{\rho^0\omega})$ can be ignored. Besides, the interference pattern of the ρ^0 and ω mesons in the reaction $e^+e^-\to\pi^+\pi^-$ and in $\pi^+\pi^-$ photoproduction on nuclei shows[5–9] that $\mathrm{Re}(\Pi_{\rho^0\omega})<0$. So, taking into account that $B(\omega\to\pi^+\pi^-)=0.0221\pm0.003$ (Ref. 3), one gets

$$-\mathrm{Re}(\Pi_{\rho^0\omega})=-(3.91\pm0.27)\times10^{-3}\ \mathrm{GeV}^2. \tag{5}$$

It follows from Eqs. (1), (2) and (5) that

$$m_{\rho^0}-m_{\rho^\pm}=5.26\pm1.41\ \mathrm{MeV}. \tag{6}$$

This result is a puzzle. First, this mass splitting is considerable and contrary to Eq. (3). Second, it is largely of electromagnetic origin, like the $\pi^\pm-\pi^0$ splitting, but it has the opposite sign. The ρ^0 meson is heavier than the $\rho^\pm$!

If one considers the linear version of Eq. (1),[1)] then $m_{\rho^0}-m_{\rho^\pm}=4.1\pm1.2$ MeV, and the situation remains essentially unchanged. Of course, it may be that corrections to Eq. (1) are important, but the current theoretical understanding of the vector meson mass splitting in the isotopical multiplets is far from perfect (see, for example, Refs. 2,10–12).

As to the value given in Eq. (3), it was obtained[13] by fitting the $\tau^-\to\nu_\tau\pi^-\pi^0$ data[13] in combination with the $e^+e^-\to\pi^+\pi^-$ data,[14] for which the production mechanism is the same except for the $\rho^0-\omega$ mixing. But a combined fit of different experiments is prone to sizable systematic errors. That is why the problem of an alternative experimental measurement of the $\rho^\pm-\rho^0$ mass splitting is quite topical. But this task is a considerable challenge, for it is practically meaningless to compare different experiments with different ρ production mechanisms in view of the large width of the ρ meson. The point is that our current knowledge of hadron production mechanisms is far from perfect, and generally in the resonance region we have a spectrum

$$\frac{dN}{dE}\sim\frac{f(E)}{(E-E_R)^2+\Gamma^2/4}, \tag{7}$$

where $f(E)$ is an unknown function which is poorly varying in the resonance region[2)] and which can shift the visible peak as much as several MeV from E_R. Indeed, let take into account two first terms of expansion of $f(E)$ in the resonance region:

$$f(E)=f_0+(E-E_R)f_1+\ldots. \tag{8}$$

Then the shift of the visible peak is

$$\Delta E_R=\frac{\Gamma^2}{8}\cdot\frac{f_1}{f_0}. \tag{9}$$

So, if $f_1=\pm f_0/4.72\Gamma=\pm1.4f_0\ \mathrm{GeV}^{-1}$ and $\Gamma=151$ MeV, then

$$\Delta E_R=\pm4\ \mathrm{MeV}. \tag{10}$$

Certainly, one can use instead of $e^+e^-\to\pi^+\pi^-$ and $\tau^-\to\nu_\tau\pi^-\pi^0$ some other processes with the same $\rho^\pm$ and ρ^0 production mechanism, for example, $a_1^-(1260)\to\rho^-\pi^0\to\to\pi^-\pi^0\pi^0$ and[3)] $a_1^-(1260)\to\rho^0\pi^-\to\pi^+\pi^-\pi^-$, the advantage of which is the absence of the $\rho^0-\omega$ mixing. But in this case the problem of different experimental systematic errors also exists.

It seems to us that the most suitable process for the aim under discussion is the $\phi \to \rho^+\pi^- + \rho^-\pi^+ + \rho^0\pi^0 \to \pi^+\pi^-\pi^0$ decay. Indeed, the charged and neutral ρ mesons are produced in one reaction with the same mechanisms. By now the Spherical Neutral Detector (SND) and Cryogenic Magnetic Detector-2 at the e^+e^- collider VEPP-2M in Novosibirsk have already collected $\sim 10^7$ ϕ mesons each, i.e., $\sim 10^6$ $\phi \to \rho\pi \to 3\pi$ decays each. With the ϕ factory DAΦNE in Frascati, two orders of magnitude larger statistics will be collected.

The differential cross section of the $e^+e^- \to \pi^+(k_+)\pi^-(k_-)\pi^0(k)$ reaction can be written in the symmetrical form[15,16]

$$\frac{d\sigma}{dm_+^2\,dm_-^2\,dm^2\,d\cos\vartheta_N\,d\varphi} = \frac{\alpha^2|\mathbf{k}_+|^2|\mathbf{k}_-|^2\sin^2\vartheta_{+-}\sin^2\vartheta_N}{128\pi^2 s^2} \times |F|^2\delta(m_+^2 + m_-^2 + m^2 - s - 2m_{\pi^+}^2 - m_{\pi^0}^2), \tag{11}$$

where $m_+^2 = (k_+ + k)^2$, $m_-^2 = (k_- + k)^2$, $m^2 = (k_+ + k_-)^2$, $s = (k_+ + k_- + k)^2$, ϑ_N is the angle between the normal to the production plane and the e^+e^- beam direction in the center mass system, ϑ_{+-} is the angle between the directions of the π^+ and π^- momenta in the center mass system.

The form factor F of the $\gamma^* \to \rho\pi$ decay with the $\rho^0 - \omega$ mixing taken into account has the form

$$F = A_\rho(s,m_+)\frac{2g_{\rho\pi\pi}(m_+)}{D_{\rho^+}(m_+)}\exp\{i\cdot\delta(m_+)\} + A_\rho(s,m_-)\frac{2g_{\rho\pi\pi}(m_-)}{D_{\rho^-}(m_-)}\exp\{i\cdot\delta(m_-)\} + A_\rho(s,m)\frac{2g_{\rho\pi\pi}(m)}{D_{\rho^0}(m)}\exp\{i\cdot\delta(m)\}\left(1 + \frac{A_\omega(s)}{A_\rho(s,m)}\frac{\Pi_{\rho^0\omega}}{D_\omega(m)}\exp\{-i\cdot\delta(m)\}\right), \tag{12}$$

where $D_V(x)$ is the V meson propagator; in the simplest case $D_V(x) = m_V^2 - x^2 - i\cdot x\Gamma_V(x)$, $\Gamma_\rho(x) = (g_{\rho\pi\pi}^2(x)/6\pi)(q_\pi^3(x)/x^2)$; to good accuracy one can consider that the propagators of the $\rho^\pm$ and ρ^0 mesons differ by values of the masses $m_{\rho^\pm}^2$ and $m_{\rho^0}^2$ only; $\delta(x)$ is a phase due to the triangle singularity (the Landau anomalous thresholds).[17]

At the ϕ meson energy $|A_\omega(s)/A_\rho(s\,,m)| \simeq 0.02$, i.e., the $\rho^0 - \omega$ mixing effects are negligible. As the energy ($\sqrt{s}$) increases, the interference between terms in Eq. (12) decreases and is unimportant at $\sqrt{s} = 1.5$–2 GeV; this circumstance is a favorable one for the aim under consideration, but the statistics in this energy region are poor, and, besides, the $\rho^0 - \omega$ effects in this energy region are expected to be considerable.[16,17]

The $J/\psi \to \rho\pi \to 3\pi$ decay stands alone. Generally speaking, one can expect adequate statistics in the future for $B(J/\psi \to \rho\pi) = (1.28 \pm 0.1) \times 10^{-2}$. The interference between the terms in Eq. (12) is practically absent here, but the $\rho^0 - \omega$ mixing effects can essentially prevent the measurement of the $\rho^\pm - \rho^0$ mass splitting $B(J/\psi \to \rho^0\pi^0 = (4.2 \pm 0.5) \times 10^{-3})$ and $B(J/\psi \to \omega\pi^0 = (4.2 \pm 0.6) \times 10^{-4})$, especially since the relative

phase of the amplitudes of the $J/\psi\to\rho^0\pi^0$ and $J/\psi\to\omega\pi^0$ decays is unknown. Incorporation of the effects of the heavy ρ' mesons in the $J/\psi\to 3\pi$ decay can be found in Ref. 18.

We thank A. A. Kozhevnikov, G. N. Shestakov and A. M. Zaitsev for helpful discussions.

The present work was supported in part by the grant INTAS-94-3986.

*e-mail: achasov@math.nsc.ru
†e-mail: achasov@inp.nsk.su
[1)]The linear relation occurs, for example, in the heavy vector meson chiral Lagrangian.[11]
[2)]Detection efficiencies can play the role of such functions for different processes with the same ρ production mechanism.
[3)]A. M. Zaitsev, private communication.

[1] M. Gourdin, *Unitary Symmetries*, North Holland, Amsterdam, 1967.
[2] J. Gasser and H. Leutwyler, Phys. Rep. **87**, 77 (1982).
[3] Particle Data Group, Eur. Rev. J. C **3**, 1 (1998).
[4] S. L. Glashow, Phys. Rev. Lett. **7**, 469 (1961).
[5] A. S. Goldhaber, G. S. Fox, and C. Quigg, Phys. Lett. B **30**, 249 (1969).
[6] M. Gourdin, L. Stodolsky, and F. M. Renard, Phys. Lett. B **30**, 347 (1969).
[7] F. M. Renard, Nucl. Phys. B **15**, 118 (1970).
[8] N. N. Achasov and G. N. Shestakov, Nucl. Phys. B **45**, 93 (1972); Fiz. Élem. Chastits. At. Yadra **9**, 48 (1978) [Sov. J. Part. Nucl. **9**, 19 (1978)].
[9] N. N. Achasov and A. A. Kozhevnikov, Yad. Fiz. **55**, 809 (1992) [Sov. J. Nucl. Phys. **55**, 449 (1992)]; Int. J. Mod. Phys. A **7**, 4825 (1992).
[10] J. Schechter, A. Subbaraman, and H. Weigel, Phys. Rev. D **48**, 339 (1993).
[11] J. Bijnens and P. Gosdzinsky, Phys. Lett. B **388**, 203 (1996); J. Bijnens, P. Gosdzinsky, and P. Talavera, Nucl. Phys. B **501**, 495 (1997).
[12] Dao-Neng Gao, Bing An Li and Mu-Lin Yan, Phys. Rev. D **56**, 4115 (1997).
[13] R. Barate *et al.*, Z. Phys. C **76**, 15 (1997).
[14] L. M. Barkov *et al.*, Nucl. Phys. B **256**, 365 (1985).
[15] M. Gell-Mann, D. Sharp, and W. Wagner, Phys. Rev. Lett. **8**, 261 (1962); J. Yellin, Phys. Rev. **147**, 1080 (1966); G. Altarelli *et al.*, Nuovo Cimento A **47**, 113 (1967).
[16] N. N. Achasov, A. A. Kozhevnikov, and G. N. Shestakov, Phys. Lett. B **50**, 448 (1974); N. N. Achasov, N. M. Budnev, A. A. Kozhevnikov, and G. N. Shestakov, Yad. Fiz. **23**, 610 (1976) [Sov. J. Nucl. Phys. **23**, 320 (1976)].
[17] N. N. Achasov and A. A. Kozhevnikov, Phys. Rev. D **49**, 5773 (1994).
[18] N. N. Achasov and A. A. Kozhevnikov, Phys. Rev. D **55**, 2663 (1997).

Published in English in the original Russian journal. Edited by Steve Torstveit.

Conductance of a 2D Corbino disk under QHE conditions in the presence of contact phenomena

V. B. Shikin

Institute of Solid-State Physics, Russian Academy of Sciences, 142432 Chernogolovka, Moscow Region, Russia

(Submitted 3 December 1998)
Pis'ma Zh. Éksp. Teor. Fiz. **69**, No. 1, 64–69 (10 January 1999)

It is noted that contacts of a two-dimensional (2DEG) electronic system with ''external'' metallic electrodes destroy the spatial uniformity of the density of the system. This gives rise to specific dimensional effects for the conductance of an unscreened Corbino disk in a magnetic field sufficient for the appearance of local regions with an integer-valued filling factor in the electron density profile. The overall pattern of the transport voltage distribution along the disk is seriously transformed. It becomes possible to explain the large (compared with the cyclotron energy) values of the critical transport voltage, leading to breakdown of the QHE regime. The experiment qualitatively confirms the predictions of the theory. © *1999 American Institute of Physics.*
[S0021-3640(99)01301-8]

PACS numbers: 73.40.Jn

Contact phenomena at the boundaries of three-dimensional (3D) and two-dimensional (2D) systems are virtually inevitable (see, for example, the section entitled ''Contact potential difference'' in Ref. 1) and lead to a number of observable consequences. For example, in the 2D case there arise specific dimensional effects in the conductivity of 2D semiconductor strips,[2] unusual contact-induced magnetooscillations of the conductance in a screened Corbino disk with low electron density,[3] direct observations of a nonuniform distribution of the electrical potential along a Corbino disk with metal terminals,[4,5] and so on.

The purpose of this letter is to discuss the role of contact phenomena in the formation of the conductance of a 2D Corbino disk under conditions giving rise to the appearance in the disk of individual ''incompressible'' strips with magnetic filling factor close to an integer. As shown below, a contact-induced perturbation of the 2D electron density stimulates under QHE conditions the appearance of so-called incompressible strips with an integer-valued magnetic filling factor. The properties of these strips, which determine mainly the value of the conductance of a Corbino disk, are very sensitive to the overall geometry of the problem, and this is also reflected in the conductance. It is found that the conductance of integer strips is strong nonuniform over their cross section. It is noted that a large number of strips can appear within the 2D region of a Corbino disk. Experimental evidence in favor of the proposed theory is presented.

1. We recall first the results of classical electrostatics for the charge distribution in the combination metal – 2D system – metal with different internal characteristics. This is effectively taken into account by introducing a contact potential difference ϕ_{ab} between the ''partners'':[1]

$$e\phi_{ab}=W_a-W_b, \tag{1}$$

where W_i are the so-called work functions of the corresponding conducting systems and e is the elementary charge.

Omitting the details, which are presented in, for example, Ref. 5, we have with adequate accuracy the following distribution of the perturbed electron density of contact origin:

$$\delta n_0(x)=\frac{\kappa w\phi_{ab}}{\pi^2 e(w^2-x^2)}. \tag{2}$$

Here $2w$ is the width of the 2D region between the metallic edges. In the limit $a_b^*\ll w$, the approximation (2) works well far from the points $x=\pm w$.

Turning to the situation with the quantum Hall effect (QHE), we shall determine first which parts of the disk satisfy the requirement at the filling factor be an integer, if the 2D system is initially spatially inhomogeneous. Existing results on this subject are contained in a series of works.[6–8] Here it is shown that for a fixed curvature $n''(0)$ of the classical electron density distribution at its extremal point (the point where the first derivative vanishes $n'(0)=0$), the width $2a_c$ of the central plateau where the filling factor is an integer $\nu_i=1,2,3,i,\ \ldots$, is found to be

$$n''(0)a_c^2/4=[\nu(0)-\nu_i]n_H, \quad n''(0)=d^2n(0)/dx^2, \tag{3}$$

$$\nu(0)=n(0)/n_H, \quad n_H^{-1}=\pi l_H^2, \quad l_H^2=\frac{c\hbar}{eH}, \tag{4}$$

H is the intensity of the magnetic field oriented in a direction normal to the plane of the disk. The width $2a_c$ is maximum when the additional Coulomb energy a rising in connection with the deformation of the initial classical electron density $n(x)$ equals the cyclotron energy $\hbar\omega_c$. Then

$$a_{\max}^3=\frac{3\kappa\hbar\omega_c}{\pi e^2|n''(0)|}. \tag{5}$$

Substituting into the definition (5) $n''(0)$ following from Eq. (2) we have

$$(a_{\max}/w)^3=\frac{3\pi\hbar\omega_c}{2e\phi_{ab}}. \tag{6}$$

Thus $a_{max}\ll w$ if $\hbar\omega_c<e\phi_{ab}$.

For what follows, no less important information from Refs. 6–8 concerns the distribution of the electric potential along an incompressible strip. Referring the reader to the primary sources for the details, following Ref. 7 we have

$$e\varphi(x) = -\frac{2\pi e^2}{\kappa}\frac{n''(0)}{6}(a_c^2 - x^2)^{3/2}, \quad |x| \leqslant a_c. \tag{7}$$

Here $2a_c$ is the width of an integer channel, defined above.

Completing the definition of the equilibrium characteristics of a Corbino disk which are required for what follows, we introduce also the perturbation arising in the ''chemical'' part $\zeta(x)$ of the electrochemical potential $\mu(x)$ as a result of the existence of $e\varphi(x) \neq 0$. The corresponding relation arises from the general requirement of equilibrium in a magnetized 2D system

$$\mu(x) = \text{const} = e\varphi(x) + \zeta(x), \tag{8}$$

and taking account of the fact that φ (7) vanishes asymptotically at large distances from the center of the strip gives

$$\zeta(x) = -e\varphi(x). \tag{8a}$$

Besides a central plateau, additional lateral channels of width a_i, which likewise was investigated in Refs. 6–8, can also exist:

$$a_i^2 \simeq \kappa\hbar\omega_c/e^2 dn(x_i)dx, \quad n_s + \delta n(x_i) = i/\pi l_H^2, \quad i = 2,3,4, \ldots . \tag{9}$$

Here n_s is the average density of the 2D system in the absence of contact phenomena, and $\delta n(x)$ is given by Eq. (2).

For what follows, we shall also determine the integer number I of strips in the disk. This definition arises from the requirements

$$(w - x_I) \geqslant a_i \quad \text{and} \quad \delta n(x_I) - \delta n(0) = (I-1)/\pi l_H^2$$

and the assumption that the central strip has a unit filling factor. As a result,

$$\delta n(x_I) - \delta n(0) = (I-1)/\pi l_H^2, \tag{10}$$

$$2x_I/w = (1-\epsilon) + \sqrt{(1-\epsilon)^2 - 4\epsilon}, \quad \epsilon = \hbar\omega_c/2e\phi_{ab}.$$

The channels closest to the metal terminals has a width $a_{\min}$ given by

$$a_{\min}^2 = 2\pi^2 w^2 \epsilon^3. \tag{11}$$

This estimate follows from the definition (9) at the points $\pm x_I$.

2. It is natural to start the discussion of the effect of contact phenomena on the Ohmic conductance of a Corbino disk with inner and outer radii r_0 and r_1, respectively, in a magnetic field which is applied in a direction normal to the surface of the disk and maintains the 2D electron system in a state close to a unit magnetic filling factor, with a presentation of the formulas that ordinarily arise in calculations of the current–voltage characteristic of a disk under QHE conditions. These are the relations between the total current J and the electrochemical potential μ

$$J/2\pi r = e^{-1}\sigma_{rr} d\mu/dr, \quad \mu(r_1) - \mu(r_0) = eV, \tag{12}$$

where σ_{rr} is the local conductivity of the 2D system and V is the guiding voltage applied to the edges of the disk. Moreover, the structure of the conductivity σ_{rr}, which in general is not a constant of the theory, is important. Under QHE conditions σ_{rr} is given by the well-known expression[9–12]

$$\sigma_{rr}=\sigma_0 e^{-\Delta/T}\cosh(\delta\mu/T), \tag{13}$$

where the Fermi energy (the electrochemical potential) $\delta\mu$ is measured from the midpoint between Landau levels, Δ is the activation energy with $\delta\mu=0$, and T is the temperature. The approximation (13) is meaningful when variations $\delta\mu(r)$ are present in the 2D system and there are no variations in the electric potential $\varphi(r)$. For definiteness, formula (13) is called below the ''μ representation.''

Together with Eq. (13), there is an alternative phenomenological definition of the conductivity (likewise discussed in Refs. 10 and 11)

$$\sigma_{rr}=\sigma_0 e^{-\Delta/T}\cosh[(\mu-e\varphi)/T]\equiv\sigma_0 e^{-\Delta/T}\cosh[\zeta(r)/T]. \tag{14}$$

This expression, called below the ''ζ representation,'' takes account of both the spatial dependence $\mu(x)$ and the possible coordinate dependence $\varphi(x)$. Ordinarily, formulas (13) and (14) are used to take account of different nonlinearity channels in the structure of the current–voltage characteristic (see, for example, Refs. 10 and 11). However, as follows from the discussion below, these definitions are also important in the Ohmic regime.

In the scenario (13), the Ohmic conductivity of an integer channel is uniform over the cross section of the channel (because in equilibrium $\mu=\text{const}$). For this reason, on the basis of Eqs. (12) and (13) Ohm's law for a Corbino disk is

$$\frac{J}{2\pi\sigma_{rr}}\ln\left(\frac{r_c+a_c}{r_c-a_c}\right)=V, \quad r_c=(r_1+r_0)/2. \tag{15}$$

The conductivity of a 2D system outside an integer channel is assumed to be infinite.

It should be noted that in the general case of values of V which are not small the combination (12) and (13) leads to a nonlinear equation that contains only $\mu(r)$ and does not depend on the detailed characteristics of the 2D system in a magnetic field (for example, the density of states). Such a simplification of the current–voltage characteristic is at variance with existing experiments[10] and therefore casts doubt on the reasonableness of the definition (13). More realistic is the ζ representation (14). In this variant the conductivity of the channel $2a_c$ is sharply nonuniform over the cross section of the channel, and this circumstance influences the details of Ohm's law for the Corbino disk:

$$\frac{J}{2\pi}\int_{r_0}^{r_1}\frac{dr}{r\sigma_{rr}(r)}=V. \tag{16}$$

Obviously, the principal value of the integral (16) is determined by the neighborhoods of saddle points where $d\zeta(r)/dr=0$. There are three such points. One point, $r_c=(r_0+r_1)/2$, corresponds to a maximum of $\zeta(r)$ and hence a maximum of the conductivity. The two other points are located on the edges of an integer channel, because the derivatives of the electric potential (7) (and hence also $\zeta(r)$ from Eq. (8a)) vanish by definition at these points, corresponding to the minima of the potential. Since in regions far from the channel ends the ratio $e\varphi(r)/T\gg 1$ is quite large, it should be possible to calculate the integral (16) by the method of steepest descent (the saddle points lie on the edges of the integer channel). However, the standard implementation of this program encounters technical difficulties (the coefficients in the Taylor expansion for the electric potential (7) on the edges of the integer channel are infinite, starting with the quadratic term). None-

theless, the conductivity (11) is exponentially minimum near the edges of the channel at distances $l_a^{(1)} \ll a_c$, and this fact can be used to simplify expression (16), so that

$$\frac{CJl_a^{(1)}}{2\pi\sigma_0 r_c}\exp(\Delta/T)=V, \quad r_c \gg 2a \gg l_a, \tag{17}$$

$$C=2\int_0^{+\infty}\frac{dx}{\cosh x^{3/2}}, \quad l_a^{(1)}=a_c^{-1}\left(\frac{\kappa T}{4\pi e^2 n''(0)}\right)^{2/3}. \tag{18}$$

Formula (17) contains a new scale length $l_a^{(1)}$, on which, essentially, the main voltage drop occurs during the flow of a transport current in a Corbino disk with one (central) channel in the disk.

If $\epsilon \ll 1$ is sufficiently small, the 2D region of the disk can contain seven channels and Ohm's law assumes the form

$$\frac{J}{2\pi\sigma_0 r_c}\exp(\Delta/T)\left[l_a^{(1)}+\sum_{i=2}^{i=I} l_a^{(i)}\right]=V, \quad l_a^{(i)}=a_i\frac{T}{\hbar\omega_c}, \quad 2\leqslant i\leqslant I. \tag{19}$$

Here $l_a^{(1)}$, a_i, and I are given by Eqs. (18), (9), and (10), respectively.

3. We shall now say a few words about the experimental situation. Unfortunately, I know of no direct Ohmic measurements, containing information about dimensional effects and other details of the conductance, on Corbino disks under QHE conditions. This information can be extracted at a qualitative level by analyzing the pattern of breakdown of the QHE regime in samples with the Corbino geometry. In this case, however, there arises the question of the critical voltage on the edges of the disk being systematically in excess of the characteristic value of $\hbar\omega_c$ at which any theory of the current–voltage characteristic exhibits nonlinear effects. For example, in a recent publication[13] the QHE regime in a GaAs Corbino disk with density $n_s=3.7\times10^{11}$ cm^{-2}, temperature $T=1.3$ K, and magnetic field $H=8.18$ T, which corresponds to a filling factor of 2, is ''broken down'' by a voltage $V_c \simeq 500$ mV. At the same time, the cyclotron energy of the 2D system $\hbar\omega_c/e \simeq 60\,\text{mV} \ll V_c$ is almost an order of magnitude lower than the critical value.

Contact phenomena resolve the above-noted paradox in a completely natural manner. The point is that when several incompressible strips are present, forming a successive chain of resistances along the Corbino disk, the external voltage drop is distributed between all channels, so that the voltage drop on each channel does not exceed $\hbar\omega_c/e$. As a result, the experimental result $eV_c/\hbar\omega_c \gg 1$, which appears to be paradoxical at first glance, in reality (according to the relations (19)) reflects the presence of a large number of integer strips $I \gg 1$ in the disk

$$eV_c/\hbar\omega_c \simeq I \gg 1. \tag{20}$$

Knowing I, it is easy to estimate the scale $e\phi_{ab}$ using Eq. (10). In the case of Ref. 13, $e\phi_{ab} \simeq 1000$ K.

In summary, in the present work the conductance of a Corbino disk under QHE conditions in the presence of contact phenomena was calculated. As a result, the disk is divided by a collection of concentric incompressible strips, each of which can ''withstand'' transport voltages of the order of the cyclotron frequency without breakdown of

the QHE regime. The number of strips is determined by the ratio $eV_c/\hbar\omega_c$ and is usually quite large, which attests to an appreciable difference of the work function for the 2D system and the metallic terminals in contact with it. Each strip conducts extremely nonuniformly with maximum resistance on its edges near lengths $l_a^{(i)}$. According to Eqs. (18) and (19) and also Eqs. (5) and (11) all lengths $l_a^{(i)}$ are proportional to w. For this reason, the critical voltage in the breakdown of the QHE regime should decrease with w, as experiments confirm (see, for example, Ref. 13).

I thank V. F. Gantmakher and V. T. Dolgopolov for a discussion of the results obtained. This work was supported by the Russian Fund for Fundamental Research under Grant No. 98-02-16640.

[1] L. D. Landau and E. M. Lifshitz, *Electrodynamics of Continuous Media*, Pergamon Press, New York [Russian original, Gostekhizdat, Mosow, 1957, p. 133].
[2] V. B. Shikin, JETP Lett. **65**, 189 (1997).
[3] V. T. Dolgopolov, A. A. Shashkin, G. V. Kravchenko *et al.*, JETP Lett. **63**, 63 (1996).
[4] W. Dietsche, K. von Klitzing, and K. Ploog, Surf. Sci. **361**, 289 (1996).
[5] V. B. Shikin and N. I. Shikina, JETP Lett. **62**, 894 (1995).
[6] D. B. Chklovskii, B. I. Shklovskii, and L. I. Glazman, Phys. Rev. B **46**, 4026 (1992).
[7] D. B. Chklovskii, K. F. Matveev, and B. I. Shklovskii, Phys. Rev. B **47**, 12605 (1993).
[8] D. Chklovskii, P. Lee, Phys. Rev. B **48**, 18060 (1993).
[9] M. G. Gavrilov and I. V. Kukushkin, JETP Lett. **43**, 103 (1986).
[10] A. A. Shashkin, V. T. Dolgopolov, and S. I. Dorozhkin, Zh. Éksp. Teor. Fiz. **91**, 1897 (1986) [Sov. Phys. JETP **64**, 1124 (1986)].
[11] M. I. Dyakonov and F. G. Pikus, Solid State Çommun. **83**, 413 (1992).
[12] S. I. Iordanskiĭ and B. A. Muzykantskiĭ, Zh. Éksp. Teor. Fiz. **103**, 2116 (1993) [JETP **76**, 1055 (1993)].
[13] Z. Liu, G. Nachtwei, J. Gross *et al.*, Phys. Rev. B **58**, 4028 (1998).

Translated by M. E. Alferieff

Hysteresis of conduction via impurities in uncompensated crystalline silicon in strong crossed electric and magnetic fields

A. P. Mel'nikov,* Yu. A. Gurvich, and E. M. Gershenzon
Moscow Pedagogical State University, 119435 Moscow, Russia

L. N. Shestakov
Maritime State University, 163006 Arkhangelsk, Russia

(Submitted 4 December 1998)
Pis'ma Zh. Éksp. Teor. Fiz. **69**, No. 1, 70–74 (10 January 1999)

It was observed that in uncompensated silicon in sufficiently strong crossed electric (E) and magnetic (H) fields the conductivity σ exhibits hysteresis as a function of E with $H=\text{const}$ and as a function of H with $E=\text{const}$. For the same values of E and H the conductivity can differ by a factor of 10^5. Weak pulses of a field E transfer the conductivity from one branch of the hysteresis loop to another. Very low-intensity background radiation radically changes the form of this loop. The results can be attributed to an insulator–metal transition stimulated in the D^- band of silicon by a strong electric field. © *1999 American Institute of Physics.* [S0021-3640(99)01401-2]

PACS numbers: 72.20.−i, 71.30.+h

1. Conduction via impurities in doped crystalline Si with very low compensation ($K=10^{-4}-10^{-5}$) exhibits a variety of characteristic features. It is believed that these features are due to the fact that conduction along the $D^-(A^+)$ band — motion of electrons (holes) via neutral donors (acceptors) — plays an important role in such materials. Recently the existence of conduction along the D^- band was directly confirmed in experiments measuring the photoconductivity spectra in the microwave region.[1]

It was established that the conduction is of a different character for different values of E. In weak fields ($E<E_c=200-250$ V/cm) the conduction is of a hopping character. Electrons hop along localized D^- states. These states lie near a certain energy level ε_{tr} (the transport level). The position of ε_{tr} depends on E. In our experimental samples the distance between ε_{tr} and the bottom ε_c of the unoccupied band was greater than 10 meV. In strong fields $E>E_c$ a mobility threshold ε_μ, lying $\leqslant 10$ meV below ε_c (see Fig. 1),[2] arises in the D^- band. States with energy $\varepsilon>\varepsilon_\mu$ are delocalized (field-induced delocalization).

As is well known, the localization radius near the mobility threshold grows without bound.[3] As a result, when ε_μ arises, the equilibrium between hops downward and upward in energy breaks down in the region $\varepsilon<\varepsilon_\mu$ in favor of upward hops. A rearrangement of the electron distribution over energy occurs: The region above the mobility threshold

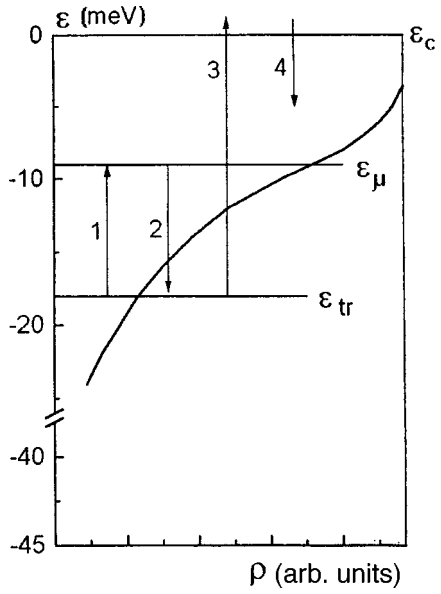

FIG. 1. Schematic representation of the density of states ρ (solid curve), the energy levels in the D^- band, and the electronic transitions.

$\varepsilon > \varepsilon_\mu$ is populated by electrons. A kind of insulator–metal transition ($D \rightarrow M$) induced by an electric field occurs. The transition $D \rightarrow M$ leads to rapid growth of the conductivity — quasibreakdown — for $E > E_c$ (Ref. 1).

Since the appearance of quasibreakdown is strongly related with the divergence of the localization radii near ε_μ, it should be expected that a magnetic field H will strongly influence the transition $D \rightarrow M$. The purpose of the present work was to investigate experimentally the effect of H on conduction along the D^- band in strong fields E perpendicular to H.

2. We present below the results obtained at $T = 4.2$ K a Si:B sample (p type; main impurity density $N = 6 \times 10^{16}$ cm^{-3}, $K = 10^{-4}$). Curve *1* in Fig. 2 shows $\sigma(E)$ at $H = 0$. It is evident that a sharp increase of $\sigma(E)$ — quasibreakdown — occurs at $E = E_c \approx 200$ V/cm. We have already presented such curves in an earlier work.[2,4] Curve *2* was obtained at $H = 20$ kOe in the forward (increasing E) and reverse (decreasing E) directions. The rate of change of E was 2 V/min. The arrows on the curves indicate the direction of motion. One can see that the quasibreakdown shifts to large values of E and becomes steeper. The main result is the presence of hysteresis in $\sigma(E)$. For example, in a field $H = 20$ kOe the value of σ increases rapidly at $E = E_2 \approx 252$ V/cm in the forward direction. For the reverse motion σ drops rapidly at $E = E_1 \approx 240$ V/cm. Hysteresis becomes even more pronounced in the field $H = 46$ kOe (curve *3*).

Figure 3 shows $\sigma(H)$ for $E = \text{const}$. The rate of change of H is 1 kOe/min. Hysteresis is also observed here. We note that the values of σ lying on the same vertical line can differ by almost a factor of 10^5.

We shall present further results for curve *3* in Fig. 3. Let H_1 and H_2 be the right-

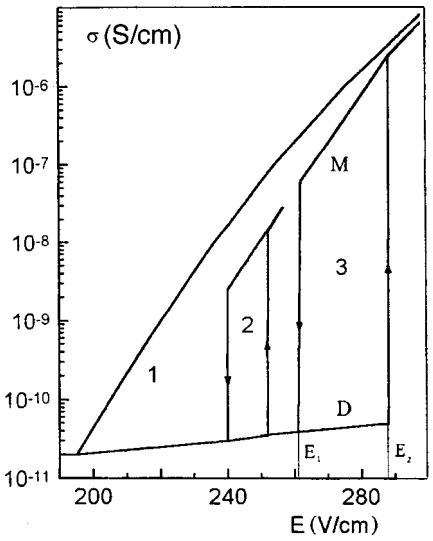

FIG. 2. $\sigma(E)$ for H, kOe: *1* — 0, *2* — 20, *3* — 46.

and left-hand limits of hysteresis, respectively. We fix an intermediate value $H=H_0$: $H_2<H_0<H_1$. At $H=H_0$ the conductivity can be large $\sigma=\sigma_M(H_0)$ (M — top section) or small $\sigma=\sigma_D(H_0)$ (D — bottom section). If H_0 is close to the center of the loop, states with conductivities $\sigma_M(H_0)$ and $\sigma_D(H_0)$ are stable or, possibly, metastable but with a very long lifetime. Thus, for $H_0\approx 1/2(H_1+H_2)$ we were not able to detect a change in σ_M or σ_D in a time greater than 1 h.

If H_0 approaches H_1, the state with conductivity σ_M becomes unstable. Fluctuations arise — short-lived deviations of the conductivity in the direction of smaller values. The magnitude and frequency of these deviations increases as $H_0\to H_1$ (see Fig. 3, curve *3*). As $H_0\to H_2$, the conductivity σ_D becomes unstable. Deviations of the conductivity are observed even in the direction of large values (these fluctuations are not shown on the other curves to avoid cluttering the figure). We note that the position of H_1 and H_2 depends on the scan rate. For example, decreasing the rate to 0.1 kOe/min (by a factor of 10) decreases the difference H_1-H_2 by approximately 10%.

For $H_2<H_0<H_1$ the transitions $M\leftrightarrow D$ can be induced by sufficiently strong electric field pulses ΔE (see below). A pulse $\Delta E>0$ ($E+\Delta E>E$) induces a transition $D\to M$ and a pulse $\Delta E<0$ induces a transition $M\to D$.

Low-intensity background radiation with low photon energies (in the experiment a system of cold filters transmitted radiation with $\hbar\omega\leqslant 20$ meV; the binding energy of the ground state was 45 meV) shifts H_2 toward H_1, narrowing the hysteresis loop and thereby decreasing the extent of the low-conductivity region. The dotted line in Fig. 3 shows the left-hand limit H_2' of hysteresis in the presence of a background. We underscore that such a strong shift of the left-hand boundary occurs for low background intensities such that the background has no influence on the conductivity outside hysteresis. Such a background has virtually no effect on the position of the right-hand boundary.

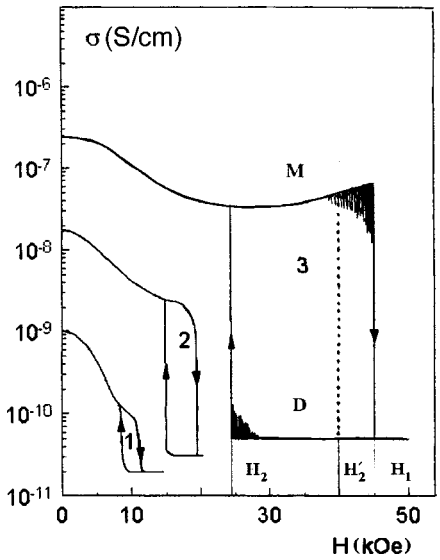

FIG. 3. $\sigma(H)$ for E, V/cm: *1* — 220, *2* — 240, *3* — 262.

The hysteresis boundaries in Fig. 3 are functions of the electric field: $H_1=H_1(E)$ and $H_2=H_2(E)$. The left-hand (E_1) and right-hand (E_2) boundaries in Fig. 2 are functions of H: $E_1=E_1(H)$ and $E_2=E_2(H)$ (the index 1 in the fields corresponds to a decrease in σ and the index 2 corresponds to an increase). It was found that the curves $E_1(H)$ and $H_1(E)$ coincide (Fig. 4, curve *1*). Likewise, the curves $E_2(H)$ and $H_2(E)$ coincide (Fig. 4, curve *2*).

3. Let us consider the E,H plane. The part of the plane shown in Fig. 4 can be divided into three regions. A region of low conductivity — ''dielectric'' or D region ($\sigma=\sigma_D$) — lies below curve *1*. A region of high conductivity — ''metallic'' or M region ($\sigma=\sigma_M$) — lies above curve *2*. A definite value of the conductivity corresponds to each point in the region D or M. A region, which we designate as $D\cap M$, where σ is a double-valued function of the position of the point, lies between curves *1* and *2*. Here the conductivity can be low or high depending on whence we arrive into this region by varying E and H. Moving from the D into the M region, the conductivity remains low ($\sigma=\sigma_D$) right up to intersection with curve *2*, where the transition $\sigma_D\rightarrow\sigma_M$ occurs. For the reverse motion on curve *1* a transition $\sigma_M\rightarrow\sigma_D$ occurs. Therefore a transition $M\rightarrow D$ always occurs on curve *1*, and a transition $D\rightarrow M$ always occurs on curve *2*. It is obvious that the region $D\cap M$ corresponds to hysteresis.

4. Let us now discuss the results obtained. We shall consider an *n*-type material. We spoke above of two types of conductivity: hopping (dielectric) — near the level $\varepsilon_{\rm tr}$ and metallic — via states near the delocalization threshold ε_μ. We assume that the jumps in conductivity accompanying a change in E or H are due to switching of conduction from the level $\varepsilon_{\rm tr}$ to the level ε_μ and vice versa. In other words, this is a manifestation of $M\leftrightarrow D$ transitions induced by an electric field. In contrast to Ref. 1, here these transitions occur in the presence of a magnetic field.

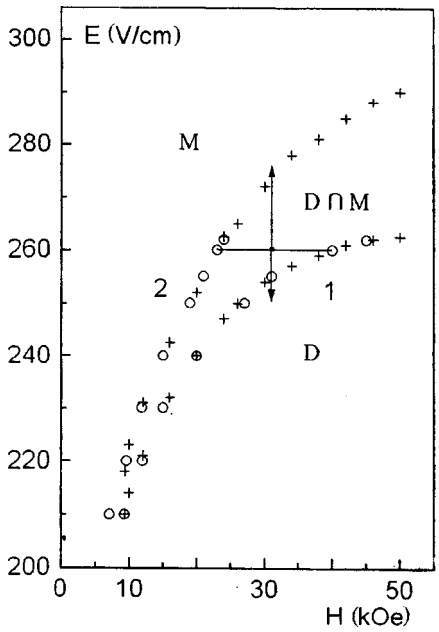

FIG. 4. Curve *1*: $E_1(H)-(+)$ and $H_1(E)-(\bigcirc)$; curve *2*: $E_2(H)-(+)$ and $H_2(E)-(\bigcirc)$.

According to Ref. 1, the transition $D\rightarrow M$ is a result of two processes: the appearance of a threshold ε_μ and the occupation of states with $\varepsilon>\varepsilon_\mu$. Both processes are stimulated by an increase in E. The reverse processes occur as E decreases. Under our experimental conditions the voltage on the sample was fixed. Let a conductivity fluctuation $\Delta\sigma<0$ occur in a state $\sigma=\sigma_M$ in some small region. If the fluctuation does not subside rapidly enough, a redistribution of the field E in the sample will occur: the field inside the region under study will increase and the field in the surrounding region will decrease. The latter will result in a decrease of the population of states with $\varepsilon>\varepsilon_\mu$ or even a disruption of delocalization in this neighborhood. In turn, this will give rise to a redistribution of the field in an even larger volume. The process will propagate like an avalanche over the entire sample, and the conductivity will drop rapidly. An almost vertical transition $\sigma_M\rightarrow\sigma_D$ will occur. Similar arguments explain the sharpness of the reverse transition.

The effect of electric field pulses can be explained in an obvious manner. Let the conductivity be $\sigma_D(P)$ at some point $P(H,E)$ in the region $D\cap M$ (see Fig. 4). A pulse $\Delta E>0$, displacing the point vertically upwards outside the region $D\cap M$, gives rise to a transition $\sigma_D\rightarrow\sigma_M$. After the pulse ends, the conductivity remains equal to σ_M. Similarly, a pulse $\Delta E<0$ can give rise to a transition $\sigma_M\rightarrow\sigma_D$. The minimum values of $|\Delta E|$ can be easily estimated from Fig. 4 (see the vertical arrows in this figure). This estimate agrees with experiment.

Curves *1* and *2* in Fig. 3 are the boundaries of stability of the M and D states, respectively. This is indicated by the increase in fluctuations as H approaches H_1 from

the left side or H_2 from the right side. Since the states themselves are different, their stability boundaries, generally speaking, should not coincide. In such a case, hysteresis should be observed.

In our samples with $H=0$ a threshold ε_μ appears (vanishes) and a redistribution of the electrons — population (depopulation) of states with $\varepsilon>\varepsilon_\mu$ — occurs at essentially the same value of the field: $E=E_c$. It can be inferred that for $H\neq 0$ these processes occur in different fields. This supposition is supported by the following argument. A redistribution occurs as a result of a displacement of electrons completely through the region of localized states between $\varepsilon_{\rm tr}$ and ε_μ. In a magnetic field, it is more difficult for electrons to pass through this region: The field H contracts the wave functions lying below the mobility threshold of weakly localized states. The probability of a hop and therefore the hopping conductivity decrease sharply. Therefore redistribution should be delayed with respect to the moment at which ε_μ appears or vanishes.

The following question arises: What happens when a jumplike change of σ occurs at the hysteresis boundaries: population (or depopulation) of states with $\varepsilon>\varepsilon_\mu$ (transitions *1* and *2* in Fig. 1) or appearance (disappearance) of the mobility threshold itself?

Experiments with background radiation give a partial answer to this question. The background radiation transfers electrons from localized states into an unoccupied band (transition *3* in Fig. 4). Next, the electrons are trapped in the D band (transition *4* in Fig. 1). It was noted above that as H decreases, the transition $\sigma_D\rightarrow\sigma_M$ occurs in the presence of a background in a field $H_2'>H_2$ (see Fig. 3), i.e., in the interval $H_2<H<H_2'$ the background produces a conductivity σ_M. This means that for $H\leqslant H_2'$ there exists a threshold ε_μ and that photoelectrons are trapped in states lying above this threshold. Hence it can be concluded that the transition $\sigma_D\rightarrow\sigma_M$ in the absence of a background (i.e., for $H=H_2$) is likewise due to occupation of states lying above a mobility threshold which already exists in these fields. The latter arises as H decreases at some $H=H_C\geqslant H_2'$. The appearance of a threshold has no effect on the conductivity, since in the interval $H_2<H<H_C$ states with $\varepsilon>\varepsilon_\mu$ in the absence of a background are still not occupied. (In this connection we note that with respect to the transitions $D-M$ a decrease of H, as is evident from Fig. 4, is equivalent to an increase of E.)

A comparison of the results obtained for different samples reveals the following law. The higher the conductivity σ_D via localized states, the weaker the hysteresis. In this case, not only the difference of the values of the conductivity decreases (which is obvious) but the width of the loop also decreases. This once again attests to the influence of hopping conduction in the gap $\varepsilon_\mu-\varepsilon_{\rm tr}$ on the kinetics of hysteresis.

Further experiments are required in order to determine the character of the transition $\sigma_M\rightarrow\sigma_D$ with $H=H_1$.

This work was supported by the Russian Fund for Fundamental Research (Grant 98-02-116903).

*e-mail: melnikov@rpl.mpgu.msk.su

[1] A. P. Mel'nikov, Yu. A. Gurvich, L. N. Shestakov, and E. M. Gershenzon, JETP Lett. **66**, 249 (1997).
[2] A. P. Mel'nikov, Yu. A. Gurvich, L. N. Shestakov, and E. M. Gershenzon, JETP Lett. **65**, 59 (1997).

[3] N. E. Mott and E. A. Davis, *Electronic Processes in Non-Crystalline Materials*, Clarendon Press, Oxford, 1979; Mir, Moscow, 1982.
[4] Yu. A. Gurvich, A. P. Melnikov, L. N. Shestakov, and E. M. Gershenson, JETP Lett. **61**, 730 (1995).

Translated by M. E. Alferieff

Experimental evidence for Coulomb charging effects in submicron Bi-2212 stacks

Yu. I. Latyshev*

Institute of Radio-Engineering and Electronics, Russian Academy of Sciences, 103907 Moscow, Russia;
Research Institute of Electrical Communication, Tohoku University, 2-1-1, Katahira, Aoba-ku, Sendai 980-8577, Japan;
CREST, Japan Science and Technology Corporation (JST), Japan

S.-J. Kim and T. Yamashita

Research Institute of Electrical Communication, Tohoku University, 2-1-1, Katahira, Aoba-ku, Sendai 980-8577, Japan;
CREST, Japan Science and Technology Corporation (JST), Japan

(Submitted 10 December 1998)
Pis'ma Zh. Éksp. Teor. Fiz. **69**, No. 1, 75–80 (10 January 1999)

Focused ion beam (FIB) and ion milling techniques are developed for the fabrication of $Bi_2Sr_2CaCu_2O_{8+d}$ (Bi-2212) stacked junctions with in-plane size L_{ab} ranging from several microns down to the submicron scale without degradation of superconducting transition temperature T_c. It is found that the behavior of submicron junctions ($L_{ab}<1\,\mu$m) is quite different from that of larger ones. The critical current density is considerably suppressed, the hysteresis and multibranched structure of the current–voltage (I–V) characteristics are eliminated, and a periodic structure of current peaks appears reproducibly on the I–V curves at low temperatures. The period ΔV of the structure is consistent with the Coulomb charging energy of a single pair, $\Delta V=e/C$, where C is the effective capacitance of the stack. It is considered that this behavior originates from the Coulomb blockade of the intrinsic Josephson tunneling in submicron Bi-2212 stacks. © *1999 American Institute of Physics.* [S0021-3640(99)01501-7]

PACS numbers: 85.25.Cp, 74.50.+r

As is well known, the tunneling current in a tunnel junction of small capacitance C can be blocked by the charging effect at bias voltages eV below the Coulomb charging energy of a single electron, $E_c=e^2/2C$, when E_c exceeds the energy of thermal and quantum fluctuations, $E_c>kT$, and $R>h/4e^2=R_Q$, where R is the tunneling resistance of the junction.[1] In a similar way, the Coulomb blockade effect can block the Josephson tunneling current in a Josephson junction of small enough area at low temperatures, where E_c becomes comparable to or greater than the Josephson coupling energy E_J (Ref. 2). The Coulomb blockade of the Cooper pair tunneling gives rise to a periodic structure of current peaks on the current–voltage (I–V) characteristics of small junctions, with a voltage period $\Delta V=2E_c$ (Ref. 3). The ''supercurrent'' has a finite slope due to the

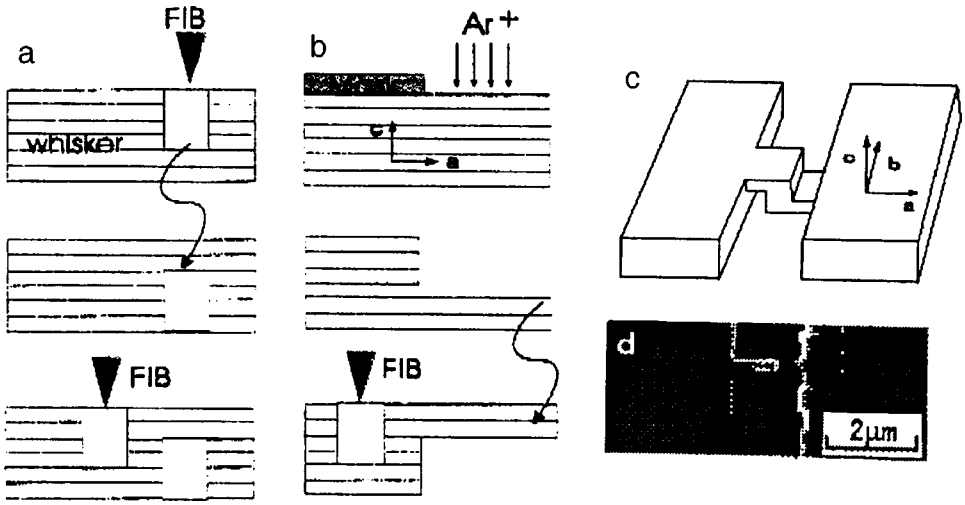

FIG. 1. Stages of the stack fabrication with FIB (a), FIB combined with the ion milling (b), a schematic view (c), and a micrograph of the submicron Bi-2212 stacked junction.

quantum or classical diffusion of the phase of the order parameter,[2] and the value of supercurrent is suppressed in proportion to the ratio E_c/E_J (Ref. 2).

The charging effects become even stronger in arrays of small junctions,[4] where the tunneling of a single electron (or pair) has recently been considered as the correlated motion of a charge soliton including a number of junctions.[5,6] The charge soliton length can be enormously large in vertically stacked junctions because of their negligibly small stray capacitance.[6] This implies that a whole stack of N junctions can effectively work as a single unit, with a charging energy N times higher than the charging energy of a single junction.

In this paper we report on studies of the intrinsic Josephson effect[7] in stacked structures of Bi-2212 with a successive decrease of their in-plane area S down to the submicron scale. We found that the interplay between the charging effects and the intrinsic Josephson effect becomes appreciable at $S \sim 1\ \mu\text{m}^2$. For the submicron junctions we clearly observed a periodic structure of current peaks on the I–V characteristics, with a period corresponding to the charge energy of a Cooper-pair charge soliton including the total number of elementary junctions (~ 50) of the stack.

We used Bi-2212 whiskers[8] as the base material for the stacks fabrication. Whiskers grown by the Pb-free method[9] have been characterized by TEM as a very perfect crystalline object.[9] We developed focused ion beam (FIB) and ion milling techniques for the fabrication of Bi-2212 stacked junctions with in-plane sizes from several microns down to the submicron scale without degradation of T_c (Ref. 10). The stages of the fabrication are shown at Fig. 1. The fabrication was done using a conventional FIB machine (Seiko Instruments SMI-900 (SP)), operating with a Ga^+ ion beam with energy ranging from 15 to 30 keV and beam current from 8 pA to 50 nA. For the smallest current the beam diameter can be focused down to 10 nm. We estimate the maximum penetration depth of 30 kV Ga^+ ions along the c axis in a Bi-2212 single crystal to be 60 nm and the lateral

TABLE I. Parameters of the stacked Bi-2212 junctions.

No.	S (μm^2)	R_N k(Ω)	I_c (μA)	J_c (A/cm^2)	T_c (K)	V_g (V)	N	V_g/N (mV)	C fF	ΔV (mV)	$2NE_{C0}$ (mV)
#1	6.0.	2.1	36	600	76	1.1	69	16	2.4	–	0.67
#2	2.0	6.5	12	600	76	1.3	65	20	0.68	–	0.22
#3	1.5	4.6	6	400	78	1.1	38	29	0.96	–	0.18
#4	0.6	10	0.24	40	76	1.7	34	50	0.44	0.38	0.36
#5	<1	13	0.30	30–60	–	–	–	–	0.38	0.45	0.42
#6	0.3	30	0.07	23	78	2.2	50	44	0.15	1.10	1.04

scattering depth to be 40 nm (Ref. 11). For the ion milling we used the standard Ar-ion plasma technique. Four electrical contacts were prepared outside the processing zone in two ways: by the application of silver paste or by evaporation of gold pads 70 nm thick with a subsequent annealing in an oxygen flow at 450 °C. In both cases the annealing of the contacts was done before the FIB processing to avoid diffusion of the Ga ions in the stack body. The parameters of several stacks under investigation are listed in Table I.

The I–V characteristics were measured in a shielded room using a low-noise preamplifier and a high-sensitivity oscilloscope at frequencies $\sim$100 Hz. We estimated the noise current level to be about 10 nA. The temperature dependences of the *c*-axis resistivity ρ_c were measured using dc currents of 1–5 μA. The $\rho_c(T)$ curves of the stacks are like the typical curves of the slightly overdoped Bi-2212 case,[12] with $T_c \approx 77$ K and $\rho_c(300) = 10-12\ \Omega\cdot$cm. The critical current density along the *c* axis for the junctions with in-plane area $S > 2\ \mu$m^2 was $J_c \approx 6\times 10^2$ A/cm^2, which is consistent with a theoretical estimate, $J_c \approx 8\times 10^2$A/cm^2, obtained from Ref. 13: $J_c(0) = c\Phi_0/(8\pi^2 s\lambda_c^2)$, where Φ_0 is the flux quantum, $\lambda_{ab} = 0.2\ \mu$m, and $\gamma = \lambda_c/\lambda_{ab} \approx 1000$ (Ref. 14). For the larger stacks the curves of the critical current along the *c* axis versus the parallel magnetic field exhibit quite good Fraunhofer patterns,[15] which prove the presence of the dc intrinsic Josephson effect in our stacks.

Figure 2 shows the I–V characteristics on a large current and voltage scale for three stacks with a decrease of S down to 0.3 μm^2. The gap voltage at $V = V_g$ and the normal state resistance R_N at $V > V_g$ are well defined. The value of R_N is practically temperature independent and corresponds to a resistivity value $\rho_c(V > V_g) \approx 12\ \Omega\cdot$cm. From it one can estimate the number of elementary junctions, N, by the simple formula $N = R_N S/\rho_c(V > V_g)s$. For the submicron junctions (Figs. 2b,c) we did not observe the *S*-shaped I–V characteristics. This implies that the self-heating[16] and nonequilibrium injection effects[17] are essentially eliminated. As a result, we found that the superconducting gap of the elementary junction $2\Delta_0 = eV_g/N$ in submicron junctions reaches a value $2\Delta_0 \approx 50$ meV (see Table I), which is consistent with the value found recently from surface tunneling measurements.[18] The value of T_c determined by polynomial extrapolation of $\Delta(T)$ to zero lies within the range 76–78 K for all the samples, including the smallest one with $S = 0.3\ \mu$m^2 (see Table I). This indicates that the junction body is essentially unaffected by the FIB processing.

The I–V characteristics on a magnified scale are shown in Fig. 3. For a larger junction (#2) the multibranched structure[7] is clearly seen. The fact that the variation of

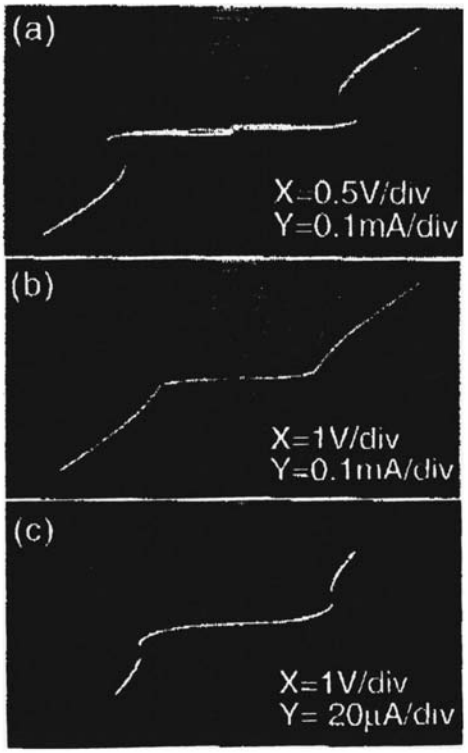

FIG. 2. The I–V characteristics of the Bi-2212 stacks on a large current and voltage scale: (a) #2, $S=2\ \mu\text{m}^2$; (b) #4, $S=0.6\ \mu\text{m}^2$; (c) #6, $S=0.3\ \mu\text{m}^2$. $T=4.2$ K.

the critical current along the stack is not large indicates good uniformity of our structures. The number of branches counted directly from the I–V characteristics is consistent with the number calculated using the formula for N given above.

We found also when S is decreased below $1-2\ \mu\text{m}^2$ the critical current density J_c of the stacks falls off (see Table I). For the submicron stacks the multibranched structure disappears. The critical current transforms into a ''supercurrent'' peak located at finite voltage. Besides, a periodic set of current peaks appears (Fig. 3). All these features are typical for the manifestation of the Coulomb blockade in a small Josephson junction.[3,19] The period ΔV of the current peak structure usually corresponds to the charging energy of a single pair, $2E_c$ (Ref. 3). For our smallest stack (#6) the period corresponds to $\Delta V=1.1$ mV, i.e., about three times the energy kT of thermal fluctuations at 4.2 K, and about 5 times higher than the Josephson coupling energy, $E_J=hI_c/4\pi e$, at this temperature.

In a stacked junction, charging effects are associated with the charge soliton.[4–6] The energy of the charge soliton, E_s, is proportional to the number of junctions located within the soliton length.[5] The large charging energy obtained, $\Delta V\approx 1$ mV ($\Delta V\equiv E_s$), evidently corresponds to the number of junctions. An estimate of the charging energy of a single elementary junction shows that this number corresponds to the total number of

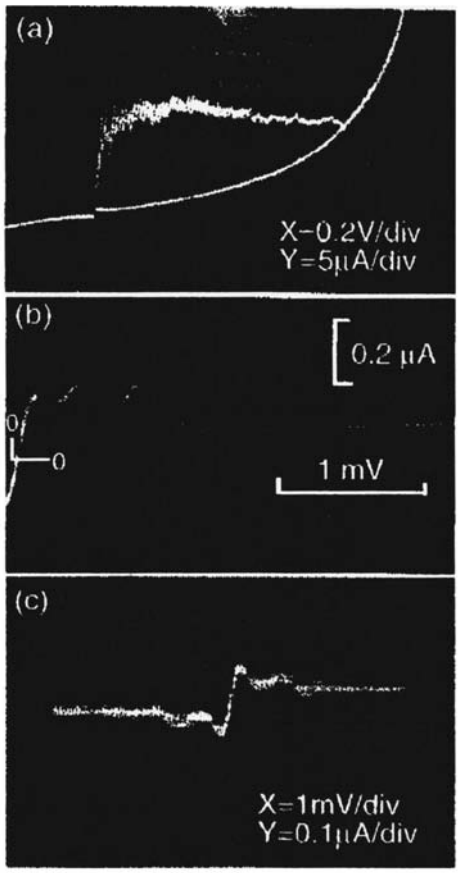

FIG. 3. The I–V characteristics of the Bi-2212 stacks on a small current and voltage scale: (a) #2, $S=2\ \mu\text{m}^2$; (b) #4, $S=0.6\ \mu\text{m}^2$; (c) #6, $S=0.3\ \mu\text{m}^2$. $T=4.2$ K.

elementary junctions in the stack. For instance, for stack #5 the charging energy of an elementary junction, $2E_{c0}$, estimated as $2E_{c0}=e^2s/\varepsilon_0\varepsilon_c S$, where ε_c is the dielectric constant along the c axis ($\varepsilon_c=5$ for Bi-2212),[20] is $2E_{c0}\approx 20$ meV, and the ratio $e\Delta V/2E_{c0}$ exactly corresponds to $N=50$, the total number of the junctions in this stack. We reproducibly observed the periodic structure of current peaks on 3 submicron stacks, with $R_N \geqslant 10$ kW, and in each case the period corresponded to the charging energy of the whole stack (see Table I). That observation is consistent with an estimate of the soliton length:[4] $L_s=2(C_0/C_g)^{1/2}$, where C_g is the stray capacitance, $C_g\approx(\varepsilon+1)s/8$ (Ref. 6), and ε is the dielectric constant of the substrate. It gives for L_s/s a value of about 400. From this estimate it follows that a stack with $N<400$ will respond to the transfer of a single pair as a single unit. This may be the reason for the disappearance of the multi-branched structure in the submicron stacks.

As S is decreased, the charging energy ΔV should increase in inverse proportion to the stack capacitance C or in direct proportion to R_N. The latter statement results from the fact that the product R_NC is a constant quantity independent of the stack geometry

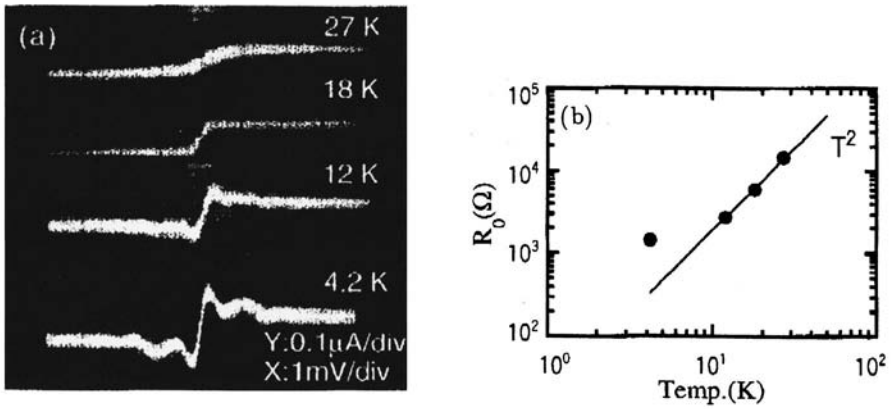

FIG. 4. Temperature evolution of the periodic structure on the I–V characteristics (a) and the temperature dependence of the zero-bias resistance R_0 (b) of Bi-2212 stack #6, $S=0.3\ \mu\text{m}^2$.

and size: $R_N C=\rho_c \varepsilon_0 \varepsilon_c$. That is in a reasonable agreement with experiment. We found ΔV to be roughly proportional to R_N for the three submicron stacks studied (see Table I).

As the temperature is increased above 4.2 K the structure of peaks gradually washes out (Fig. 4) and disappears above 12 K (for stack # 6) when the charge soliton energy ΔV becomes less than kT. The behavior of the supercurrent peak under conditions $E_J \ll kT$, $E_J \ll E_c$, which are roughly valid for our case, has been analyzed in Ref. 21. It was shown that in the case when the resistance of the environment, Z_1, is less than the quantum resistance R_Q, the junction will have classical phase diffusion behavior, and the zero-bias resistance R_0 should be proportional to $(kT)^2$: $R_0=2Z_1(kT/E_J)^2$. That is in qualitative agreement with our experiment (see the inset to Fig. 4).

A falloff of J_c for submicron junctions can also be explained by the Coulomb blockade effect. According to Ref. 2, J_c should fall off $\propto E_J/4E_c$. For our stacks the condition $E_J<4E_c$ is met for $S<1\ \mu\text{m}^2$. We defined the critical current for the submicron junctions as the height of the supercurrent peak I_0. The other current peaks, I_n, at $V=n\Delta V$ (n is an integer), also originate from the supercurrent contribution,[3] corresponding in our case to the correlated motion of single-Cooper-pair solitons. We note here that the amplitude of the two types of peaks changes with decrease of S in a correlated way, i.e., I_1/I_0 remains $\approx$ constant (compare Figs. 3b and 3c), indicating their common nature. The detailed picture of the correlated soliton motion in the stacked structures is still not clear and is in need of further theoretical and experimental investigations.

In summary, we developed the FIB method combined with the ion milling technique for the fabrication of small Bi-2212 stacked junctions with in-plane size down to the submicron level without degradation of their T_c. We found that the low-temperature behavior of the submicron junctions is governed by Coulomb charging effects and their interplay with the intrinsic Josephson tunneling. This is the first observation of the Coulomb charging effects in the layered high-T_c materials.

The authors are grateful to K. K. Likharev, T. Claeson, and L. N. Bulaevskii for a

helpful discussion the results. This study been supported in part by the Russian State Program on HTSC (Grant #95028).

*e-mail: latychev@riec.tohoku.ac.jp

[1] D. V. Averin and K. K. Likharev, *Mesoscopic Phenomena in Solids*, edited by B. L. Altshuler, P. A. Lee, and R. A. Webb, Elsevier, 1991, Chap. 6.
[2] M. Tinkham, *Introduction to Superconductivity*, McGraw-Hill, New York, 1996, Chap. 7.
[3] D. B. Haviland, Y. Harada, P. Desling *et al.*, Phys. Rev. Lett. **73**, 1541 (1994).
[4] P. Delsing, in *Single Charge Tunneling*, edited by H. Grabert and M. H. Devoret, Plenum Press, New York, 1992, p. 249.
[5] K. K. Likharev, N. S. Bakhvalov, G. S. Kazacha, and S. I. Serdyukova, IEEE Trans. Magn. **MAG-25**, 1436 (1989).
[6] K. K. Likharev and K. A. Matsuoka, Appl. Phys. Lett. **67**, 3037 (1994).
[7] For a review see: P. Mueller, in *Advances in Solid State Physics*, edited by R. Helbig, Vieweg, Braunschweig/Wiesbaden, 1994, Vol. 34, p. 1.
[8] I. Matzubara, H. Kageyama, H. Tanigawa *et al.*, Jpn. J. Appl. Phys., Part 2 **28**, L1121 (1989).
[9] Yu. I. Latyshev, I. G. Gorlova, A. M. Nikitina *et al.*, Physica C **C216**, 471 (1993).
[10] Yu. I. Latyshev, S.-J. Kim, and T. Yamashita, in *Abstract Book of the Applied Superconductivity Conference*, Palm Desert, Sept. 13–18, 1998, p. 150.
[11] S.-J. Kim, Yu. I. Latyshev, and T. Yamshita, unpublished.
[12] T. Watanabe, T. Fujii, and A. Matsuda, Phys. Rev. Lett. **79**, 2113 (1997).
[13] L. N. Bulaevskii, J. R. Clem, and L. I. Glazman, Phys. Rev. B **46**, 350 (1992).
[14] Yu. I. Latyshev, P. Monceau, and V. N. Pavlenko, Physica C **293**, 174 (1997).
[15] Yu. I. Latyshev, J. E. Nevelskaya, and P. Monceau, Phys. Rev. Lett. **77**, 932 (1996).
[16] J. Takeya, S. Akita, S. Watauchi *et al.*, Physica C **293**, 220 (1997).
[17] A. Yurgens, D. Winkler, N. V. Zavaritsky, and T. Claeson, Phys. Rev. B **53**, R887 (1996).
[18] N. Myakawa, P. Guptasarma, J. E. Zasadzinski *et al.*, Phys. Rev. Lett. **80**, 157 (1998).
[19] J. G. Lu, J. M. Hergenrother, and M. Tinkham, Phys. Rev. B **53**, 3543 (1996).
[20] J. U. Lee, G. Hohenwarter, R. J. Kelley, and J. E. Nordman, IEEE Trans. Appl. Supercond. **AS-5**, 2543 (1995).
[21] G.-L. Ingold and H. Grabert, Phys. Rev. B **50**, 395 (1994).

Published in English in the original Russian journal. Edited by Steve Torstveit.